SYNTHESIS, CHARACTERIZATION AND APPLICATIONS OF METAL NANOPARTICLES SUPPORTED ON POROUS CARBON

by

CHARITHA JAYARUK THAMBILIYAGODAGE

MARTIN G. BAKKER, COMMITTEE CHAIR
SHANE STREET
SHANLIN PAN
PAUL RUPAR
JASON BARA

A DISSERTATION

Submitted in partial fulfillment of the requirements
for the degree of Doctor of Philosophy
in the Department of Chemistry
in the Graduate School of
The University of Alabama

TUSCALOOSA, ALABAMA

2017

ABSTRACT

Porous carbon incorporating metal nanoparticles has been synthesized by nanocasting. The main two methods of synthesis were used: the formation of nanoparticles during the carbonization of carbon, and the formation of nanoparticles by metal precursor infiltration and reduction on porous carbon. The catalytic activity of nickel nanoparticles incorporated onto hierarchically porous carbon monoliths for the reduction of *p*-nitrophenol was studied. *p*-Quinoimine was identified as the stable intermediate. Catalytic graphitization of monolithic hierarchically porous carbon by iron, cobalt and nickel nanoparticles was investigated. The catalytic graphitization of amorphous carbon increased with increasing pyrolysis temperature. Iron was capable of graphitizing carbon more effectively than cobalt and nickel, with cobalt being higher in activity than nickel. Oxygen and nitrogen rich mesoporous carbon were used to support gold nanoparticles and their catalytic activity was investigated for oxidation of benzyl alcohol in water. The catalysts showed significant catalytic activity, but loss of activity were found, resulting in decreasing conversion of benzyl alcohol on subsequent cycles.

DEDICATION

This dissertation is offered to the triple gems of my religion for teaching the real meaning of the life. This dissertation is dedicated to my mother, father, and sister who are with me encouraging me and being the strength and the spirit of my whole life. This dissertation is a tribute for their effort. I would like to dedicate this dissertation to my brother and my little son who added extra courage for their support.

I would like to dedicate this dissertation to my best friend who supports my life being with me and understanding me in every ways. This dissertation is devoted to all my friends and everyone who helped me to accomplish this masterpiece.

LIST OF ABBREVIATIONS AND SYMBOLS

°C	degrees in Celsius
%	percent
θ	diffraction angle in degrees
AAS	Atomic absorption spectroscopy
Au NPs	gold nanoparticles
BET	Brunauer-Emmett-Teller
BJH	Barrett-Joyner-Halenda
C_{18}TAB	octadecyltrimethylammonium bromide
cm	centimeter
C	concentration at time = t
C_0	concentration at time = 0
cc	cubic centimeter
COMPO	composition (back scatter detector)
$Co(NO_3)_2$. $6H_2O$	cobalt(II) nitrate hexahydrate
CVD	chemical vapor deposition
dV(d)	derivative of volume with respect to diameter
e.g.	exempli gratia (for example)
et al.	et alia (and others)
etc.	et cetera (and so on)
eV	electron volt
EDS	Energy dispersive spectroscopy

FA	furfuryl alcohol
$Fe(NO_3)_3.\ 9H_2O$	iron(III) nitrate nonahydrate
FWHM	full width at half maximum
GADDS	general area detector diffraction system
GC	gas chromatography
GC-MS	gas chromatography-mass spectrometry
h	hour
$HAuCl_4.3H_2O$	hydrogen tetrachloroaurate(III) trihydrate
HRTEM	high resolution transmission electron microscopy
HRSEM	high resolution scanning electron microscopy
HNO_3	nitric acid
H_2O_2	hydrogen peroxide
i.e.	in other words
I_D	intensity of Raman D peak
I_G	intensity of Raman G peak
I_D/I_G	intensity ratio of Raman D and G peaks
K	Kelvin
k	pseudo-first order rate constant
KOH	potassium hydroxide
K_2CO_3	potassium carbonate
kV	kilo volt
mg	milligram
ms	millisecond
m	meter
mm	millimeter

µm	micrometer
nm	nanometer
mW	milliwatt
min	minutes
mol	mole
mol%	molar percentage
M	molarity
mM	millimolar
µM	micromolar
mL	milliliter
NPs	nanoparticles
NHE	normal hydrogen electrode
$NaBH_4$	sodium borohydride
NH_4OH	ammonium hydroxide
N_2	liquid nitrogen
NC	nanocast carbon
NC/Ni	nanocast carbon monoliths with nickel nanoparticles
NC/1%Ni	nanocast carbon monoliths with nickel nanoparticles (nickel loading 1 mol% with relative to the amount of FA)
NC/5%Ni	nanocast carbon monoliths with nickel nanoparticles (nickel loading 5 mol% with relative to the amount of FA)
NC/Fe	nanocast carbon monoliths with iron nanoparticles
NC/Co	nanocast carbon monoliths with cobalt nanoparticles
$Ni(NO_3)_2.6H_2O$	nickel(II) nitrate hexahydrate
NC/O	oxygen rich nanocast carbon
NC/O/Au	gold nanoparticles incorporated oxygen rich nanocast carbon

NC/O,N	oxygen and nitrogen rich nanocast carbon
NC/O,N/Au	gold nanoparticles incorporated oxygen and nitrogen rich nanocast carbon
OA	oxalic acid
PEG	polyethylene glycol
P	pressure
Po	initial pressure
P/Po	partial pressure
p-NP	*p*-nitrophenol
p-NSP	*p*-nitrosophenol
p-HAP	*p*-hydroxyaminophenol
p-QI	*p*-quinoimine
p-AP	*p*-aminophenol
R^2	coefficient of determination
s	second
SAED	selected area electron diffraction
SEM	scanning electron microscopy
SiO_2	silica
SiO_2/NC	nanocast carbon monoliths before etching silica
SiO_2/NC/Ni	nanocast carbon monoliths with nickel nanoparticles before etching silica
SiO_2/NC/1%Ni	nanocast carbon monoliths with nickel nanoparticles before etching silica (nickel loading 1 mol% with relative to the amount of FA)
SiO_2/NC/5%Ni	nanocast carbon monoliths with nickel nanoparticles before etching silica (nickel loading 5 mol% with relative to the amount of FA)
SiO_2/NC/Fe	nanocast carbon monoliths with iron nanoparticles before etching silica

SiO_2/NC/Co	nanocast carbon monoliths with cobalt nanoparticles before etching silica
TEOS	tetraethoxy silane
TEM	transmission electron microscopy
TON	turn over number
TOF	turn over frequency
UV-vis	UV-visible
wt%	weight percentage
XRD	X-ray diffraction
XPS	X-ray photoelectron spectroscopy

ACKNOWLEDGEMENTS

I am pleased to thank my family and friends who helped me to achieve this dissertation by being with me, encouraging me, and giving all the strength. I am much grateful to my supervisor, Prof. Martin G. Bakker, who tried to build a chemist by guiding for independent thinking and sharing research knowledge. His inspiring support for the research projects and the academic process is highly appreciated. I would like to thank the all dissertation committee members, Prof. Shane Street, Prof. Shanlin Pan, Prof. Paul Rupar, and Prof. Jason Bara who provided invaluable guidance throughout my carrier.

I am much thankful to the great support given by Prof. Gregory Szulczewski by teaching and guiding me on X-ray photoelectron spectroscopic analysis. I would like to thank Prof. Paulo Araujo for his collaboration and teaching on analysis of Raman spectroscopic data. The faculty members who taught in the classes and all the faculty members who helped me sharing their knowledge and instruments are greatly acknowledged.

The main instrumentation was provided by the Central Analytical Facility of the University of Alabama. Their contribution on training instruments and providing additional support whenever required are greatly appreciated.

The support of all the group members to complete this work is appreciated. I am thankful to every graduate and undergraduate student and staff members who shared knowledge and helped me during the carrier.

I am thankful to the Bakker Gift Fund for providing all the required funds for all the research projects. Finally, I would like to thank the Department of Chemistry, the College of

Art and Sciences, and the University of Alabama for all the guidance and support provided during the program.

CONTENTS

LIST OF TABLES

LIST OF SCHEMES

LIST OF FIGURES

CHAPTER 1

Introduction

1.1 Background

Porous materials can consist of one or more types of pore system. The main three types of pores are micropores, of which the diameter is less than 2 nm, mesopores, the diameter of which in the range of 2-50 nm and macropores of which the diameter is greater than 50 nm. Materials that consist of two interconnected, pore systems with different pore diameters are called hierarchically porous materials. These can be composed of either micropores and mesopores or mesopores and macropores. The advantages of such materials over those with only a single pore system are that the different pore diameters facilitate the mass transport of gas or liquid by minimizing the diffusion barriers and the enhancement of the active site distribution in catalysis.[1] The pore systems can be ordered or disordered. Ordered pore systems are periodic and generally have pores of similar size and shape over the entire material. While the disordered substances have pores of different sizes and shapes. The ordered porous materials are more interconnected as they create tubes of the same thickness but the tubes created from disordered pores have different thickness from place to place. Therefore a disordered pore system has a broader pore size distribution while an ordered pore system has a narrower pore size distribution. The porous materials can be powder or monoliths in appearance. Monolithic materials are advantageous over powder substances in many ways. In a flow system such as chromatography and catalytic reactors, the macropores minimize the diffusion barriers and facilitate the flow. The monolithic electrodes in fuel cells allow faster mass transport throughout the electrode and

monolithic catalysts can be removed easily from the reaction mixture rather than powder catalysts which need filtration to remove the catalyst. The porous materials which are researched most extensively are silica,[2] carbon,[3] metal oxides like iron oxide, tin oxide and zirconia.[4] Porous carbon materials can be synthesized via nanocasting in which a hard template like SiO_2 is used and by sol gel synthesis in which a soft template such as a surfactant or a structure directing agent is used. This dissertation discusses synthesizing metal NPs incorporated into porous carbon composites where the particles can be incorporated into nanocast materials or be formed during nanocasting of the materials.

1.2 Synthesis routes

The two main methods of synthesizing hierarchically porous carbon monoliths are nanocasting and sol gel synthesis. Nanocasting is the method of using a hard template to produce a negative replica at the nanometer scale. In brief, a liquid is infiltrated into the pores of the template, then the precursor is converted to the desired product and finally the template is removed. Nanocasting can produce powdered substances and monolithic materials. The template should have an interconnected porous system in order to get a complete replication and to retain the monolithic form. Mesoporous carbon has been synthesized by using different silica including MCM-41,[5] MCM-48,[6] SBA-1,[7] SBA-15,[8] and KIT-6.[9] Hierarchically porous carbon has been produced by using silica monoliths that have a disordered porous system.[3,10,11] Carbon precursors such as FA,[10] sucrose,[6] resorcinol[12] or phenol[13] and formaldehyde polymers have been used widely to produce mesoporous carbon.

The sol gel synthesis method uses a soft template or a structure directing reagent such as the surfactant Pluronic® F127. Hierarchically porous carbon monoliths via this method have

been reported.[14-16] In addition to the template, the method consists of a carbon precursor and a polymerization reagent. Resorcinol is the carbon source and formaldehyde is the polymerization reagent. Pluronic® F127 is the structure directing agent and 1,6-diaminohexane facilitates the formation of cross links and provides the required basicity for the polymerization. The polymerization initially occurs via a Mannich reaction.[15]

Porous carbon containing metal NPs can be synthesized in at least three different ways: (1) the direct infiltration of the metal precursor into the porous carbon substance followed by the reduction of metal salt to the metal NPs, (2) a one pot synthesis in which the metal precursor is mixed with the carbon polymer precursor(s) and porogens, and where metal NPs synthesized during the pyrolysis of carbon, and (3) nanocasting, where a metal salt is mixed with the carbon precursor and infiltrated into a porous template. Porous carbons containing metal NPs in both powder and monolithic forms have been synthesized and have been evaluated for their catalytic activity. Metal NPs such as Pd,[17] Fe,[18,19] Co,[18,19] Ni,[20] and Au[21] on powdered mesoporous carbon and Co,[16] Ni,[22,23] and Pd[24] supported on hierarchically porous carbon monoliths have been synthesized and their activity towards catalytic reactions like the "domino" carbonylations,[17] oxygen reduction reaction,[18] *p*-NP hydrogenation,[21] and for hydrogen storage[23] are described in literature.

1.3 Metal nanoparticle carbon monolithic composites via nanocasting

Hierarchically porous carbon monoliths with metal NPs have been synthesized by nanocasting. FA was used as the carbon precursor and the metal nitrate acted as the polymerization catalyst of FA, in addition to being the precursor for the metal NPs. It has been reported that hierarchically porous carbon monoliths have been prepared by nanocasting using

FA as the carbon precursor and oxalic acid as the polymerization catalyst.[3,11] But when metal nitrate is used as the polymerization catalyst the average weight of the carbon monolith is higher than when oxalic acid is used. The macropores were observed to be filled with carbon in metal nitrate catalyzed polymerization, consistent with the high carbon weight found. The micropore volume per gram of carbon decreases going from NC to metal containing NC. This could be because the volume of micropores in the carbon filling the surfactant mesopores is much higher than in the carbon of found in the macropores. These observations show a difference in the degree of polymerization when OA is used as the catalyst compared to metal nitrate. The NPs are formed during the carbonization of carbon and this is an efficient and cost effective method as additional reduction steps are not necessary to synthesize the NPs. The disadvantage of this method is the significant loss of NPs which are washed off or dissolved during the etching and washing to remove the SiO_2 template from the carbon monoliths after pyrolysis. But the loss of the number of NPs could be reduced by minimal washing after etching, although the presence of potassium ions left after the etching could alter the reaction rate if the material was used as a catalyst and the pH of the medium would change due to the presence of hydroxyl ions on the surface of the monolith. The small NPs are embedded within the mesopores while larger NPs are located at the macropore walls. The resulting monolithic nanocomposites contain metal NPs of zero oxidation state; however, the surface of the NPs is metal hydroxide as the monoliths were immersed in concentrated basic solution during the etching of SiO_2. These carbon composites are partially graphitized as the metal NPs formed during carbonization act to catalytically graphitized some of the amorphous carbon. Increasing metal loading increases the degree of crystallinity of carbon through this graphitization process. Carbon monoliths containing nickel NPs were found to be catalytically active for the reduction of *p*-NP by $NaBH_4$. *p*-QI was

observed during the *p*-NP reduction. This had previously been proposed to be an intermediate for electrochemical reduction of *p*-NP, but had not previously been reported in the catalysis literature.

1.4 Catalytic graphitization

The catalytic graphitization of hierarchically porous carbon monoliths by nickel NPs was reported in the first project as described above based on XRD and Raman data. So the second project was designed to study the catalytic effect of iron, cobalt and nickel NPs on graphitization of amorphous carbon and the temperature effect on catalytic graphitization. Catalytic graphitization is the conversion of amorphous carbon to more crystalline carbon by a chemical reaction between the ungraphitized carbon and the catalyst. Catalytic graphitization can occur mainly by two mechanisms: the dissolution-precipitation mechanism, in which carbon is dissolved into the catalyst particle and precipitates as a graphitic material, and the formation and decomposition of the carbide mechanism where carbon reacts with the metal and forms metal carbide and the metal carbide decomposes into graphite.[25] Transition metals such as Fe,[26-28] Co,[26-28] Ni,[26,28] Mn,[26] and Cr[26] and metal oxides such as MnO_2,[29,30] and Cr_2O_3[29,30] are capable of catalytically graphitizing amorphous carbon. XRD and Raman are quantitative techniques that determine the graphitization of amorphous carbon. In the XRD pattern the peak in the vicinity of the graphite (002) peak, is often used to follow graphitization. It appears as a sharp peak around 2θ of 30.99° (Co source, wavelength = 0.179 nm) and d spacing of 0.335 nm, corresponding to the distance between two polyaromatic layers in graphitic carbon. This peak appears around 2θ of 30° and d spacing of 0.346 nm in turbostratic carbon. The broad peak appears around 2θ of 28°and d spacing of 0.367 nm corresponds to the non crystalline amorphous carbon. Carbon

materials with both amorphous and turbostratic carbon give a broad peak at 2θ of 28° for amorphous carbon and a sharp peak at 2θ of 30° for tubostratic carbon. Two dimensional diffractions (10) and (11) appear around 2θ of 51° as a broad peak. A graphene layer has six membered rings of sp^2 hybridized carbon atoms linked via covalent bonds. The unit cell consists of two atoms A and B, stacking in Bernel arrangement forming multilayer graphene or graphite.[31] Van der Waals forces exist in between graphene layers. Graphite and turbostratic carbon differ as the graphene layers of turbostratic carbon may translate to each other and rotate about the normal to the graphene layers. Turbostratic carbon may have structural changes such as translation, rotation, curvature, and fluctuation of interlayer spacing of graphene layers.[31] The diffraction angle and the FWHM of the (002) peak decrease with decreasing crystallite size of both graphite and turbostratic carbon. Rotation of graphene layers in turbostratic carbon causes the intensity of three dimensional diffraction peaks such as (101) and (102) to decrease except for the instances of (00ℓ) peaks and two dimensional diffraction peaks because rotation does not affect the atomic arrangement of graphene layers.[31] The diffraction angles and FWHM of peaks are affected by structural distortion factors. Therefore they cannot be used to calculate the lattice parameters and crystallite size of turbostratic carbon.[31]

Raman spectroscopy is a non destructive technique used for the quantitative analysis on graphitization. The D peak and G peak appear in the region of 1000-2000 cm^{-1} and the overtone peaks appear in the range of 2300-3300 cm^{-1}, especially the G' peak which appears at 2700 cm^{-1} is considered for the analysis. The D peak around 1350 cm^{-1} is due to the *K*-point phonons of A_{1g} symmetry and the G peak appears in the region of 1580-1600 cm^{-1} corresponding to the zone center phonons of E_{2g} symmetry.[32,33] Furthermore, the D peak appears due to the breathing modes of sp^2 atoms in rings and the G peak appears due to the bond stretching of sp^2 atoms in

both rings and chains.[34] The area ratio of these two peaks is considered for the analysis in disordered graphite[35,36] but the intensity ratio is considered in the analysis of largely disordered carbon materials by decoupling the information on intensity and FWHM.[32,33] I_D/I_G is the principle quantity used to evaluate the graphitization while the FWHM is also considered. The intensity ratio is expected to increase with increasing disorder of graphite and it is proportional to $1/L_D$, where L_D is the distance between two defects and when L_D is approximately equal to, or greater than 2 nm. This is because the D peak gets activated in the presence of disorder. On further disordering in which L_D is less than 2 nm, the intensity ratio decreases proportionally to L_D^2, because I_D is proportional to the total number of defects.[32] The relative motion of the sp^2 atoms in carbon contributes to the I_G. As the number of defects increases the sp^2 domains become smaller and hexagons become fewer and more distorted and ultimately rings open. I_D is proportional to the presence of sp^2 rings. Therefore, I_D decreases and I_D/I_G decreases.[32,33] We have demonstrated that the I_D/I_G ratio of NC and NC with Fe, Co and Ni NPs increases with increasing temperature of pyrolysis. Thermal energy favors the clustering of sp^2 phase to ordered rings.[32] I_D is directly proportional to the number of ordered rings and clustering of rings. Therefore I_D increases with increasing temperature. The G peak relates to bond stretching of all sp^2 pairs[32] and its intensity does not change. Therefore, I_D/I_G ratio increases with increasing temperature.

The second order Raman spectral features appear as a broad peak in amorphous carbon while peaks can be differentiated in more graphitic carbon.[32] The G' peak appears at 2700 cm^{-1} of the second order Raman spectra corresponds to the first overtone of the D peak.[37] This peak appears as a single Lorentzian peak in turbostratic carbon similar to monolayer graphene due to the absence of interlayer interactions between graphene layers.[38] The G' peak appears as two

peaks in highly oriented pyrolytic graphite.[38] Amorphous carbon turns to turbostratic carbon on catalytic graphitization with increasing temperature. This is illustrated in our work that the G' peak becomes more prominent as a single peak and the FWHM decreases with increasing temperature especially in metal loaded NC.

TEM is another technique that is used to analyze graphitization qualitatively and quantitatively. TEM images show the amorphous carbon region and the turbostratic carbon regions. They indicate the nanoparticle distribution with respect to the graphitic and turbostratic regions. HRTEM images show the polyaromatic layers of turbostratic or graphitic region and the distance between lattice fringes can be used to evaluate whether the formed crystalline carbon is turbostratic or graphitic as described in the XRD section. The SAED pattern shows the diffraction rings and that can use to determine the formed carbon is turbostratic or graphitic. If it is turbostratic carbon only the (002), (10), and (11) rings are present. In addition to those diffraction rings in graphitic carbon (004), (103), (101), (112), and (110) diffraction rings are also present.[39]

1.5 Au NPs supported on hetoroatom rich mesoporous carbon

The first chapter discusses on the catalytic activity of nickel NPs incorporated hierarchically porous monolithic carbon on reduction of *p*-NP. The third project was designed to determine the catalytic activity on oxidation of benzyl alcohol by Au NPs supported on mesoporous carbon because catalysis is a major application of metal NPs supported porous carbon. Mesoporous carbon functionalized with heteroatoms such as oxygen and nitrogen provide active sites for catalysis.[40] The functional groups like COOH, C-O-C and C-N provide binding sites for Au NPs. Therefore Au NPs immobilizing on functionalized carbon result in efficient catalysts. Carbon produced by using FA as the carbon precursor for nanocasting, has

oxygen functional groups such as C-O, C=O, and OH and when furfuryl amine is used as the carbon precursor it gives carbon with nitrogen functional groups like pyrolic nitrogen and oxidized nitrogen in addition to the above mentioned oxygen containing functional groups. $HAuCl_4$ the Au precursor was introduced to porous carbon by the incipient wetness method and was reduced in 5% H_2/N_2 to produce Au NPs. The catalysts synthesized by incorporating Au NPs onto such functionalized mesoporous carbon have proven to be efficient catalysts for benzyl alcohol oxidation.

CHAPTER 2

One Pot Synthesis of Carbon/ Ni Nanoparticle Monolithic Composites by Nanocasting and their Catalytic Activity on 4-Nitrophenol Reduction

2.1 Abstract

Composites of nickel NPs incorporated in hierarchically porous carbon monoliths, with varying Ni loading were synthesized by a one-pot, nanocasting pathway in which the carbon and nickel were produced in a single step. TEM and SEM images of the composites show well dispersed NPs in the carbon matrix with small NPs of about 4-12 nm located within the mesopores and larger NPs (20-60 nm) located in the macropores. The NPs are unevenly distributed on the mm scale within the monolith. The surface area and the mesopore volume of the carbon determined by nitrogen adsorption decreased with increasing metal loading. XRD suggests the NPs are metals at zero oxidation state but XPS shows the presence only of $Ni(OH)_2$. Raman spectra show a significant increase in carbon crystallinity with increasing metal loading. The composites were used to catalyze the reduction of *p*-NP to *p*-AP. The intermediate *p*-QI was identified by GC-MS.

2.2. Introduction

NPs show different catalytic properties than the bulk material as the Fermi potential is more negative, facilitating electron transfer.[1,2] However, they show inactivity and low selectivity as they tend to aggregate due to their high surface energy which results from large surface to

volume ratio.[3] NPs need to be stabilized and this can be done by incorporating them onto a support.[4] Different kinds of supports such as SiO_2,[4] MgO,[5] ZrO_2,[6] and Al_2O_3[7] are available but porous carbon has advantages due to the high surface area which facilitates the electron transfer. Porous carbons have attracted tremendous interest as catalyst supports,[8] for adsorption of dyes,[9] and for hydrogen storage,[10] as they are thermally and chemically stable.[11]

SiO_2 has been used as the template to synthesize porous carbon as powder or monolith, a process often referred to as nanocasting. Ryoo et al. have produced ordered mesoporous carbon powders, CMK-3 and CMK-5, that have different mesostructures.[12,13] Smätt and et al. have reported synthesis of carbon monoliths using disordered mesoporous SiO_2 as the template and FA as the carbon precursor.[14-16] Recently there has been interest in obtaining metal NPs contained in porous carbon via a one-pot synthesis method in which NPs are formed during the carbonization of the carbon. Metals such as Pd,[17] Co,[18] Fe,[18] and Ni[19] incorporated into mesoporous carbon materials have been extensively studied for their applications in catalysis. Other methods of making Ni NPs/carbon composites include using phenolic resol,[20] resorcinol-formaldehyde polymers,[21] and chitosan[19] as carbon precursors.

Here we report a novel procedure to synthesize carbon monoliths containing Ni NPs by a one pot synthesis via a nanocasting pathway. Monolithic catalysts can be much more easily removed from a reaction mixture than powdered catalysts, and can also be used as fixed bed catalysts. Most of the studies reported so far are of composites in powder form and have shown the appearance of the NPs on the exterior surface or in the pore walls of the carbon.[19,20] Carbon monoliths with Ni NPs have been synthesized by a sol-gel method.[22,23] Such one pot synthesis methods are faster as the NPs are synthesized during the preparation of carbon, but generally yield significantly larger NPs than we report here. Our study demonstrates that NPs of size about

4-12 nm are embedded in the mesoporous structure while the larger NPs are located in the macropores of the porous carbon. We have applied these new composite materials as catalysts for the chemical reduction of *p*-NP.

p-NP is a pollutant found in industrial and agricultural wastes that needs to be removed.[24] The reduction of *p*-NP can be carried out in many ways including metal/acid reduction, electrolytic reduction and catalytic hydrogenation. The metal/acid reduction requires strong acidic media and has low selectivity, and electrolytic reduction requires acidic or basic electrolytes. Catalytic hydrogenation yields high conversion with high efficiency and less impact on the environment.[25] *p*-NP reduction has been used as a model reaction for investigating the catalytic activity of new catalysts and is generally believed to be well understood mechanistically.[19,26,27]

2.3. Experimental

2.3.1. Materials

PEG 35,000, HNO_3 70%, KOH, *p*-NP and $NaBH_4$, ethanol 95% were procured from VWR. NH_4OH 29% was purchased from Fisher Scientific. FA 98% was purchased from Acros Organics. TEOS 98%, anhydrous OA 98% and $Ni(NO_3)_2.6H_2O$ 98%, were purchased from Alfa Aesar. C_{18}TAB was obtained from Genescript. All chemicals were used as received without further purification.

2.3.2 Catalyst Synthesis

2.3.2.1 Synthesis of SiO_2 monoliths

SiO_2 monoliths were synthesized according to a literature procedure.[28] In a typical synthesis PEG 35,000 (2.2 g) was dissolved in 33 mL of 18 MΩ water with magnetic stirring and 6.5 mL of 30% HNO_3 added to the stirring mixture. TEOS (32 mL) was then added and stirring was continued until a uniform solution was obtained. C_{18}TAB (5.5 g) was then added and the mixture was stirred until all surfactant had dissolved. The resulting mixture was degassed and was poured into well plates that were covered with parafilm. The well plates were incubated at 40 °C for 3 days. Then the monoliths were removed from the well plates and put into a 1 M NH_4OH solution and incubated at 90 °C for 15 h. The monoliths were then washed with 0.1 M HNO_3 and dried at 40 °C for 3 days followed by calcination at 550 °C for 5 h at a heating rate of 1 °C min^{-1}.

2.3.2.2 Synthesis of NC monoliths

SiO_2 monoliths were degassed for 2 h prior to use. FA was diluted in ethanol in which OA was dissolved. The molar ratio of FA and OA was 100:1 and the volume ratio of FA to ethanol was 5:1. Degassed SiO_2 monoliths were added to the above mixture and were allowed to infiltrate overnight. After excess solution was removed by drying on copier paper, the monoliths were incubated at 75 °C for 1 day to polymerize the FA. The infiltration and polymerization steps were repeated once. After the polymerization, the monoliths were heated to 600 °C in 4 h and held at 600 °C for 2 h under N_2 flow. The obtained SiO_2/NC monolithic composites were immersed in 3 M aqueous KOH at 75 °C for one day in order to remove the SiO_2 and the etched monoliths were dried at room temperature.

2.3.2.3 Synthesis of NC/Ni monoliths

Ni was included as a molar percentage (1% and 5%) relative to the FA. $Ni(NO_3)_2.6H_2O$ (0.0375 g for 1% Ni and 1.675 g for 5% Ni for 10 mL of FA) was dissolved in a mixture of ethanol (2 mL) and FA (10 mL). SiO_2 monoliths were degassed for 2 h prior to use. Then the ethanol/FA mixture was introduced to the SiO_2 monoliths by impregnation and was incubated at room temperature overnight. After removal of excess solution by rolling the monoliths on copier paper, the composites were heated at 90 °C for 15 h to polymerize the FA. The infiltration - polymerization cycle was repeated once in order to enhance the homogeneity of the polymer. Pyrolysis, etching and drying were then carried out in a similar fashion to the procedure described above. The amount of nickel incorporated in the carbon was determined by leaching a monolith overnight in 24 ml of aqua regia, diluting with water as necessary and determining the nickel concentration by Atomic Absorption spectrometry on a HP Instruments AAnalyst 400 system. The AAS measurements were carried out in triplicate, and the average of duplicate analyses reported (i.e. on two separate monoliths for each composition).

2.4. Characterization

XRD patterns of the samples were collected with a Bruker D8 Discover with GADDS (Wavelength Co Kα, 1.79 Å) and a Hi-Star area detector. TEM images of the samples were obtained on a FEI Tecnai F20, equipped with a cold field emission gun and a super twin objective lens with an accelerating voltage of 200kV. Samples were prepared on holey carbon supported by a copper grid. SEM images were collected using a JEOL 7000 FE-SEM operated at 30 kV, with diode based back-scatter electron detector and an Oxford EDS detector for elemental analysis. XPS spectra were acquired on a Kratos Axis 165 XPS that is operated with a dual

Mg/Al anode and a monochromatic X-ray source at 1486.6 eV, corresponding to the Al K_α line. Photoelectrons were collected with a takeoff angle of 90° relative to the sample surface. The survey and high resolution XPS spectra were acquired in order to determine the chemical states of C, O and Ni and to determine the relative atomic ratios. The survey spectra and high resolution spectra of NC were taken at a pass energy of 160 eV, with a step size of 0.1 eV and using a single scan. The dwell time for the survey scan was 500 ms and 1000 ms for the high resolution spectra. The survey spectra and the high resolution spectra of NC/Ni were taken at a pass energy of 320 eV, step size of 0.1 eV and using one scan. The dwell time for the survey scan was 125 ms, and 5000 ms for high resolution spectra.

Raman spectra were acquired using a Jobin-Yvon Horiba confocal Raman microscope. The excitation source used was the 632.81 nm line from a HeNe laser with a power of approximately 12 mW at the sample and the 10x objective was used. Raman spectra were acquired in the region of 1000 cm^{-1}- 2000 cm^{-1} and the spectral acquisition time was 32 min for all samples. N_2 sorption measurements were taken on a Quantachrome Nova 2200e pore size analyzer at -197 °C with He mode to determine surface areas and void volumes of the monoliths, respectively. The interpretation of the isotherms was carried out with Quantachrome's Nova Win software version 11.0 using a multipoint BET method[29] to determine the surface areas, and the BJH method[30] was applied to the adsorption branch to determine the pore size distribution. The volume of micropores was determined by the t-plot method. Product analysis was carried out on a HP6890 GC using a Micromass Auto-spec Ultima^{TM} NT mass spectrometer equipped with a Zebron 2B-5MS, 30 m x 250 µm x 0.25 µm, column.

2.5. Catalytic activity

The catalytic activity of the synthesized composites was investigated by using the reduction reaction of *p*-NP to *p*-AP by $NaBH_4$. Catalyst (NC/1%Ni, NC/5%Ni and NC) was powdered and was dispersed in water by sonication with a catalyst concentration of 1 mg/ml. $NaBH_4$ (100mM) was dissolved in 0.5 ml of this suspension, and was quickly added to 3.5 ml of 60 µM *p*-NP, in a quartz cuvette. The cuvette was placed in a UV-vis spectrometer equipped with a magnetic stirrer. Experiments on dye adsorption to the catalyst were carried out in the same way but the powdered composite was dispersed in a basic solution without $NaBH_4$, in which the pH was adjusted by addition of NaOH solution to the same pH value as when $NaBH_4$ is present. Time resolved UV-vis spectra were collected while stirring the solution in the cuvette. The reactions were monitored by a Cary 100 Bio UV-vis spectrophotometer in the range of 250-600 nm.

The conversion and selectivity were evaluated by GC-MS. The concentration of *p*-NP used for the reaction was 1 mM, the same molar ratio of *p*-NP to $NaBH_4$ as used in the UV-vis study. The catalyst was used as whole monoliths. To identify the intermediates by GC-MS, the reaction was carried out and samples were taken out at various times during the course of the reaction.

2.6 Results

2.6.1 Material Characterization

All monolithic materials had a length of about 7 mm and diameter of about 5 mm, and were cylindrical as shown in Figure **2.1**. They were stable, and upon etching shrinkage in the carbon monoliths was negligible. The average mass of the monoliths was found to be 0.022 g for NC, 0.048 g NC/1%Ni, and 0.079 g for the NC/5%Ni.

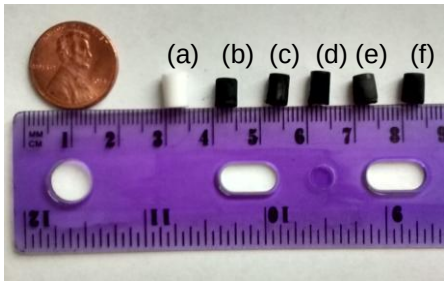

Figure (2.1). Representative photo of the monoliths studied, (a) SiO_2, (b) SiO_2/NC, (c) SiO_2/NC/1%Ni, (d) SiO_2/NC/5%Ni, (e) NC/1%Ni, (f) NC/5%Ni. An American one cent coin is shown to indicate the scale.

SiO_2 was used as the template to prepare NC monoliths and NC/Ni monolithic composites as it has an interconnected porosity that facilitates the structural integrity of the produced monoliths after removal of SiO_2 by base etching.[14,31] The SEM images in Figure **2.2a** show the macropore structure of the SiO_2. Figures **2.2b**, **c** and **d** show that the carbon formed retains the macropore structure of the SiO_2, i.e. that a positive replica is formed, as is expected from earlier work.[15,16]

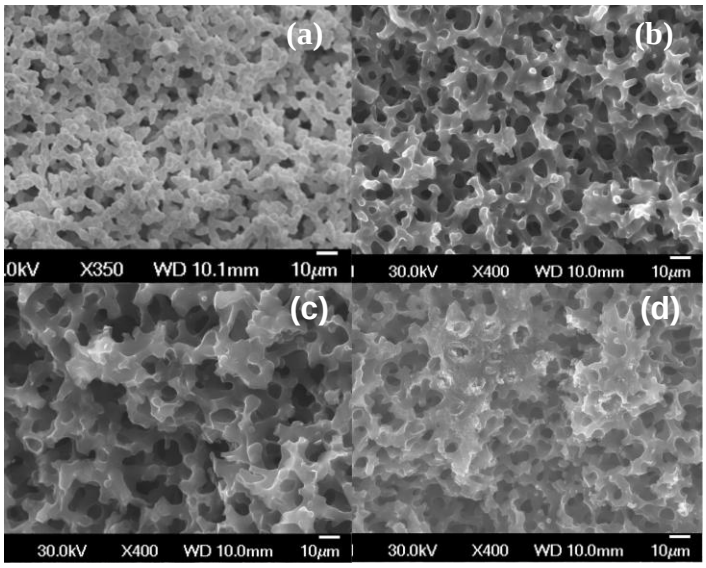

Figure (2.2). SEM images of (a) SiO_2, (b) NC, (c) NC/1%Ni, (d) NC/5%Ni.

However closer inspection of Figure **2.2d** especially shows that there is considerably more carbon present in the macropores for the NC/5%Ni sample than for the NC or NC/1%Ni samples. This is consistent with the larger masses of the monoliths found for the NC/1%Ni and NC5%Ni samples relative to the NC sample.

The N_2 sorption isotherms of SiO_2, SiO_2/NC, NC, SiO_2/NC/1%Ni, SiO_2/NC/5%Ni, NC/1%Ni and NC/5%Ni are given in Figure **2.3a** and **b**, and the pore size distribution in Figure **2.3c** and **d**. The values determined from nitrogen adsorption are summarized in Table **2.1**. The SiO_2 monolith used as template has three types of pores[28] (1) surfactant mesopores generated by the surfactant added during the synthesis, (2) textural mesopores resulting from the ethylene glycol polymer and condensation of SiO_2 particles and (3) macropores resulting from spinodal decomposition of the SiO_2 sol mixture. The isotherm for SiO_2 shows the two regions of N_2 uptake. The first region appeared around P/Po = 0.4, and is due to the surfactant mesopores. The second one, which appeared around a relative pressure of 0.9 is due to the filling of textural mesopores.[15] The isotherm for SiO_2/NC shows a weak N_2 uptake around P/Po = 0.4 consistent with almost complete filling of the surfactant mesopores by carbon. The second, even smaller N_2 uptake around a relative pressure of 0.9, shows that most of the textural mesopores are also filled by carbon. The reappearance of the loop around relative pressure 0.4 in the isotherm for NC indicates that upon etching, replication of the surfactant mesopores in the template has produced mesopores in the NC. The relatively high volume around relative pressure 0.9 shows that upon etching, replicas of some of the SiO_2 textural mesopores have also been created. The BJH pore size distribution has a relatively narrow maximum of 3.4 nm for SiO_2, which is consistent with the CTAB used as porogen to make the silica. The maximum of the pore size distribution for NC is at about 3.4 nm, but the pore size distribution is much broader than for the parent silica

monolith. This is consistent with earlier work,[14,32] as the surfactant mesopores are randomly spaced rather than an ordered array, and so the SiO_2 walls have variable thickness. Nanocasting gives a negative replica at the nanoscale, producing a broader mesopore size distribution. The isotherms for SiO_2/NC/1%Ni and SiO_2/NC/5%Ni show that the uptake due to the surfactant mesopore filling at low pressures and textural mesopore filling at high pressures have disappeared indicating that in these samples both the surfactant and textural mesopores were completely filled with carbon. This is consistent with the BJH pore size distributions (Figure **2.3c** and **d**) as they also illustrate that the surfactant mesopore peak at around 3.4 nm diameter has essentially disappeared in both SiO_2/NC/1%Ni and SiO_2/NC/5%Ni. The total pore volume and mesopores and micropore volumes of SiO_2/NC/5%Ni are all somewhat smaller than those of SiO_2/NC/1%Ni. Upon etching, the nitrogen uptake corresponding to replication of the surfactant mesopores appears. As with the NC samples, the BJH pore size distribution curves show that mesopores have been shifted to higher pore size in NC/1%Ni and NC/5%Ni, approximately 4.4 nm and 3.2 nm respectively, with a significantly broader pore size distribution.

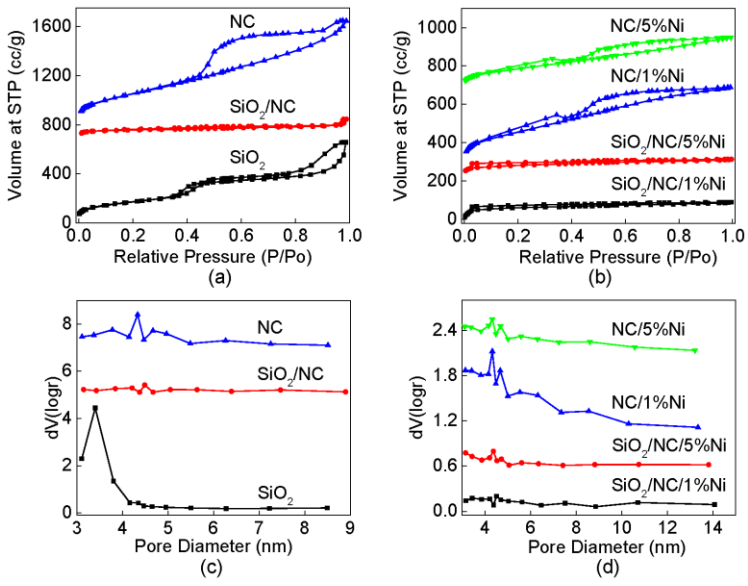

Figure (2.3). (a) N_2 sorption isotherms of SiO_2, SiO_2/NC, NC, (b) N_2 sorption isotherms of SiO_2/NC/Ni and NC/Ni composites, BJH pore size distribution curves of (c) SiO_2, SiO_2/NC, NC, (d) SiO_2/NC/Ni and NC/Ni.

Interestingly on a per monolith basis the volume of mesopores is actually higher in the Ni containing monoliths than in the OA templated monoliths. This is consistent with largely complete filling of the surfactant mesopores for the Ni containing monoliths, with the extra carbon filling the macropores and contributing proportionately fewer mesopores per gram.

The increasing growth of carbon in the macropores with increasing amount of Ni may be due to faster polymerization induced by Ni catalysis compared to OA. The observation that the samples all have approximately similar volumes of mesopores (on a per monolith basis) suggests that the Ni/FA solution completely fills and replicates the surfactant mesopores of the SiO_2 template. And that excess FA polymer is trapped in the macropores.

The SiO_2 template has little microporosity, whereas NC is observed to contain significant amounts of micropores. Interestingly, the micropore volume on a per gram basis drops significantly for NC/1%Ni and further for NC/5%Ni. It is possible that this results from carbon formed in the surfactant mesopores having higher microporosity that carbon formed in the macropores. However, it seems more likely, that this difference reflects a difference in the degree of polymerization and nature of the polymer formed by OA catalysis of FA compared with that from Ni catalysis. Alternately it could be a reflection of the impact of Ni NPs on the graphitization of the carbon formed, as such graphitization would be expected to remove micropores.

Table **2.1.** Textural parameters of SiO_2, SiO_2/NC, NC, SiO_2/NC/1%Ni, SiO_2/NC/5%Ni, NC/1%Ni, and NC/5%Ni.

Sample	BET Surface are (m^2/g)	Total Pore Volume (cc/g)	Mesopore Volume (cc/g)	Micropore Volume (cc/g)	BJH Method Adsorption Pore Diameter (nm)
SiO_2	615	0.54	0.54	0.00	3.4
SiO_2/NC	438	0.25	0.10	0.15	4.4
NC	1247	0.88	0.84	0.04	4.4
SiO_2/NC/1%Ni	196	0.12	0.12	0.00	3.4
SiO_2/NC/5%Ni	114	0.07	0.07	0.00	3.2
NC/1%Ni	923	0.62	0.53	0.09	3.2
NC/5%Ni	540	0.36	0.30	0.06	3.2

The wide angle XRD pattern of NC shows only a broad peak from (002) scattering of amorphous carbon and a weak peak from scattering from the (10) and (100) planes (Figure **2.4a**). Peaks corresponding to the (111), (200) and (220) reflections of metallic Ni which appear at 52.31°, 61.14° and 91.87° were present in both NC/1%Ni and NC/5%Ni samples (Figure **2.4b** and **c**). Scherrer analysis was performed for NC/1%Ni, and NC/5%Ni to determine the size of the Ni crystallites. The average crystallite size calculated from the (111), (200) and (220) reflection peaks for NC/1%Ni is 3.7 nm, and for NC/5%Ni it is 24.37 nm, showing the increase average in crystallite size with increasing amount of Ni. A sharp peak corresponding to the (002) reflection of carbon could be seen at 30.5° indicating that higher metal loading increases the graphitization of carbon.

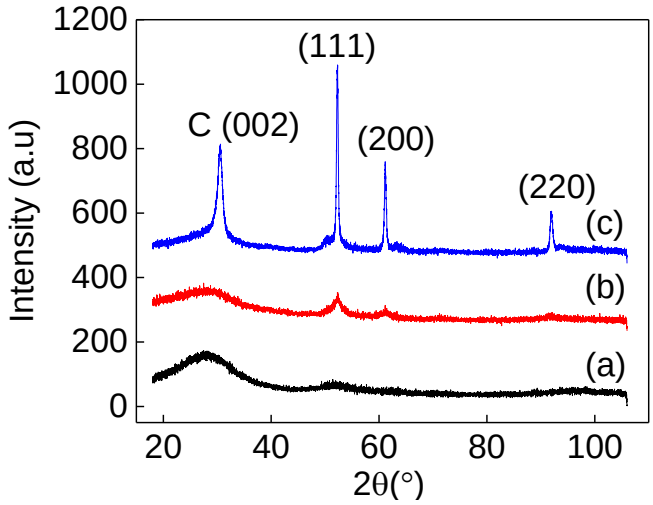

Figure (2.4). Wide angle XRD pattern (a) NC (b) NC/1%Ni and (c) NC/5%Ni.

The high resolution XPS spectrum of C 1s for NC (Figure **2.5a**) shows graphitic C at 284.30 eV.[33] In addition it shows the peak due to C bound to O by a single bond at 286.25 eV and C in an ester at 289.18 eV.[34] The peak that appeared at 292.30 eV can be attributed to the shake-up peak of C 1s. The high resolution spectrum of O 1s (Figure **2.5b**) illustrates the presence of O bound to C via single and double bonds at 532.40 eV and 531.42 eV, respectively. The peak at 533.34 eV can be attributed to hydroxyl groups. The high resolution spectra of Ni 2p show $2p_{3/2}$ and $2p_{1/2}$ peaks due to spin orbital coupling in both NC/1%Ni and NC/5%Ni as seen in Figure **2.5c** and **d,** respectively. The $2p_{3/2}$ appeared at 856 eV and the shake-up line at 862 eV. The positions of these peaks are consistent with the formation of $Ni(OH)_2$.[35] As the monoliths were immersed in 3M KOH to remove SiO_2 it seems likely that $Ni(OH)_2$ could form on the surface of nanoparticles. Sodium borohydride is a sufficiently strong reductant to reduce $Ni(OH)_2$ and so the presence of a surface nickel hydroxide is unlikely to impact the catalytic properties. According to the quantification that was performed using the integrated peak areas, the percentage of Ni relative to C in NC/1%Ni of 0.12 at% and in NC/5%Ni of 0.32 at%. These

compositions would correspond to approximately 0.59 wt% and 1.57 wt%. These are significantly different than the composition determined by leaching of the metal in aqua regia and determination by atomic adsorption spectrometry which gives values of 1.7 wt% for NC/1%Ni and 4.6 wt% for the NC/5%Ni samples. The surface nature of XPS makes it particularly prone to contamination by dust and other atmospheric pollutants that tend to include substantial amounts of carbon. Accordingly we have used the compositions determined by AAS in subsequent calculations. The proportionally higher incorporation of nickel in the NC/1%Ni sample compared to the NC/5%Ni sample is likely to result from the adsorption of nickel on the SiO_2 surface, which acts to concentrate nickel inside the monoliths. Excess solution is used it is rather than an incipient wetness procedure, providing a pool of nickel/FA from which the nickel can be concentrated.

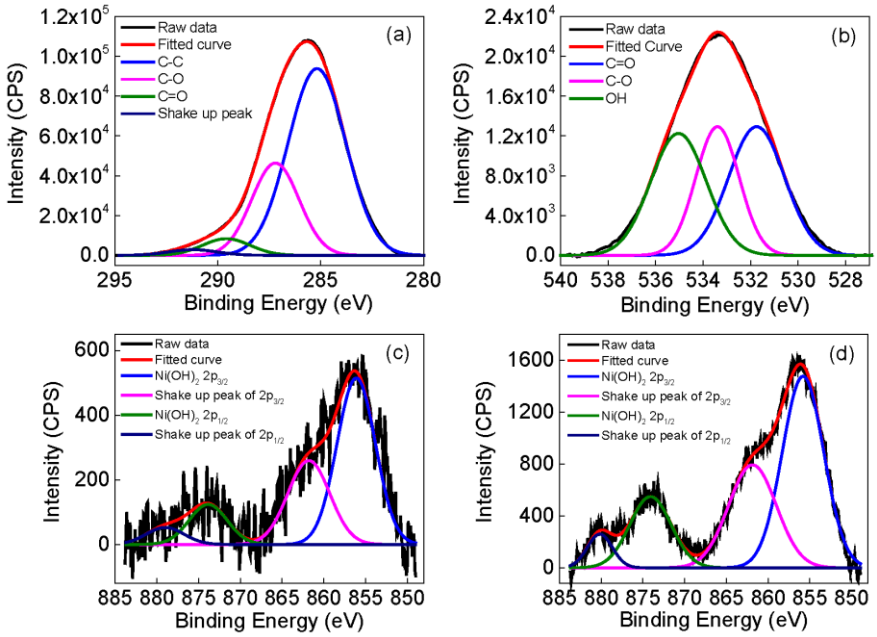

Figure (2.5). High resolution XPS spectra of NC (a) C 1s (b) O 1s, (c) Ni 2p of NC/1%Ni (d) Ni 2p of NC/5%Ni.

Raman spectroscopy is a useful tool to characterize carbon materials as it provides information on the extent of graphitization. Figure **2.6** shows the Raman spectra of NC (Figure **2.6a**), NC/1%Ni (Figure **2.6b**) and NC/5%Ni (Figure **2.6c**) in the 1000 cm^{-1} to 2000 cm^{-1} region. The D peak, which is related to the concentration of defects, appeared around 1330 cm^{-1} and the G peak from sp^2 carbon is related to ordered graphene sheets appeared around 1590 cm^{-1}. The ratio of intensities of D and G peaks were determined by fitting the D and G peaks to Lorentz curves by using Peak Fit 4.1. I_D/I_G in metal free NC is 0.75, in NC/1%Ni it is 0.96 and it is 1.24 in NC/5%Ni. For well-ordered graphitic carbon the I_D/I_G ratio decreases with increased ordering, however for amorphous and poorly order carbons, when the distance between defects is less than ~3 nm, the I_D/I_G peak increases with increased ordering. So the increase in the I_D/I_G ratio with increased metal loading can be attributed to increased formation of nanocrystalline graphite.[36]

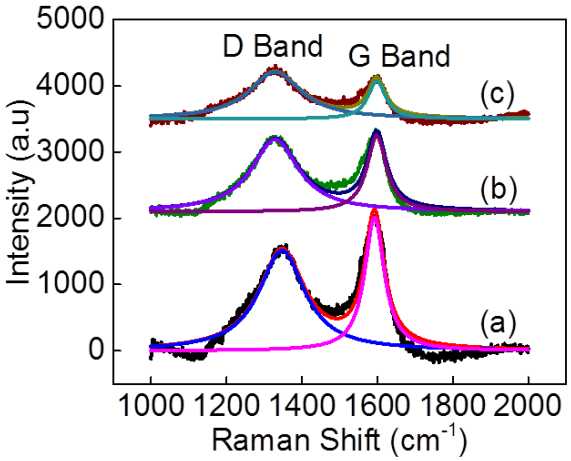

Figure (2.6). Raman spectra of (a) NC (b) NC/1%Ni and (c) NC/5%Ni.

The disordered nature of the mesopore structure of the SiO_2 template can be seen in the TEM image. TEM images of NC are consistent with the mesopores formed being a negative replication of the SiO_2 template.[14] The TEM images of SiO_2 and NC can be found in appendix A.

TEM images of NC/1%Ni and NC/5%Ni are given in Figure **2.7**. These images show that the NPs are dispersed in the carbon support. TEM and HRTEM images were taken by tilting the sample holder by 0° (Figure **2.7**). By tilting the sample holder at $+15^{o}$ and -15^{o} it was possible to confirm that the small Ni NPs are embedded within the mesopores as their position did not change relative to the matrix on tilting. However, the larger particles observed were likely located outside the mesopores. On changing the tilt angle these particles moved substantially relative to the carbon structure and so were not incorporated in the carbon, but rather were located on the surface of the carbon, consistent with a location in the macropores. The TEM images taken by tilting the sample holder are given in appendix A. The Ni particle size in NC/1%Ni showed significant variation from image to image in the ground monoliths. A particle size distribution generated from all the various images is given in appendix A. The mean particle size found was 9 nm. The density of particles in NC/5%Ni observed by TEM is much lower than that found for NC/1%Ni. The mean Ni NP size found for NC/5%Ni was 47 nm, significantly larger than in NC/1%Ni.

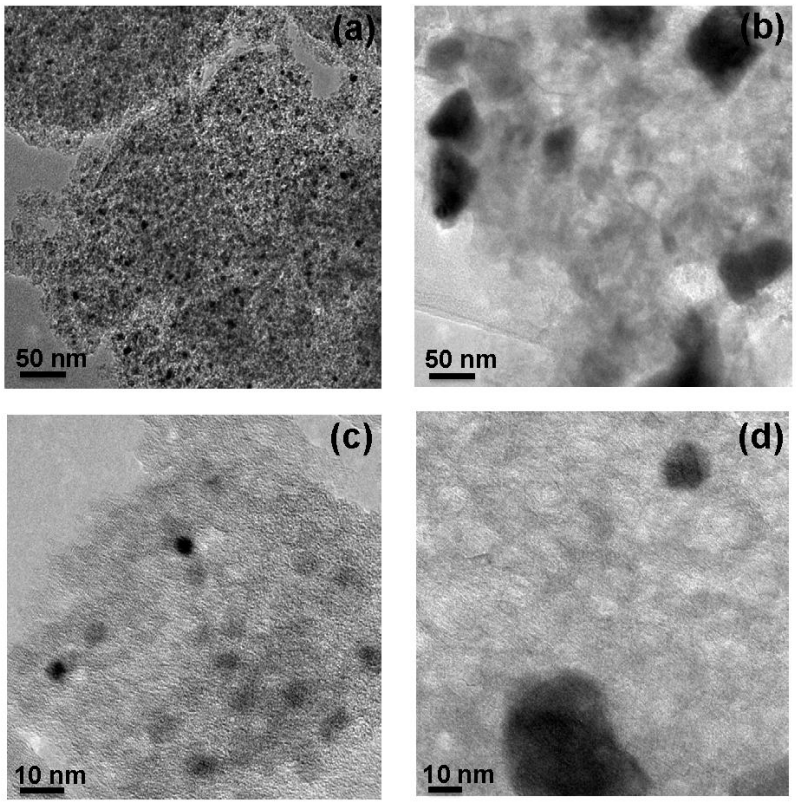

Figure (2.7). TEM images of (a) NC/1%Ni (b) NC/5%Ni tilt 0°, HRTEM images of (c) NC/1%Ni (d) NC/5%Ni tilt 0°.

HRSEM images (Figure **2.8**) were taken in an area at the center (Figure **2.8a** and **c**) and in an area close to the edge (Figure **2.8b** and **d**) of the monolith in order to observe the spatial distribution of the particles in the monoliths, respectively in NC/1%Ni and NC/5%Ni, by using the back scatter detector (COMPO). From the SEM images it can be seen that the NPs are not evenly distributed in the carbon framework of both NC/1%Ni and NC/5%Ni. It appears likely that this unevenness in distribution is a result of interaction between the Ni salt and the SiO_2 of the template during infiltration. SiO_2 is negatively charged and Ni^{2+} is positively charged. Ni^{2+} ions are therefore likely to be strongly adsorbed onto the SiO_2 and a chromatographic effect would then produce an uneven distribution through the monolith. The heterogeneity is then

reflected in an uneven spatial distribution of NPs. These images also clearly show that the large NPs of about 53 nm and 61 nm respectively in NC/1%Ni and NC/5%Ni are located on the macropore walls.

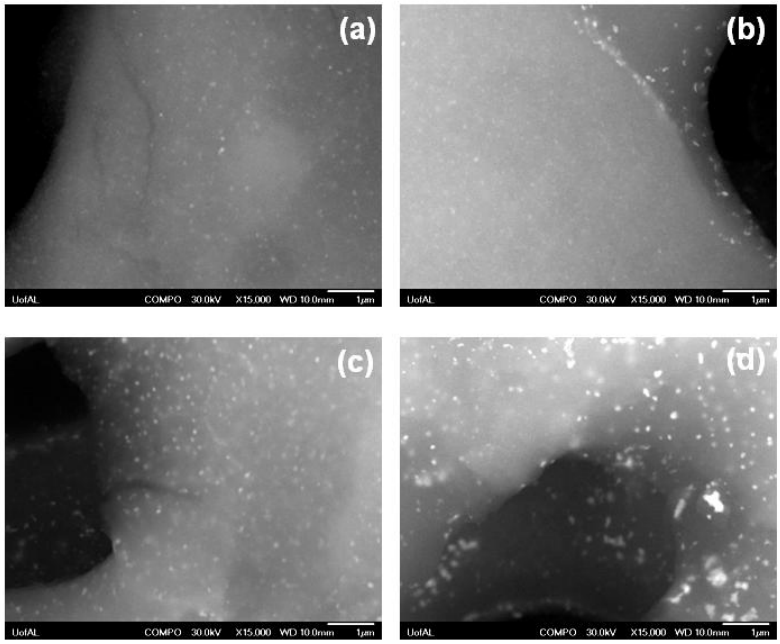

Figure (2.8). SEM images of NC/1%Ni (a) center (b) outside, NC/5%Ni (c) center (d) outside.

2.6.2 Catalytic activity

The reduction of *p*-NP to *p*-AP has become a common model reaction to evaluate the catalytic activity of NPs and nanocomposites. The reduction is thermodynamically feasible as E_0 for *p*-NP/ *p*-AP = -0.76V and H_3BO_3/BH_4^- = 1.33V versus NHE, but is not kinetically favorable without a catalyst.[26] *p*-NP has an absorbance maximum at 317 nm and upon addition of $NaBH_4$ the absorbance maximum shifted to 400 nm due to the formation of *p*-nitrophenolate ions in the basic medium.[37] UV-vis spectra were recorded over time and the reduction of the *p*-nitrophenolate ion was monitored. The only product, *p*-AP, can also be monitored, as it gives a new peak at 300 nm. Figures **2.9a** and **2.9b** are absorbance vs. wavelength plots as a function of

time for NC/1%Ni and NC/5%Ni, respectively. *p*-Nitrophenolate ions are potentially subject to adsorption in addition to reduction by $NaBH_4$. To check for this, dye adsorption was monitored in the absence of $NaBH_4$, with the pH adjusted to match the pH when $NaBH_4$ was present. Figure **2.9c** shows the absorbance of *p*-nitrophenolate in the presence of NC over the same time span that the catalytic reaction was monitored. Some fluctuation in the absorbance was observed, but no net adsorption or reaction of nitrophenolate occurred.

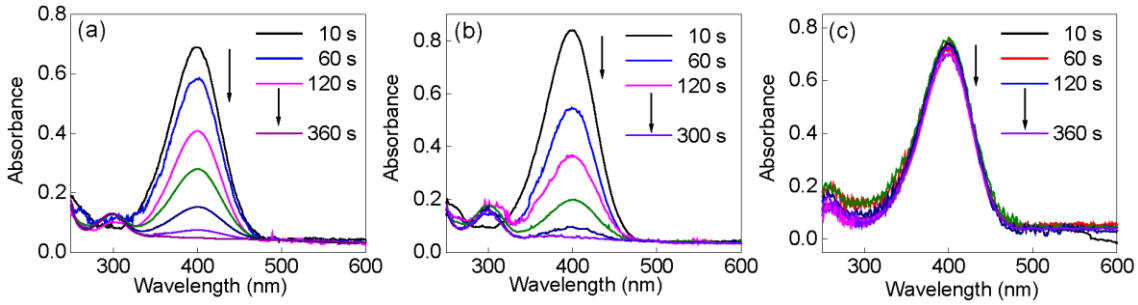

Figure (2.9). UV-vis absorption spectra of *p*-NP dye in the presence of $NaBH_4$ (a) NC/1%Ni, (b) NC/5%Ni, and (c) NC.

The $NaBH_4$ concentration is much greater than that of *p*-NP, and so the rate of reaction is effectively zeroth order in $NaBH_4$ concentration, and the reaction is considered to follow pseudo-first-order kinetics with respect to *p*-NP, i.e. $C=C_0e^{-kt}$, where k is the pseudo-first-order rate constant, C and C_0 are concentration of *p*-nitrophenolate at times, t and 0, respectively. The concentration is directly proportional to the absorbance. Figure **2.10** shows the absorbances measured at 400 nm as a function of time. The curves shown are exponential fits to the observed absorbances. The rate constants, 95% confidence limits and the R^2 values are tabulated in Table **2.2**. As can be seen in Figure **2.9** there is no net change of dye absorbance indicating that there is no adsorption of dye onto the NC and that the NC has no catalytic activity.

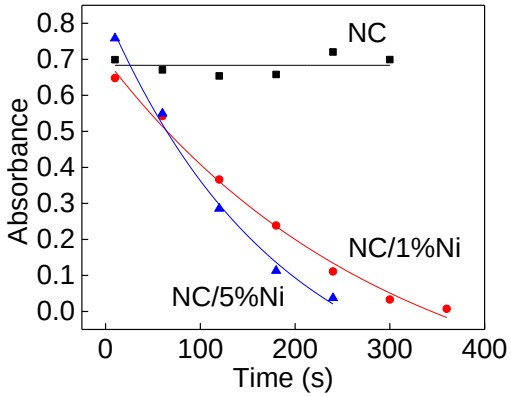

Figure (2.10). Absorbance vs. time of NC, NC/1%Ni, and NC/5%Ni.

Table **2.2.** Rate constants, 95% confidence limits and R^2 values on catalysis.

Sample	Rate constant (s^{-1})	95% confidence limit	R^2
NC/1%Ni	1.03×10^{-2}	$\pm 4.1 \times 10^{-3}$	0.91
NC/5%Ni	1.25×10^{-2}	$\pm 3.3 \times 10^{-3}$	0.95

The primary product observed by GC-MS was *p*-AP (m/z 109). p-QI (m/z 107) was also observed. The GC-MS spectra of *p*-AP and *p*-QI are given in appendix A. The GC-MS experiments support the results obtained from UV-vis as both the catalysts were found to completely convert *p*-NP to *p*-AP with no other products being observed. Moreover, as the reactions for GC-MS were carried out by using the catalysts as monoliths and, the powdered form was used for the kinetic evaluation, it demonstrates that the catalyst can be used in both forms.

The TON and TOF are important parameters in comparing the catalysts synthesized. The TON is the number of reactant molecules that are converted to products by 1 g of nickel, and TOF is TON/time.[1] The TOF values of NC/1%Ni and NC/5%Ni were found to be 6.5×10^{-5}

moles g^{-1} s^{-1} and 2.84 x 10^{-5} moles g^{-1} s^{-1}, respectively. The higher TOF for NC/1%Ni compared to that for NC/5%Ni is consistent with the small difference in the rate constants found for the two catalysts and the higher nickel loading on the NC/5%Ni samples.

2.7. Discussion

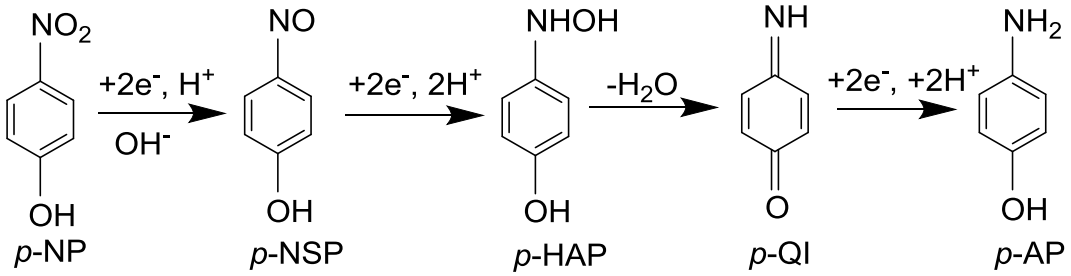

Scheme **2.1**. Proposed mechanism of reduction of *p*-NP to *p*-AP.

The reduction of *p*-NP by $NaBH_4$ is a six electron, six proton transfer reaction accompanied by loss of two water molecules. The mechanism generally accepted within the catalysis community[38] is that first proposed by Haber[39] in which reduction is believed to occur via *p*-NSP and *p*-HAP intermediates in both protic and aprotic media. In the electrochemical community dehydration of the *p*-HAP is believed to give *p*-QI, which is then reduced to *p*-AP. This mechanism, is shown in Scheme **2.1**.[40] The reaction of *p*-HAP is believed to generally be the slow step.[38] This mechanism has recently been called into question[41] based on isotope effects, and differences in the observed chemistry when the reaction was started with *p*-NSP, but it has been argued that there are considerable variations in which of a number of potential pathways are followed depending upon metal, support, solvent and H_2 pressure.[42] The first two steps, reduction of *p*-NP to *p*-NSP and reduction of *p*-NSP to *p*-HAP are fast[38] consistent with the *p*-NSP (m/z 123) not being detected in the GC-MS spectrum. Similarly the signal for m/z 125

corresponding to *p*-HAP was not detected. That *p*-QI is observed and *p*-HAP was not suggests that *p*-QI must be a reasonably stable intermediate in solution, suggesting that it is reduction of *p*-QI that is the rate determining step. However, it is possible that dehydration/reduction of *p*-HAP is the rate determining step, but that *p*-HAP is strongly adsorbed on the surface, while *p*-QI is not, so that the observation of one rather than the other could reflect differences in adsorption rather than rate.

In considering the catalytic activity: NC/5%Ni (1.25×10^{-2} $s^{-1} \pm 3 \times 10^{-3}$) is only slightly higher than that of NC/1%Ni (1.0×10^{-2} $s^{-1} \pm 4 \times 10^{-3}$). We can neglect the solution phase hydrogenation, which is known to be much less than the heterogeneous catalytic rate. We have not corrected for any adsorption on the Ni, but can reasonably expect this (and the catalysis) to be proportional to the Ni surface area. With higher Ni loading an increase in Ni surface area and hence in catalytic activity would be expected, with a 2.7-fold increase expected if similarly sized NPs are produced in both cases. However, the observed particle sizes seen by TEM were significantly larger for NC/5%Ni (47 nm) than for the NC/1%Ni (9 nm average). Based on these average values, the estimated surface Ni surface areas/gram catalyst are about 0.46 m^2 for NC/1%Ni and 0.32 m^2 for NC/5%Ni. The lower surface area for the NC/5%Ni is because there are fewer, larger particles for the NC/5%Ni despite the increase in total amount of Ni. This approximate calculation would therefore predict that the two catalysts would have similar activities: exactly what is observed.

The observed increase in particle size, accompanied by the inferred decrease in the number of particles, does raise the question of how the number of particles can decrease, when the amount of Ni is increased. The $Ni(NO_3)_2$ added serves as more than just a precursor to Ni NPs, it also catalyzes the polymerization of FA. Previous procedures to nanocast carbon with FA

included addition of a small amount of OA[15] to induce polymerization and minimize FA evaporation. This role of the Ni would suggest that it is initially dispersed within the mesopores of the SiO_2 monolith with the carbon precursor. It is possible that the Ni nitrate phase separates from the carbon precursor solution during the drying step. However this seems unlikely: the Ni actually adsorbs somewhat on the SiO_2 (which leads to the somewhat inhomogeneous distribution of Ni within the monolith that we have observed), this adsorption would act to keep the Ni spread out over the surface of the SiO_2, rather than concentrated. Further, the TEM shows clearly that the Ni NPs are incorporated within the carbon in the mesopores, arguing against large scale phase separation.

This implies that the particle growth must be occurring at a later stage of the formation of the nanocomposites. It seems reasonable to take as a starting point that the mechanism for Ni nanoparticle formation in the carbon precursor is similar to that seen in mesoporous SiO_2: decomposition of the $Ni(NO_3)_2.6H_2O$ first to the Ni oxide and that the Ni oxide is then reduced by the carbon present to Ni metal. The mobility of $Ni(NO_3)_2.6H_2O$ on heating is strongly dependent upon the conditions under which it is carried out. We have previously shown the impact of heating under air, vacuum or various inert gases on the decomposition of $Co(NO_3)_2$ in mesoporous SiO_2 templates.[43] Similarly, it has been shown that the presence of NO significantly reduces the mobility of Co and Ni nitrates in mesoporous SiO_2 by scavenging oxygen radicals, aiding the conversion of the mobile nitrate hydrate phases into the immobile hydroxynitrate counterparts.[44] The furan ring is known to be an active radical trap[45] and so it seems likely that FA will similarly act as an oxygen scavenger. In our earlier work on nickel oxide we saw good evidence for mobility of nickel oxide in mesoporous SiO_2 at temperatures of 550-600 ^oC.[43] However it is reported[46] that $Ni(NO_3)_2$ incorporated into cellulose is converted to nickel oxide at

300 ^{o}C and to Ni metal by 400 ^{o}C. This would suggest that nickel oxide mobility is unlikely to be the primary cause of the growth of nickel oxide particles. We believe that the particle growth is predominantly at the point where the nickel oxide has been reduced to Ni.

Metal NPs are known to impact the graphitization of carbon,[47,48] in particular nanoparticles of Fe, Co, Cr and Ni are reported to be able to catalyze the graphitization of carbon to graphite at temperatures below 1000 ^{o}C.[49] The mechanism is believed to be either formation of metal carbides or dissolution of amorphous carbon in the nanoparticle followed by precipitation of graphitic material.[48] The Ni NPs initially produce a shell of graphitic carbon around them, but with time and rising temperature this shell breaks[50] allowing the particle to move leaving a trail of graphitic carbon.[46] As the particles move through the carbon they grow.[46] This can be clearly seen in this work by the increase in particle size for the NC/5%Ni compared to the NC/1%Ni and the observation of agglomerated NPs in the TEM. This suggested mechanism is in agreement with the increase in the graphitic nature of the material seen in both the XRD and the Raman results. It also is consistent with the decrease in microporosity that is observed between pure carbon, and carbon incorporating Ni NPs: graphitization would be predicted to lead to decreased microporosity. Carbon atoms on the surface of a micropore have higher energy due to being on a surface and so would be more easily dissolved into the Ni nanoparticle, leading to a preferential removal of micropores possibly accompanied by a growth of mesopores.

2.8 Conclusions

Hierarchically porous NC/Ni carbon monolithic composites were synthesized using a one pot synthesis by nanocasting into hierarchically porous SiO_2 monoliths. After removal of the SiO_2 template Ni NPs were found to be distributed over the resulting carbon monoliths, with small NPs incorporated into the mesopores and larger NPs distributed on the macropore walls.

The Ni NPs have also increased the extent of graphitization of the carbon. The Ni supported on carbon monoliths was found to be active for reduction of 4-NP to 4-AP by $NaBH_4$. The material synthesized with higher Ni loading was found to be more catalytically active, however the catalytic activity on a per gram Ni basis was lower due to increased agglomeration of Ni leading to fewer, larger NPs. Analysis of the reaction products by GC-MS showed the formation of the intermediate *p*-QI, an intermediate routinely postulated in the electrochemical literature but not previously observed or postulated in the catalysis literature.

2.9 References

(1) Saha, S.; Pal, A.; Kundu, S.; Basu, S.; Pal, T.: Photochemical Green Synthesis of Calcium-Alginate-Stabilized Ag and Au Nanoparticles and Their Catalytic Application to 4-Nitrophenol Reduction. *Langmuir* **2010,** *26*, 2885–2893.

(2) Bhowmik, T.; Kundu, M. K.; Barman, S.: Ultra small gold nanoparticles–graphitic carbon nitride composite: an efficient catalyst for ultrafast reduction of 4-nitrophenol and removal of organic dyes from water. *RSC. Adv.* **2015,** *5*, 38760-38773.

(3) Li, M.; Chen, G.: Revisiting catalytic model reaction p-nitrophenol/ $NaBH_4$ using metallic nanoparticles coated on polymeric spheres. *Nanoscale* **2013,** *5*, 11919-11927.

(4) Zhang, S.; Gai, S.; He, F.; Ding, S.; Lia, L.; Yang, P.: In situ assembly of well-dispersed Ni nanoparticles on silica nanotubes and excellent catalytic activity in 4-nitrophenol reduction. *Nanoscale* **2014,** *6*, 11181-11188.

(5) Yoon, B.; Hakkinen, H.; Landman, U.; Worz, A. S.; Antonietti, J.-M.; Abbet, S.; Judai, K.; Heiz, U.: Charging Effects on Bonding and Catalyzed Oxidation of CO on Au_8 Clusters on MgO. *Science* **2005,** *307*, 403-407.

(6) Mostafa, S.; Croy, J. R.; Heinrich, H.; Cuenya, B. R.: Catalytic decomposition of alcohols over size-selected Pt nanoparticles supported on ZrO_2: A study of activity, selectivity, and stability. *App. Catal. A* **2009,** *366*, 353-362.

(7) Sanchez, S. I.; Menard, L. D.; Bram, A.; Kang, J. H.; Small, M. W.; Nuzzo, R. G.; Frenkel, A. I.: The Emergence of Nonbulk Properties in Supported Metal Clusters: Negative Thermal Expansion and Atomic Disorder in Pt Nanoclusters Supported on γ-Al_2O_3. *J. Am. Chem. Soc.* **2009,** *131*, 7040-7054.

(8) Yang, Y.; Chiang, K.; Burke, N.: Porous carbon-supported catalysts for energy and environmental applications: A short review. *Catal. Today* **2011,** *178*, 197-205.

(9) He, X.; Male, K. B.; Nesterenko, P. N.; Brabazon, D.; Paull, B.; Luong, J. H. T.: Adsorption and Desorption of Methylene Blue on Porous Carbon Monoliths and Nanocrystalline Cellulose. *ACS Appl. Mater. Interfaces* **2013,** *5*, 8796-8804.

(10) Xia, Y.; Yang, Z.; Zhu, Y.: Porous carbon-based materials for hydrogen storage: advancement and challenges. *J. Mater. Chem. A* **2013,** *1*, 9365-9381.

(11) Dutta, S.; Bhaumik, A.; Wu, K. C. W.: Hierarchically porous carbon derived from polymers and biomass: effect of interconnected pores on energy applications. *Energy Environ. Sci.* **2014,** *7*, 3574-3592.

(12) Jun, S.; Joo, S. H.; Ryoo, R.; Kruk, M.; Jaroniec, M.; Liu, Z.; Ohsuna, T.; Terasaki, O.: Synthesis of New, Nanoporous Carbon with Hexagonally Ordered Mesostructure. *J. Am. Chem. Soc.* **2000,** *122*, 10712-10713.

(13) Joo, S. H.; Choi, S. J.; Oh, I.; Kwak, J.; Liu, Z.; Terasaki, O.; Ryoo, R.: Ordered nanoporous arrays of carbon supporting high dispersions of platinum nanoparticles. *Nature* **2001,** *412*, 169-172.

(14) Taguchi, A.; Smått, J.-H.; Lindén, M.: Carbon Monoliths Possessing a Hierarchical, Fully Interconnected Porosity. *Adv. Mater.* **2003,** *15*, 1209-1211.

(15) Lu, A.-H.; Smått, J.-H.; Backlund, S.; Lindén, M.: Easy and flexible preparation of nanocasted carbon monoliths exhibiting a multimodal hierarchical porosity. *Micropor. Mesopor. Mater.* **2004,** *72*, 59-65.

(16) Lu, A.-H.; Smått, J.-H.; Lindén, M.: Combined Surface and Volume Templating of Highly Porous Nanocast Carbon Monoliths. *Adv. Funct. Mater.* **2005,** *15*, 865-871.

(17) Li, Z.; Liu, J.; Huang, Z.; Yang, Y.; Xia, C.; Li, F.: One-Pot Synthesis of Pd Nanoparticle Catalysts Supported on N‑Doped Carbon and Application in the Domino Carbonylation. *ACS Catal.* **2013,** *3*, 839−845.

(18) Kong, A.; Kong, Y.; Zhu, X.; Han, Z.; Shan, Y.: Ordered mesoporous Fe (or Co)-N-graphitic carbons as excellent non-precious-metal electrocatalysts for oxygen reduction. *Carbon* **2014,** *78*, 49-59.

(19) Yang, Y.; Ren, Y.; Sun, C.; Hao, S.: Facile route fabrication of nickel based mesoporous carbons with high catalytic performance towards 4-nitrophenol reduction. *Green Chem.* **2014,** *16*, 2273-2280.

(20) Wang, W.; Wang, H.-Y.; Wei, W.; Xiao, Z.-G.; Wan, Y.: Self-Assembling and Size-Selective Synthesis of Ni and NiO Nanoparticles Embedded in Ordered Mesoporous Carbon and Polymer Frameworks. *Chem. Euro. J.* **2011,** *17*, 13461-13472.

(21) Yao, J.; Li, L.; Song, H.; Liu, C.; Chen, X.: Synthesis of magnetically separable ordered mesoporous carbons from F127/$[Ni(H_2O)_6](NO_3)_2$/resorcinol-formaldehyde composites. *Carbon* **2009,** *47*, 436–444.

(22) Kotbagi, T. V.; Hakat, Y.; Bakker, M. G.: Facile One-Pot Synthesis and Characterization of Nickel Supported on Hierarchically Porous Carbon. *Mater. Res. Bull.* **2016,** *73*, 204-210.

(23) Liu, Y.; Li, D.; Lin, B.; Sun, Y.; Zhang, X.; Yang, H.: Hydrothermal synthesis of Ni-doped hierarchically porous carbon monoliths for hydrogen storage. *J. Porous Mat.* **2015,** *22*, 1417–1422.

(24) El-Sheikh, S. M.; Ismail, A. A.; Al-Sharab, J. F.: Catalytic reduction of p-nitrophenol over precious metals/highly ordered mesoporous silica. *New J. Chem.* **2013,** *37*, 2399-2407.

(25) Sun, J.; Fu, Y.; He, G.; Sun, X.; Wang, X.: Catalytic hydrogenation of nitrophenols and nitrotoluenes over a palladium/graphene nanocomposite. *Catal. Sci. Technol.* **2014,** *4*, 1742-1748.

(26) Ji, T.; Chen, L.; Schmitz, M.; Bao, F. S.; Zhu, J.: Hierarchical macrotube/mesopore carbon decorated with mono-dispersed Ag nanoparticles as a highly active catalyst. *Green Chem.* **2015,** *17*, 2515-2523.

(27) Niu, Z.; Zhang, S.; Sun, Y.; Gai, S.; He, F.; Dai, Y.; Li, L.; Yang, P.: Controllable synthesis of Ni/SiO_2 hollow spheres and their excellent catalytic performance in 4-nitrophenol reduction. *Dalton Trans.* **2014,** *43* , 16911-16918.

(28) Smått, J.-H.; Schunk, S. A.; Lindén, M.: Versatile Double-Templating Synthesis Route to Silica Monoliths Exhibiting a Multimodal Hierarchical Porosity. *Chem. Mater.* **2003,** *15*, 2354-2361.

(29) Brunauer, S.; Emmett, P. H.; Teller, E.: Adsorption of Gases in Multimolecular Layers. *J. Am. Chem. Soc.* **1938,** *60*, 309-319.

(30) Barrett, E. P.; Joyner, L. G.; Halenda, P. P.: The Determination of Pore Volume and Area Distributions in Porous Substances. I. Computations from Nitrogen Isotherms. *J. Am. Chem. Soc.* **1951,** *73*, 373-380.

(31) Backlund, S.; Smatt, J.-H.; Rosenholm, J. B.; Linden, M.: Template-Free Sol-Gel Synthesis of Hierarchically Macro- and Mesoporous Monolithic TiO_2. *J. Disper. Sci. Tech.* **2007,** *28*, 115-119.

(32) Grano, A. J.; Sayler, F. M.; Smått, J.-H.; Bakker, M. G.: Hierarchically Porous Monoliths of carbon and metal oxides with ordered mesopores *J. Porous Mat.* **2014,** *21*, 1113-1122.

(33) Witek, G.; Noeske, M.; Mestl, G.; Shaikhutdinov, S.; Behm, R. J.: Interaction of platinum colloids with single crystalline oxide and graphite substrates: a combined AFM, STM and XPS study. *Catal. Lett.* **1996,** *37*, 35-39.

(34) Briggs, D.; Beamson, G.: Primary and secondary oxygen-induced C1s binding energy shifts in x-ray photoelectron spectroscopy of polymers. *Anal. Chem.* **1992,** *64*, 1729-1736.

(35) B.P. Payne; M.C. Biesinger; McIntyre, N. S.: The study of polycrystalline nickel metal oxidation by water vapour. *J. Electron Spectrosc.* **2009,** *175*, 55-65.

(36) Cancado, L. G.; Jorio, A.; Martins Ferreira, E. H.; Stavale, F.; Achete, C. A.; Capaz, R. B.; Moutinho, M. V. O.; Lombardo, A.; Kulmala, T. S.; Ferrari, A. C.: Quantifying Defects in Graphene via Raman Spectroscopy at Different Excitation Energies. *Nano Lett.* **2011,** *11*, 3190–3196.

(37) Liu, J.; Qin, G.; Raveendran, P.; Ikushima, Y.: Facile "Green" Synthesis, Characterization, and Catalytic Function of β-D-Glucose-Stabilized Au Nanocrystals. *Chem. Euro. J.* **2006,** *12*, 2131-2138.

(38) Blaser, H.-U., A Golden Boost to an Old Reaction. *Science* **2006,** *313*, 312-313.

(39) Haber, F., Uber Stufenweise Reduktion Des Nitrobenols Mit Begreztem Kathodenpotential. *Z. Elektrochem.* **1898,** *4*, 506-514.

(40) Boateng, A.; Brajter-Toth, A.: Nanomolar detection of p-nitrophenol via in situ generation of p-aminophenol at nanostructured microelectrodes. *Analyst* **2012,** *137*, 4531-4538.

(41) Gelder, E. A.; Jackson, S. D.; Lok, C. M.: The hydrogenation of nitrobenzene to aniline: a new mechanism. *Chem. Comm.* **2005**, 522-524.

(42) Blaser, H.-U.; Steiner, H.; Studer, M.: Selective Catalytic Hydrogenation of Functionalized Nitroarenes: An Update. *ChemCatChem* **2009,** *1*, 210-221.

(43) Smått, J.-H.; Sayler, F. M.; Grano, A.; Bakker, M. G.: Formation of Hierarchically Porous Metal Oxide and Metal Monoliths by Nanocasting into Silica Monoliths. *Adv. Eng. Mat.* **2012,** *14*, 1059-1073.

(44) Wolters, M.; Munnik, P.; Bitter, J. H.; de Jongh, P. E.; de Jong, K. P.: How NO Affects Nickel and Cobalt Nitrates at Low Temperatures To Arrive at Highly Dispersed Silica-Supported Nickel and Cobalt Catalysts. *J. Phys. Chem. C* **2011,** *115*, 3332-3339.

(45) Davidenko, N.; Zaldivar, D.; Peniche, C.; Sastre, R.; San Roman, J.: Activity of the Furfuryl Ring in the Free Radical Polymerization of Acrylic Monomers. *J. Polym. Sci., Part A: Polym. Chem.* **1996,** *34*, 2759-2766.

(46) Sevilla, M.; Fuertes, A. B.: Graphitic carbon nanostructures from cellulose. *Chem. Phys. Lett.* **2010,** *490*, 63-68.

(47) Oya, A.; Otani, S.: Influences of Particle Size of Metal on Catalytic Graphitization of Non-graphitizing Carbons. *Carbon* **1981,** *19*, 391-400.

(48) Oya, A.; Marsh, H.: Phenomena of catalytic graphitization. *J. Mater. Sci.* **1982,** *17*, 309-322.

(49) Maldonado-Hodar, F. J.; Moreno-Castilla, C.; Rivera-Utrilla, J.; Hanzawa, Y.; Yamada, Y.: Catalytic Graphitization of Carbon Aerogels by Transition Metals. *Langmuir* **2000,** *16*, 4367-4373.

(50) Hoekstra, J.; Beale, A. M.; Soulimani, F.; Versluijs-Helder, M.; Geus, J. W.; Jenneskens, L. W.: A Combined Raman Spectroscopy, Temperature Dependent X-ray Diffraction and High-Resolution Transmission Electron Microscopy Study. *J. Phys. Chem. C* **2015,** *119*, 10653−10661.

Appendix A

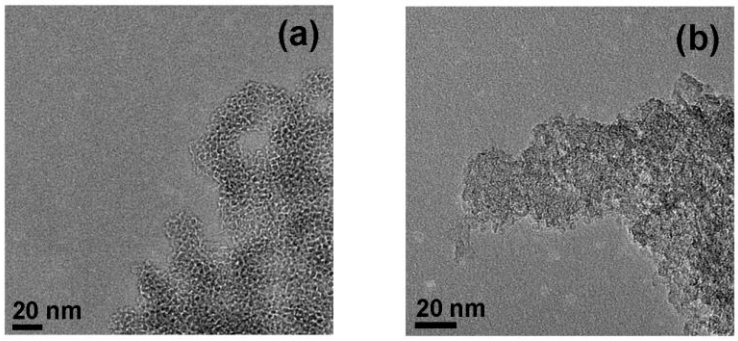

Figure (A1). TEM images of (a) SiO_2 (b) NC.

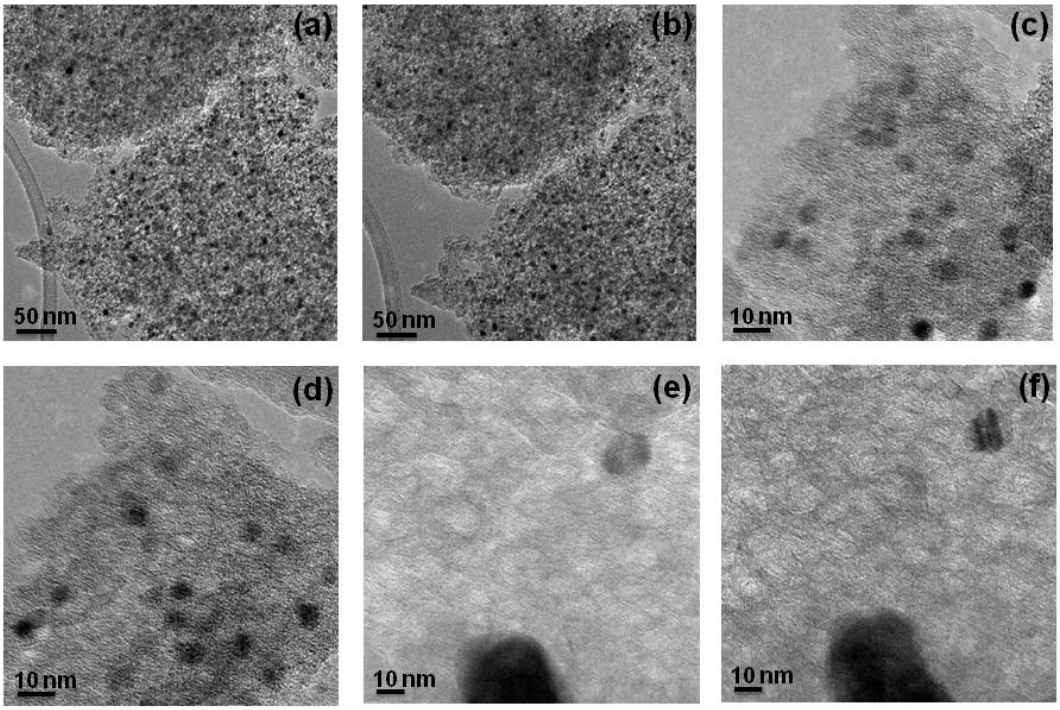

Figure (A2). TEM images of NC/1Ni, tilt (a) +15° (b) -15°, HRTEM images of NC/1Ni (c) +15° (d) -15°, NC/5Ni (e) +15° (f) -15°.

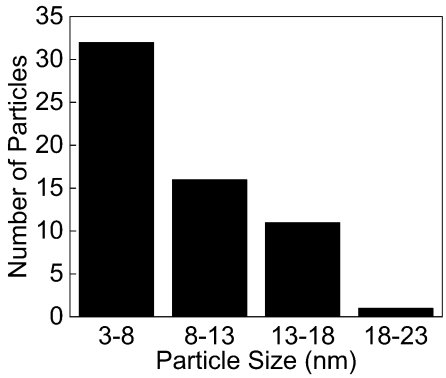

Figure (A3). Nickel Particle Size Distribution for NC/1%Ni.

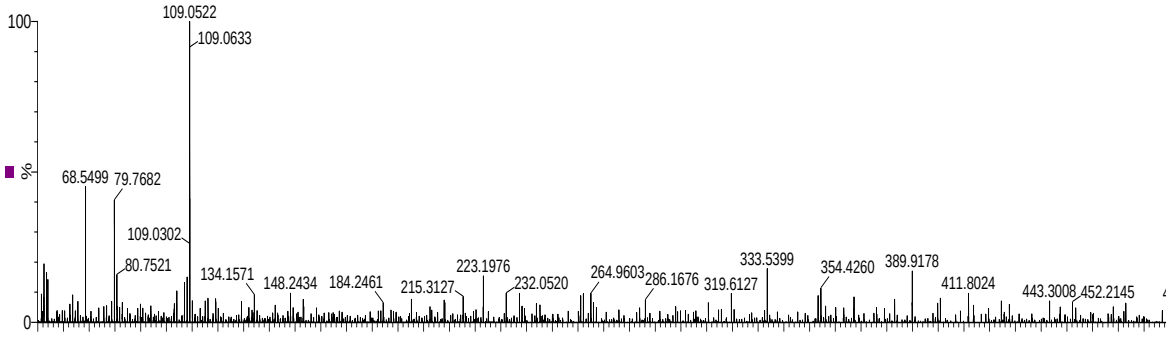

(a)

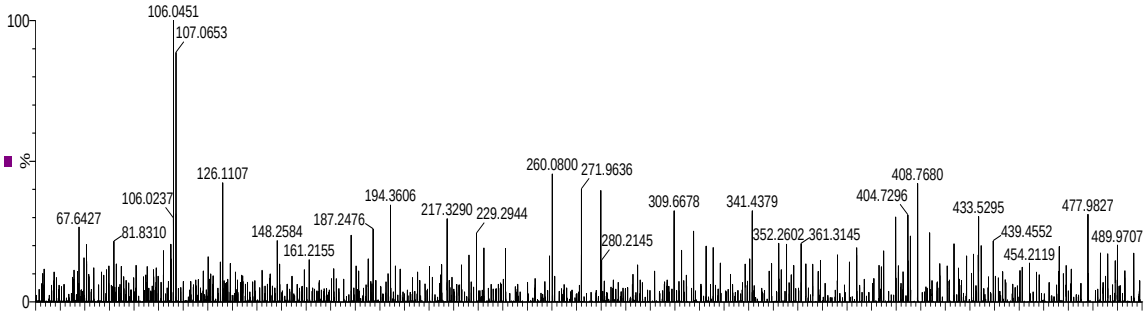

(b)

Figure (A4). GC-MS spectra of (a) *p*-AP (b) *p*-QI.

CHAPTER 3

Catalytic Graphitization of Monolithic Nanocast Carbon by Iron, Cobalt and Nickel Nanoparticles

3.1 Abstract

Hierarchically porous carbon monoliths containing metal NPs were synthesized in a one pot synthesis through the nanocasting technique using SiO_2 as the template. Metal (Fe, Co, and Ni) nitrate dissolved in FA was used, in which FA is the carbon precursor. The polymerized monoliths were pyrolyzed in the temperature range of 500 °C-800 °C. The macropore structure of SiO_2 has been replicated in nanocast carbon and N_2 adsorption analysis revealed that the monolithic composites have high surface area, high mesopore volume, and micropores are also present. The temperature effect on catalytic graphitization was studied by using XRD, TEM and Raman spectroscopy. Analysis of the Raman data with increasing pyrolysis temperature, with and without metal, confirmed ordering of amorphous carbon. Iron, cobalt, and nickel were found to be good catalysts of graphitization with the order of catalytic activity being Fe> Co> Ni. It was observed that iron was capable of producing turbostratic carbon at a low temperature of 500 °C, while turbostratic carbon was produced at temperatures of 700 °C when cobalt and nickel were present. TEM images showed that turbostratic carbon domains were located close to the metal NPs consistent with catalytic graphitization.

3.2 Introduction

Graphite consists of sp^2 hybridized carbon atoms arranged in sheets that have an AB stacking structure.[1,2] The unit cell contains two atoms, A and B, and stacking graphene layers in a Bernal arrangement produces multilayer graphene or three dimension graphite.[2] Graphitic carbon is important in applications like electrode materials,[3] thermal conductive materials,[4] and conducting plates.[5] Graphite has been prepared by many methods that require often extreme conditions like high temperatures or special and expensive equipment. These synthesis methods include CVD,[6] solvothermal synthesis,[7] and arc discharge.[8] Catalytic graphitization is a process in which a catalyst is used to enhance the crystallization of carbon by a chemical reaction between the catalyst (metal or an inorganic compound) and ungraphitized carbon.[9] Different from the other methods cited above, this method requires only moderate conditions and low temperatures.[10] Transition metals like Fe,[11-13] Co,[11,13,14] Ni,[11,13,14] Mn,[11] Cr[11,13] and metal oxides like Cr_2O_3[15] and MnO[15] have been extensively studied as catalysts. In addition metals like Mg,[11,14] Ca[11,14] and Si and Ge have been used as catalysts as well.[11] A wide variety of carbon precursors have been investigated including phenolic resins,[16] polyfurfuryl alcohol[12] and cellulose,[17] in which the metal salt is mixed with the carbon precursor. It has been found that when the metal is incorporated in the carbon structure as in iron and cobalt gluconates[18] and nickel phthalocyanines,[19] the carbon structure resulting from the catalysis is of good quality.
A major application of graphitic carbon is to use in the electrochemical field as electrodes and conducting materials.[3,5] The surface area, presence of micropores (average pore diameter less than 2 nm) and mesopores (average pore diameter 2-50 nm), composing the electrode material are important parameters that can, for example, affect the performance of capacitors when these capacitors are utilizing graphitic carbon as electrodes.[20] Graphitized carbon of high surface area

and pore volume is believed to facilitate electron transport when they are used as conducting materials.[21] Namely, a high surface area facilitates the accumulation of charges in the electrode electrolyte interface, while micropores are essential in forming the electrical double layer. Note that as these micropores need to be electrochemically accessible to ions, coupling to mesopores allows improved ion transport to the bulk of the electrode material.[20] Gao and *et al.* report that ease of graphitization of mesoporous carbon could be increased by selecting appropriate carbon precursors (such as polyaromatic hydrocarbons), CVD, applying high temperature, and catalytic graphitization.[21] Mesoporous carbon that has some graphitic order have also been synthesized by using SiO_2 as the template without any catalyst for the graphitization[22-24], while catalytically graphitized mesoporous carbon has been prepared by using SiO_2 as the template.[16,21]

In this paper, a new method of preparing hierarchically porous carbon monoliths of high surface area with graphitic ordering through catalytic graphitization is reported. FA has been used as the carbon precursor and iron, cobalt and nickel nitrates have been used as the metal salts. After the polymerization of FA, monoliths were pyrolyzed in N_2 flow in the temperature range of 500 °C - 800 °C. The scope of this work is to study the effect of temperature on catalytic graphitization of nanocast carbon by XRD, TEM and Raman spectroscopy.

3.3 Experimental

3.3.1 Materials

PEG 35,000, HNO_3 70%, KOH, ethanol 95% and acetone were procured from VWR. NH_4OH 29%, was purchased from Fisher Scientific. FA 98% was purchased from Acros Organics. TEOS 98%, anhydrous OA 98%, $Ni(NO_3)_2.\ 6H_2O$ 98%, $Fe(NO_3)_3.\ 9H_2O$ 98+% and $Co(NO_3)_2.\ 6H_2O$ 97.7%, were purchased from Alfa Aesar. C_{18}TAB was obtained from Genescript. All chemicals were used as received without further purification.

3.3.2 Material Synthesis

3.3.2.1 Synthesis of SiO_2 monoliths

Synthesis of SiO_2 monoliths was carried out according to a literature procedure.[25] PEG 35,000 (2.2 g) was added to 33 mL of 18 MΩ water and was stirred until it dissolved. Then 6.5 mL of 30% HNO_3 was added to the stirring mixture. After that, 32 mL of TEOS was added and was stirred until a homogeneous mixture was obtained. Then 5.5 g of C_{18}TAB was added and stirring was continued until all the surfactant dissolved. The solution was poured into well plates and was incubated at 40 °C for 72 h. The gels were removed from the well plates and were immersed in 1 M NH_4OH at 90 °C for 12 h. Then the monoliths were washed with 0.1 M HNO_3 and then washed with deionized water several times. The monoliths were finally washed with acetone and were dried at 40°C for 72 h. Then they were calcined at 550 °C for 5 h at a heating rate of 1 °C•min^{-1}.

3.3.2.2 Synthesis of NC monoliths

Synthesis of nanocast carbon was performed according to a modified version of a published procedure.[26,27] The SiO_2 monoliths which were used as templates were degassed for several hours prior to use. FA and ethanol were mixed in the volume ratio of 5:1 and sufficient OA was dissolved in the mixture such that the FA:OA molar ratio was 200:1. The SiO_2 monoliths were added to the mixture and were allowed to infiltrate overnight. The monoliths were then heated to 80 °C and kept at that temperature for 24 h to polymerize the FA and they were then heated to the required final temperature (500 °C, 600 °C, 700 °C and 800 °C) in 4 h and held at that temperature for 2 h. The resulting SiO_2/NC monoliths were etched in 3 M KOH

at 75 °C for 24 h to remove the SiO_2. Then they were washed with deionized water several times and were dried at room temperature.

3.3.2.3 Synthesis of metal nanoparticles containing nanocast carbon monoliths

Metal containing nanocast carbon monoliths were prepared using SiO_2 as the template. SiO_2 monoliths were degassed for several hours prior to use. FA and ethanol were mixed in the volume ratio of 5:1 and metal (Ni, Co, and Fe) was included as 1 wt% relative to FA by dissolving the metal nitrate ($Fe(NO_3)_3.\ 9H_2O$, $Co(NO_3)_2.\ 6H_2O$, and $Ni(NO_3)_2.\ 6H_2O$) in the mixture of FA and ethanol. The SiO_2 monoliths were added to the mixture and were allowed to infiltrate overnight. Then they were heated to 80 °C and held at 80 ^oC for 15 h to polymerize the FA. The carbonization, etching and drying were carried out similarly to the procedure described above.

3.4 Characterization

XRD patterns were collected on a Bruker D8 Discover instrument with GADDS (Co anode, wavelength 1.79 Å) and a High Star area detector. The interlayer spacing, d(002) was calculated from the Bragg equation, $d(002) = \lambda/2\sin\theta$, in which λ is the wavelength of the Co Kα x-ray source, θ is the Bragg angle and d is the interlayer spacing. Crystallite size (L_C) was calculated by the Debye-Scherrer equation, $L_C = K\lambda/B\cos\theta$, in which L_C is the crystallite size, K is the shape factor (0.9), and B is the FWHM in radians. The acquisition time for all samples was 1 hour. TEM images were obtained on a FET Tecnai F20, equipped with a cold field emission gun and a super twin objective lens with an accelerating voltage of 200 kV. Samples were

prepared on holey carbon supported by a Cu grid. The morphology was imaged by bright field image and SAED was used for structural analysis.

Raman spectra were acquired by using a 10× objective lens and 532 nm and 633 nm laser wavelengths as excitation sources. The laser power at the sample was kept around 0.5 mW to avoid heating effects. The spectra were deconvoluted with Lorentizian curves by using the Peakfit software. A base line subtraction was performed before fitting the data. The region with frequencies ranging from 1200 to 1800 cm^{-1} (so-called G- and D-bands) was fitted with three peaks. The region with frequencies ranging from 2300 to 2900 cm^{-1} was fitted to four peaks.

XPS spectra were acquired on a Kratos Axis 165 XPS system that was operated with a dual Mg/Al anode and a monochromatic x-ray source at 1486.6 eV, corresponding to the Al Kα line. Photoelectrons were collected with a takeoff angle of 90° relative to the sample surface. The survey and high resolution spectra were acquired in order to determine the chemical states of C, O, Fe, Co and Ni. The survey spectra were taken at a pass energy of 160 eV, with a step size of 0.1 eV, using a single scan. The dwell time was 500 ms for the survey spectra and 1000 ms for the high res spectra.

SEM images were collected using a JEOL 7000 FE-SEM operated at 30 kV, with diode based back scatter detector and an Oxford EDS detector for elemental analysis. N_2 adsorption measurements were taken on a quantachrome Nova 2200e pore size analyzer at -197 °C with He mode to determine the surface area and void volumes of the monoliths. The interpretation of the isotherms was carried out with Quantachrome Nova Win software version 11.03 using a multipoint BET method[28] to determine the surface areas, and the BJH method[29] was applied to the adsorption branch to determine the pore size distribution. The volume of micropores was determined by the t-plot method.

3.5 Results and Discussion

3.5.1 XRD of NC

XRD is a technique widely used for the analysis of graphitization of carbon. XRD patterns of NC pyrolyzed at different temperatures (500 °C, 600 °C, 700 °C and 800 °C) are shown in Figure **3.1**. The XRD patterns of NC from all pyrolysis temperatures look similar and do not show the crystallite carbon peak, revealing that well ordered graphitic carbon is not present. The broad peak centered around 28°, which corresponds to an interlayer spacing of about 0.36 nm, indicates that NC is amorphous and crystalline graphitic carbon is not present. The other, less intense peak, which appears around 52°, comes from the merging of two dimensional (10) and three dimensional (100) peaks. XRD patterns are basically characterized by two reflections. They are the (002) reflection, the three dimensional diffraction corresponding to the stacking of graphene layers and two dimensional diffraction lines such as (10) and (11).[1] The latter lines are superimposing on the corresponding three-dimensional diffraction lines such as (10) on (100) and (11) on (110). So it is almost impossible to distinguish the two dimensional lines[1] and analysis could not performed on those peaks. If that analysis could be done especially of the (10) diffraction peak, intensity should increase, FWHM should decrease and the peak position should shift to a lower diffraction angle with increasing pyrolysis temperature.[30] The XRD observations are consistent with the TEM images (*vide infra*).

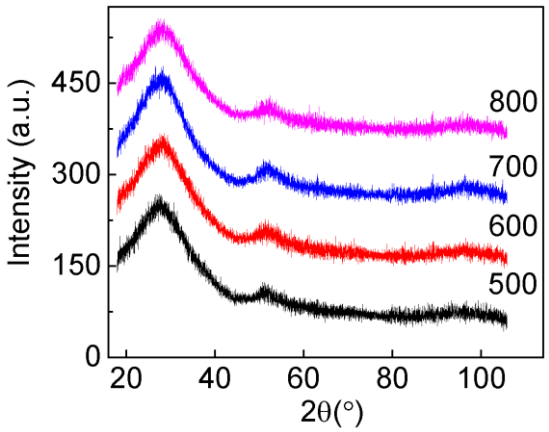

Figure (3.1). XRD pattern on NC pyrolyzed at 500 °C, 600 °C, 700 °C, and 800 °C.

3.5.2 TEM of NC

The TEM image of NC treated at 800 °C (Figure **3.2a**), clearly shows the amorphous, disordered mesoporous nature of the carbon. The HRTEM image (Figure **3.2b**) does not show any graphitic domains but nanocrystallites could be seen.

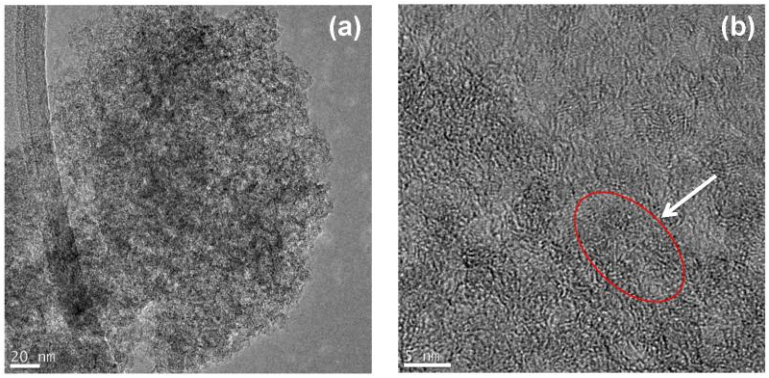

Figure (3.2). (a) TEM image (b) HRTEM image of NC 800 °C. Nanocrystallites are shown by the highlighted circle in the HRTEM image.

3.5.3 XRD of NC/Fe

The XRD patterns of NC/Fe are given in Figure **3.3a**. The graphitic (002) peak is present at temperatures from 500 to 800 °C. That the peak is not present in NC and that the intensity

grows with increasing temperature is consistent with catalytic graphitization of amorphous carbon by Fe nanoparticles. The XRD patterns show that Fe is capable of catalyzing graphitization of carbon at relatively low temperatures. The crystallite peak was observed around 30° which corresponds to an interlayer spacing of about 0.345 nm. This result suggests that some turbostratic carbon is present, as the interlayer spacing for crystalline graphite is 0.335 nm. A d spacing higher than 0.342 nm is generally considered to be due turbostratic carbon.[31] The crystallite size determined from the width of the C(002) peak is about 3.4 nm. At 500 °C, although the graphitic carbon peak is present in the XRD patterns, the broad peak that appeared around 28° indicates that amorphous carbon is still the dominant form. This broad feature seems to be less dominant as the pyrolysis temperature increases, consistent with increasing conversion of amorphous to more crystalline carbon. The broad small peak at 51° corresponds to the (10) and (100) diffractions, as discussed earlier in the text, and is also present in NC/Fe pyrolyzed at all temperatures. In turbostratic carbon, the peak for two dimensional diffraction (10), is expected to increase in intensity, have narrower width and decreasing peak position with increasing temperature.[30] However, the (111) diffraction of the Fe nanoparticles also appears at 51° and the interference from this peak prevents a more detailed analysis of the (10) and (100) carbon peaks. Hexagonal graphite and turbostratic graphite possess regular spacing in stacked graphene layers but they differ in degree of stacking ordering.[1] Hexagonal graphite has the ordered AB stacking structure and the turbostratic carbon has graphene layers that are randomly translated relative to each other and are also rotated about the normal to the graphene layers. These translations and rotations of stable h-graphite change the interlayer spacing and/or shape of atomic layers.[1] Turbostratic carbon has structural changes like rotation, translation, curvature, local fluctuation of interlayer spacing of graphene layers. These changes affect the diffraction

angle and the FWHM of the XRD peaks and hence they cannot be simply used to characterize the lattice parameters and crystallite size of turbostratic carbon.[1] Parameters such as peak position, FWHM and lattice parameters calculated using the above expressions can give some general indication about the sample structure. The nanoparticle distributions in the monolithic composites are not spatially homogeneous as reported in our previous study.[32] So the graphitization catalysts are not evenly distributed through the monolith, which results in more heterogeneous carbon containing both turbostratic and amorphous carbons. So the differences in the peak position, interlayer spacing and crystallite size are likely due to the structural changes of turbostratic carbon and heterogeneous distribution of the metal nanoparticles.

In the XRD diffraction pattern, peaks for metallic iron or iron oxide could not be seen. This is due to the metal nanoparticles being dissolved/washed out during the etching of SiO_2 and subsequent, extensive washing of the monoliths. In order to determine the crystal state XRD patterns of the monoliths before etching (Figure **3.3b**) were collected. The XRD patterns of monoliths pyrolyzed at 600°C, 700 °C and 800 °C, indicate the presence of iron nanoparticles and the iron (111), (200) and (220) diffraction peaks were measured at 51°, 59.60° and 89°. The Fe (111) diffraction peak is believed to overlap the graphitic carbon (10) and (100) diffraction peaks and could not be resolved. In the XRD pattern of the monoliths pyrolyzed at 500°C, these peaks were not present which could be due to the nanoparticle dispersion. Peaks corresponding to iron carbide were not observed. The broad peak in all patterns in Figure **3.3b** has the contribution of both amorphous carbon and SiO_2.

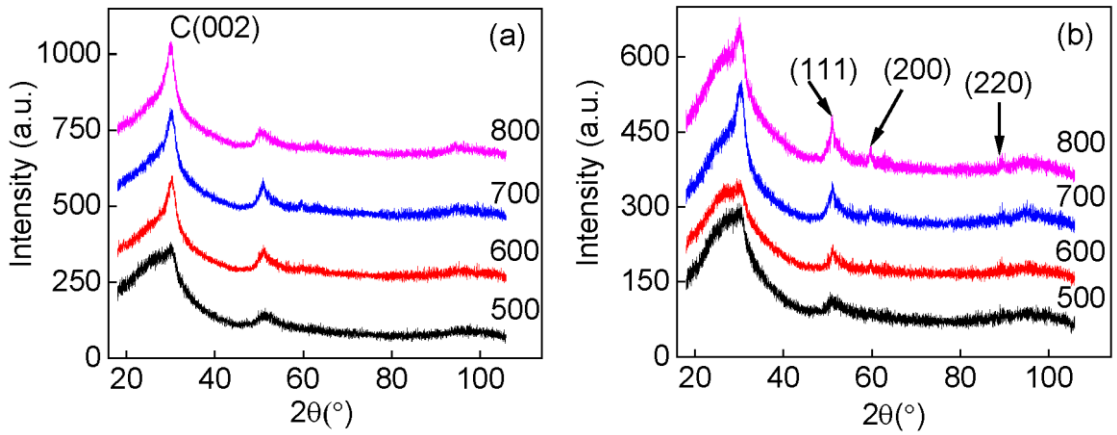

Figure (3.3). XRD patterns of (a) NC/Fe (b) SiO_2/NC/Fe pyrolyzed at 500 °C, 600 °C, 700 °C, and 800 °C.

3.5.4 TEM of NC/Fe

TEM images of NC/Fe and SiO_2/NC/Fe pyrolyzed at 800 °C are given in Figure 3.**4**. Turbostratic carbon shows a combination of ribbon morphology and areas of amorphous carbon as can be seen in the TEM image of NC/Fe (Figure **3.4a**). Polyaromatic layers arranged in turbostratic biperiodic order are indicated by the lattice fringes and are highlighted in the HRTEM image of NC/Fe (Figure **3.4b**). The interlayer spacing is 0.3586 nm. The SAED pattern of NC/Fe (Figure **3.4c**) shows (002), (10), and (11) diffraction rings. The (002) diffraction ring indicates the presence of graphitic ordered carbon and (10) and (11) diffraction rings indicate the presence of turbostratic carbon. The presence of these diffractions is consistent with the results from XRD. Fe nanoparticles could not be seen in the TEM images. This is believed to be due to dissolution of the nanoparticles during the washing step after etching SiO_2. The presence and position of the nanoparticles in both the carbon matrix and in the graphitic domains, was observed in the unetched, SiO_2/NC/Fe sample. The distribution of NPs in the carbon matrix is shown in the TEM image of SiO_2/NC/Fe (Figure **3.4d**). These NPs have an average size of 28 nm. Amorphous carbon and the SiO_2 framework were also present and it is possible to see

that the turbostratic carbon and NPs are present among this matrix. The turbostratic carbon is located close to the nanoparticle as shown in the HRTEM image of SiO_2/NC/Fe (Figure **3.4e**).

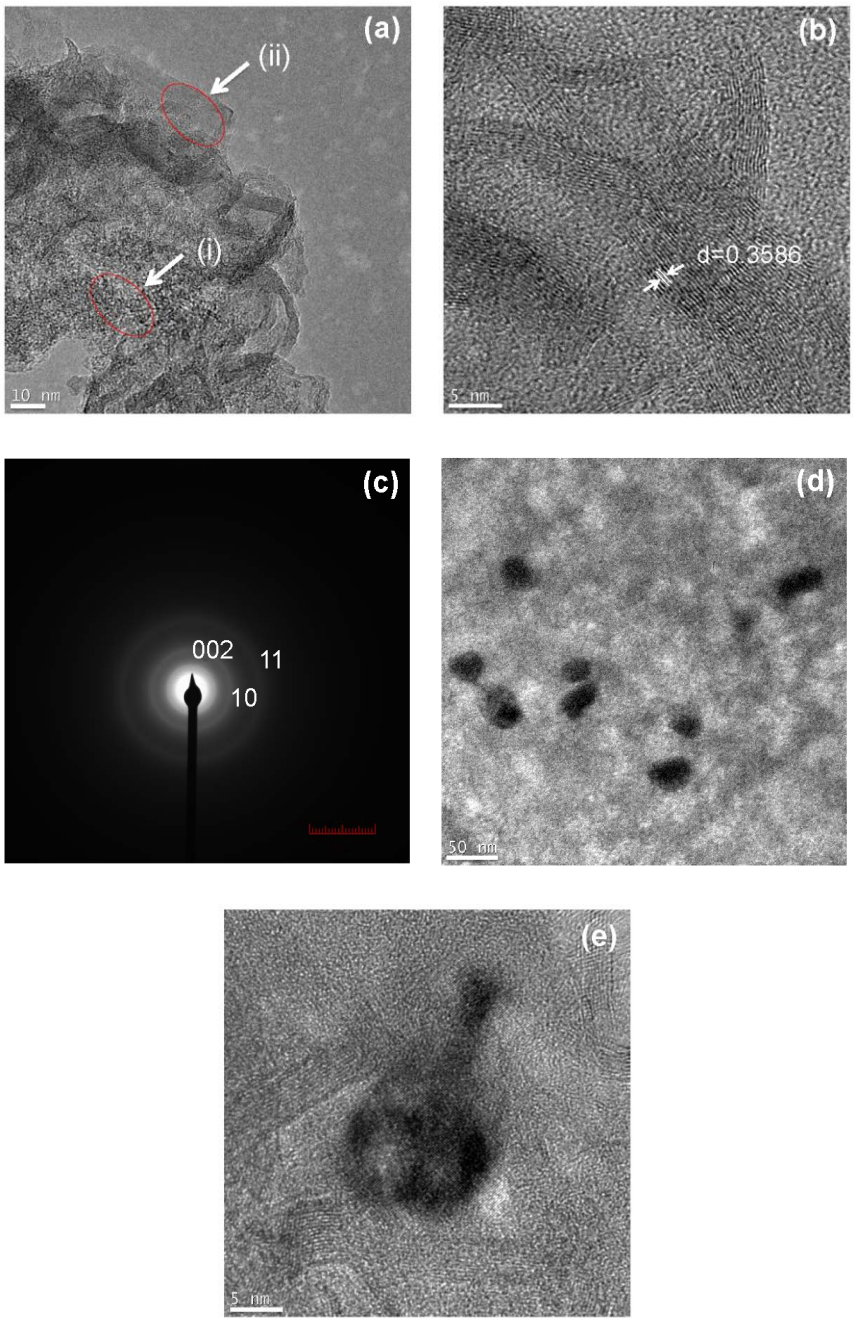

Figure (3.4). (a) TEM image (b) HRTEM image (c) SAED pattern of NC/Fe 800 (d) TEM image (e) HRTEM image of SiO_2/ NC/Fe 800. In (a) Amorphous region is labeled as (i) and Turbostratic region is labeled as (ii).

3.5.5 XRD of NC/Co

The XRD patterns of NC/Co pyrolyzed at different temperatures are shown in Figure **3.5a**. The crystallite peak of carbon was present in NC/Co samples which were pyrolyzed at 700 °C and 800 °C but not in samples pyrolyzed at 500 °C and 600 °C. The broad peak centered on about 28° is present in all samples, a feature that was observed for the NC/Fe as well. This suggests that the density of crystalline carbon in NC/Co samples pyrolyzed at 500 °C and 600 °C is not sufficient to produce a measurable diffraction peak in the XRD pattern. This observation confirms that catalytic graphitization increases with increasing temperature. The crystallite peak appeared at about 30°, and the interlayer spacing is about 0.345 nm, which is again greater than the interlayer spacing of graphite, 0.335 nm.[31] This indicates that turbostratic carbon has been produced from catalytic graphitization by Co NPs. The crystallite size is about 3.6 nm, which is 0.2 nm larger that the crystallite size found for the NC/Fe system. The broad peak observed at 28° shows the presence of amorphous carbon, to a greater extent than was found in NC/Fe. In addition to the (002) peak, the (10) and (100) peaks of carbon could be seen around 51°. Although other authors[30] have quantitatively analyzed the effect of temperature on the intensity, FWHM and peaks position of this peak in terms interference from the Co (111) diffraction peak (which appears at 52°), prevented such an analysis being carried out here. The structural changes that occur in turbostratic carbon, explained in the earlier discussion concerning NC/Fe, affect the diffraction angle and FWHM and hence the calculation of lattice parameters and crystallite size.[1] So, it is worth mentioning that the values that were calculated can give qualitative insight, but are not quantitatively accurate. As described in the discussion on NC/Fe, the inhomogeneous distribution of NPs in the monolith also contributes to variation of the parameters calculated.

The crystal state of the NPs could not be evaluated by XRD as no metallic peaks were observed. This is due to the removal of NPs during the washing of monoliths after etching SiO_2. The XRD patterns of monoliths before etching were collected in order to determine the crystal state. They are given in Figure **3.5b**. The XRD pattern of NC/Co pyrolyzed at 500 °C and 600 °C do not show any peaks which could be due to the NPs well dispersed in the carbon matrix. NC/Co pyrolyzed at 700 °C showed metallic peaks, (111) at about 52°, (200) at about 61° and (220) at about 91°. The crystallite size could not be accurately calculated as the diffraction peak (111) is fairly broad, and overlaps with the diffraction peaks of carbon. The XRD pattern of NC/Co pyrolyzed at 800 °C shows diffraction peaks at 51.53°, 53.09°, 53.81°, 57.11°, 63.28°, 81.20°, 95° that correspond to the orthorhombic phase of cobalt silicide (Co_2Si) (JCPDS card number 04-010-3523). The Co_2Si Phase was reported to form when Co thin films on Si (100) were heated to 350 °C. Further heating produced other cobalt silicide phases.[33] Therefore it appears reasonable that during the pyrolysis of NC/Co to 800 °C, metal Co was synthesized at lower temperatures and upon further heating to 800 °C, Co_2Si has formed. In other samples pyrolyzed at lower temperatures, the temperature it is not sufficient to produce detectable amounts of cobalt silicides. It has been reported that nickel silicide catalyzes the graphitization of carbon nanofibers, albeit at temperatures higher than used here.[34] This suggests that cobalt silicide might also be contributing to the graphitization of carbon for the NC/Co samples.

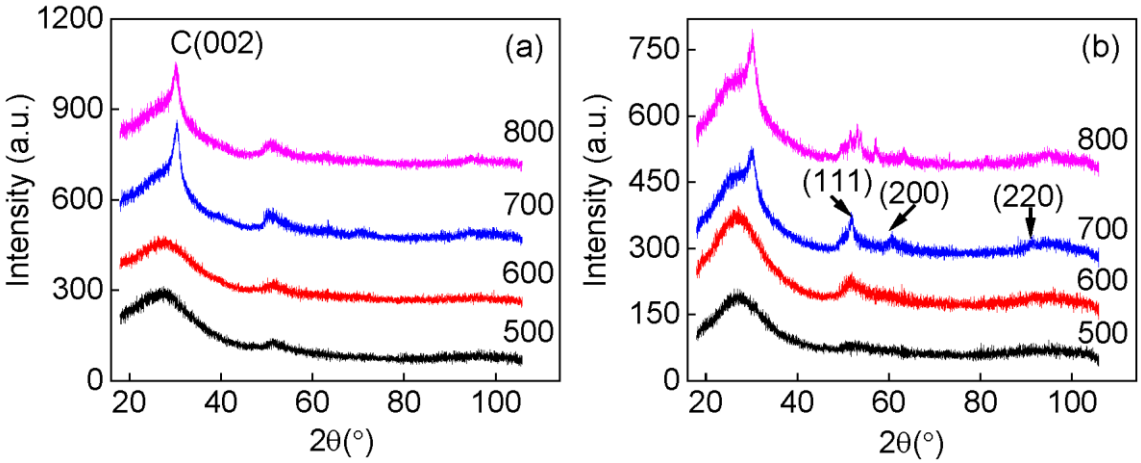

Figure (3.5). XRD patterns of (a) NC/Co (b) SiO_2/NC/Co pyrolyzed at 500 °C, 600 °C, 700 °C, and 800 °C.

3.5.6 TEM of NC/Co

TEM images of NC/Co and SiO_2/NC/Co pyrolyzed at 800 °C are given in Figure **3.6**. TEM images of SiO_2/NC/Co were taken in order to observe the nanoparticle distribution relative to the amorphous and turbostratic carbon as again, during etching and washing most of the NPs are removed. TEM image of NC/Co (Figure **3.6a**) shows the presence of both turbostratic carbon and amorphous carbon, consistent with the XRD results. The HRTEM image of NC/Co (Figure **3.6b**) shows lattice fringes that are composed of polyaromatic layers organized in turbostratic biperiodic order. The interlayer spacing is 0.3436 nm. The corresponding SAED patterns of NC/Co (Figure **3.6c**) show the (002), (10) and (11) diffraction rings. The presence of (10) and (11) diffraction rings also indicate that turbostratic carbon has been produced. The location of NPs relative to turbostratic and amorphous carbon regions was assessed using TEM images of SiO_2/NC/Co (Figure **3.6d**). These NPs have an average size of 33 nm. The HRTEM image of SiO_2/NC/Co (Figure **3.6e**) shows that turbostratic carbon is located close to the nanoparticle, consistent with cobalt NPs catalyzing carbon crystallization.

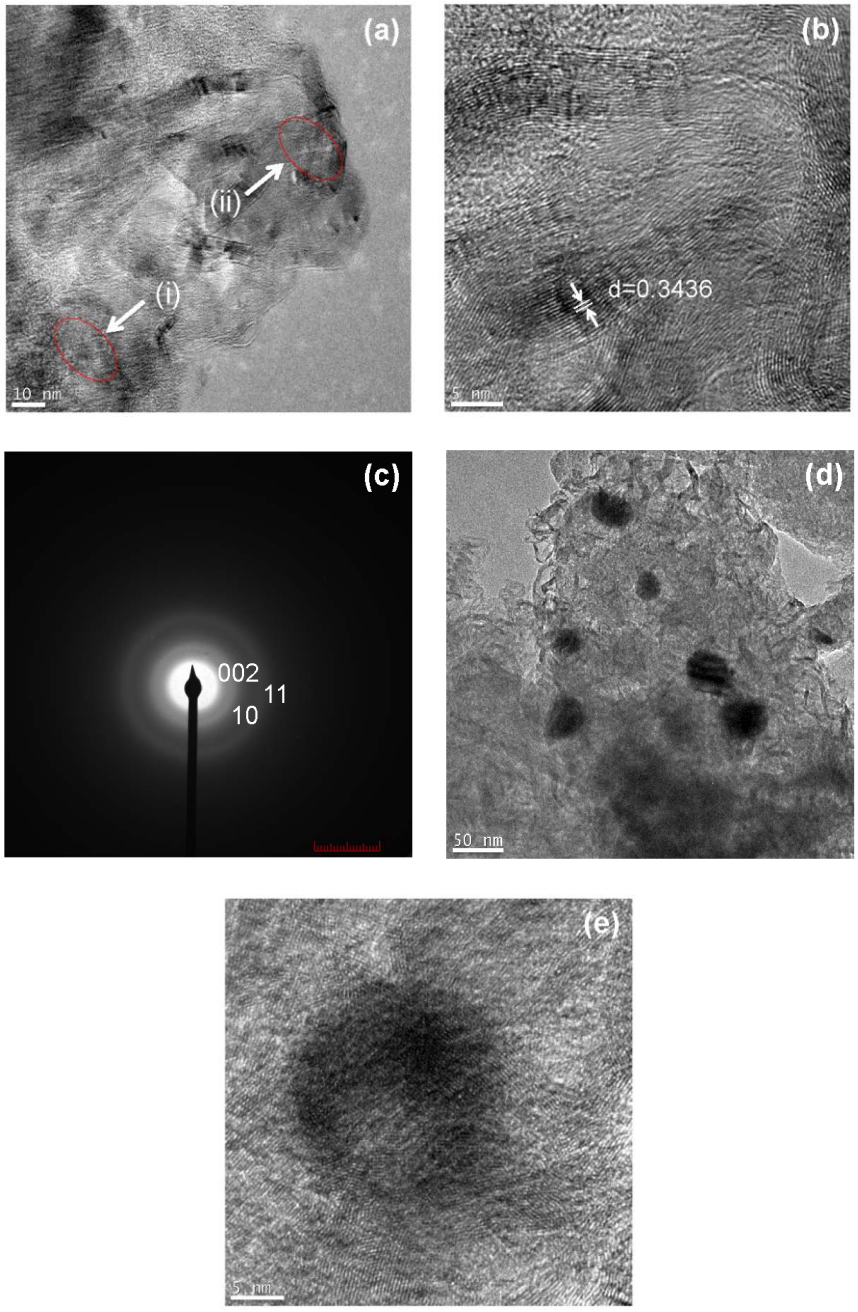

Figure (3.6). (a) TEM image (b) HRTEM image (c) SAED pattern of NC/Co 800 (d) TEM image (e) HRTEM image of SiO_2/ NC/Co 800. In (a) Amorphous region is labeled as (i) and Turbostratic region is labeled as (ii).

3.5.7 XRD of NC/Ni

The XRD patterns of NC/Ni pyrolyzed at different temperatures are given in Figure **3.7a**. The presence of the C(002) XRD peak shows that a graphitized of carbon is present in NC/Ni pyrolyzed at 700 °C and 800 °C. Again, as seen in the NC/Co samples, the turbostratic carbon crystallite peak is not observed in NC/Ni pyrolyzed at 500 °C and 600 °C. The broad peak appear at about 28° is present in these NC/Ni samples as well. These observations show that the crystallization of carbon increases with increasing temperature. The C(002) peak was at about 30° in NC/Ni pyrolyzed at 700 °C and 800 °C, corresponding to an interlayer spacing of about 0.345 nm. Once again, this interlayer spacing is greater than the interlayer spacing of graphite (0.335 nm) indicating the formation of turbostratic carbon.[31] The crystallite size is found to be the largest among the three different samples: 3.7 nm. The XRD patterns of NC/Ni also show the presence of the broad peak at about 28° indicating that amorphous carbon is present to a greater extent than is turbostratic carbon. The peak observed at 51° corresponds to the combination of (10) and (100) peaks. Again this peak overlaps with the metallic Ni (111) diffraction peak preventing any detailed analysis.[30] The structural changes in turbostratic carbon as described earlier in NC/Fe and NC/Co affect the diffraction angle and FWHM, and hence the lattice parameters and crystallite size.[1] Those quantities provide a general idea than a specific trend. The heterogeneous distribution of NPs in the monolith also contributes to such fluctuations, which has proven to be a common behavior for all the three cases studied here.

In order to evaluate the crystal state of the NPs XRD patterns of SiO_2/NC/Ni pyrolyzed at different temperatures were collected as well (Figure **3.7b**). SiO_2/NC/Ni pyrolyzed at 500 °C and 600 °C show diffractions consistent with the metallic phase of Ni. The diffraction peak at 52.11° corresponds to the Ni (111) diffraction, the peak at 61.10° corresponds to the Ni (200) diffraction

and the peak at 92.08° to the Ni (220) diffraction. Crystallite size was not calculated as the (10) and (100) diffractions of carbon also appear around that position. The XRD pattern of SiO_2/NC/Ni pyrolyzed at 700 °C showed peaks at about 46.15°, 49.74°, 50.98°, 53.30°, 57.43°, 62.82°, 80.89°, and 90.46°. These peaks can be indexed as the orthorhombic phase of nickel silicide (Ni_2Si) (JCPDS card number 04-010-3516). The peak at about 55.46° matches the orthorhombic phase of nickel silicide (NiSi) (JSPDS card number 04-003-0573) and the peaks at about 52.14°, 61.26° to the cubic phase of nickel silicide (Ni 82.00%, Si 8.00%) (JCPDS card number 04-004-4506). The peaks of SiO_2/NC/Ni pyrolyzed at 800 °C that appeared at about 50.84°, 53.29°, and 57.33° can be attributed to the orthorhombic phase of nickel silicide (Ni_2Si) (JCPDS card number 04-010-3516), the peak at about 55.28° to the orthorhombic phase of nickel silicide (NiSi) (JSPDS card number 04-003-0573) and the peaks at about 52.21°, 61.11° and 91.98° can be assigned to the cubic phase of nickel silicide (Ni 82.00%, Si 8.00%) (JCPDS card number 04-004-4506). NC/Ni samples pyrolyzed at 500 °C and 600 °C show the presence of metallic nickel and NC/Ni pyrolyzed at 700 °C and 800 °C show that different phases of nickel silicide have formed. The nickel silicide, Ni_2Si, phase is reported to start to form by heating Ni metal and silicon together at temperatures between 250 °C and 300 °C, and further increasing temperature is reported to form NiSi.[35] It could be that during pyrolysis Ni metal has formed and further increasing temperature of samples pyrolysed at 700 °C and 800 °C different phases of nickel silicide has formed. It has been reported that the nickel silicide contributes efficiently to the graphitization of carbon nanofibers.[34] So it is likely that the nickel silicide compounds formed during the pyrolysis have affected the graphitization in our work too.

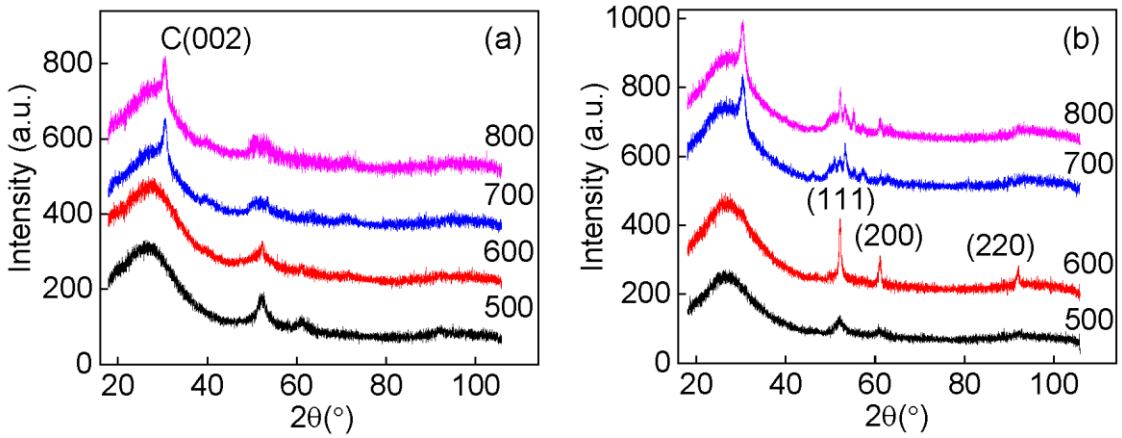

Figure (3.7). XRD patterns of (a) NC/Ni (b) SiO_2/NC/Ni pyrolyzed at 500 °C, 600 °C, 700 °C, and 800 °C.

3.5.8 TEM of NC/Ni

TEM images of NC/Ni and SiO_2/NC/Ni pyrolyzed at 800 °C are given in Figure **3.8**. TEM images of SiO_2/NC/Ni were taken to assess the NP distribution in the carbon matrix relative to the positions of amorphous and turbostratic carbon because during etching and washing NPs are washed out. Turbostratic carbon and amorphous carbon could be seen in the TEM images of NC/Ni (Figure **3.8a**). This is consistent with XRD pattern showing the presence of both types of carbon. The HRTEM image of NC/Ni (Figure **3.8b**) shows the polyaromatic layers arranged in turbostratic carbon biperiodic order. The interlayer spacing is 0.3594 nm. The SAED pattern (Figure **3.8c**) shows the carbon (002), (10) and (11) diffraction rings. The (10) and (11) diffraction rings confirm that turbostratic carbon has been produced. The distribution of NPs in the carbon matrix is shown in the TEM image of SiO_2/NC/Ni (Figure **3.8d**). These NPs have an average size of 30 nm. The HRTEM image of SiO_2/NC/Ni (Figure **3.8e**) shows that turbostratic carbon is present close to the nanoparticle. This indicates that the amorphous carbon located close to the nanoparticle was graphitized.

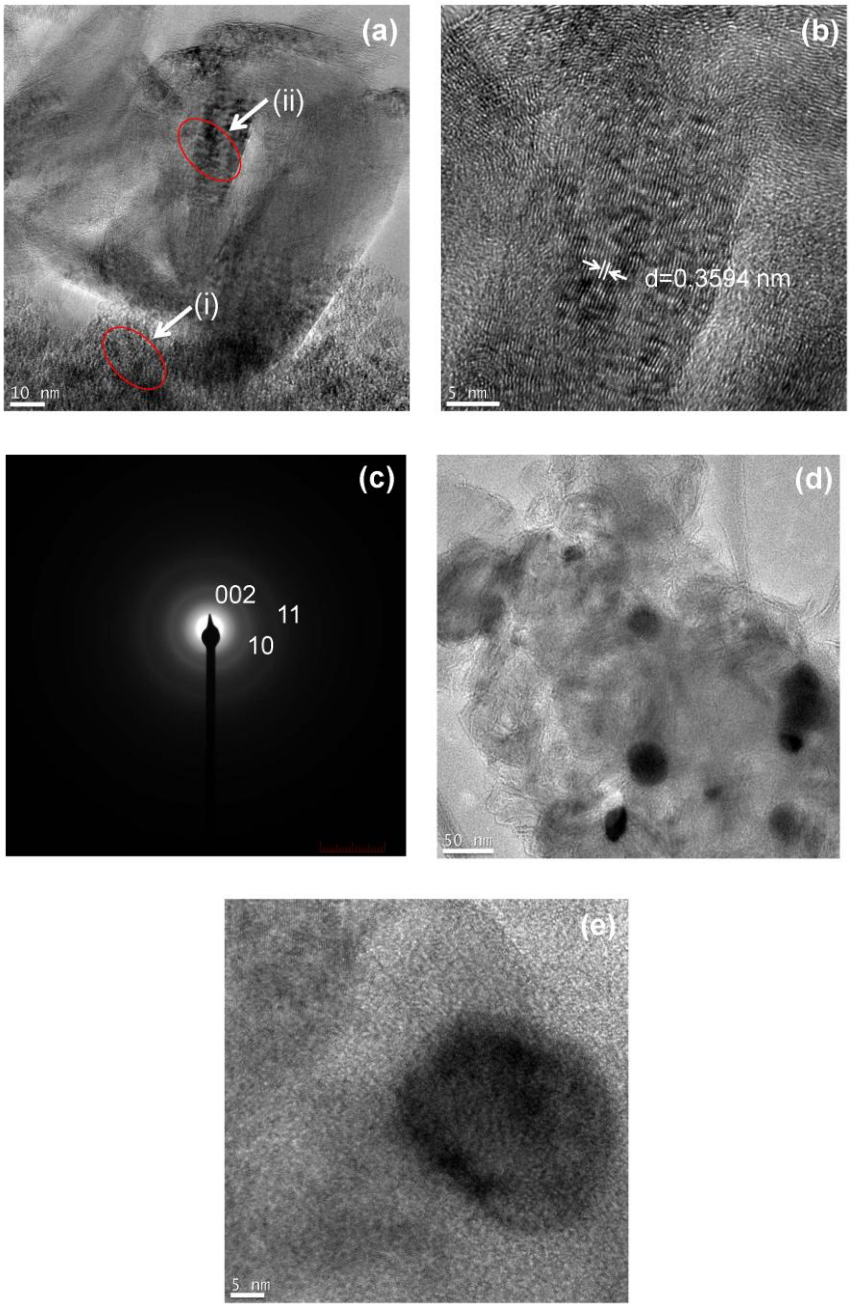

Figure (3.8). (a) TEM image (b) HRTEM image (c) SAED pattern of NC/Ni 800 (d) TEM image (e) HRTEM image of SiO_2/ NC/Ni 800. In (a) Amorphous region is labeled as (i) and Turbostratic region is labeled as (ii).

Catalytic graphitization can occur via dissolution-precipitation and carbide formation-decomposition mechanisms.[17] According to the carbide formation-decomposition mechanism the metal nanoparticle forms a metal carbide layer that converts to a graphitic layer around the metal nanoparticle when temperature is increased. Because the thermal expansion coefficients of iron, cobalt, and nickel are greater than that of graphite, when heated to high temperatures the NPs expand and pressurize the inner surface of the graphitic shell and break it and escape.[36] The escaped nanoparticle moves to another area of amorphous carbon and continues to crystallize the amorphous carbon at high temperatures. The decomposition temperature of iron carbide is 700 °C.[37] The pyrolysis at low temperatures produces Fe_3O_4 NPs that are carbothermally reduced to FeO and then to Fe with increasing temperature. The reduction of FeO to Fe is believed to occur at about 700 °C which is similar to the thermal decomposition temperature of iron carbide.[36] Peaks corresponding to iron carbide were not seen. If iron carbide had been produced, the peaks from iron carbide should have been observed in samples pyrolyzed at 500 °C and 600 °C as under these temperatures the samples are below the decomposition temperature. Samples pyrolyzed at 700 °C and 800 °C may not have those peaks as iron carbide (if formed) would probably decompose. The thermal decomposition temperature of cobalt carbide and nickel carbide are about 485 °C and 420 °C respectively.[37] We believe that peaks corresponding to cobalt carbide and nickel carbide are not present in the XRD pattern as all our samples are heated above the decomposition temperature. Catalytic graphitization is therefore believed to have occurred by dissolution-precipitation mechanism. Amorphous carbon dissolves in the nanoparticle, and precipitates as graphitic carbon.[9,12] TEM images show that turbostratic carbon is located close to the nanoparticles, and the amorphous carbon is present further away from the NPs. This suggests that it is only amorphous carbon close to the NPs that is catalytically

graphitized while amorphous carbon is not subject to crystallization without NPs as catalysts. This observation is further supported by the heterogeneous distribution of NPs in the monolith as there are amorphous carbon regions where NPs are not present. The nanoparticle concentration appears to be too low to catalyze the graphitization of all amorphous carbon as the metal nitrate was dissolved in the precursor FA, in which only one weight percent of metal is present relative to FA. NPs have previously been reported to move in the carbon matrix catalyzing the graphitization of amorphous carbon.[16,36]

The percentage of graphitic carbon was calculated by fitting the (002) peak into two Gaussian peaks which are centered at 28° and 30°, and then considering the ratio of integrated peak area to the total integrated peak area as given in Figure **3.9**. From Figure **3.9** we see that the percentage of graphitic carbon is higher in NC/Fe than NC/Co and NC/Ni and Fe is catalytically active at low temperatures. Co and Ni are found to be active at high temperatures (700 °C and 800 °C), Co being more effective than Ni.

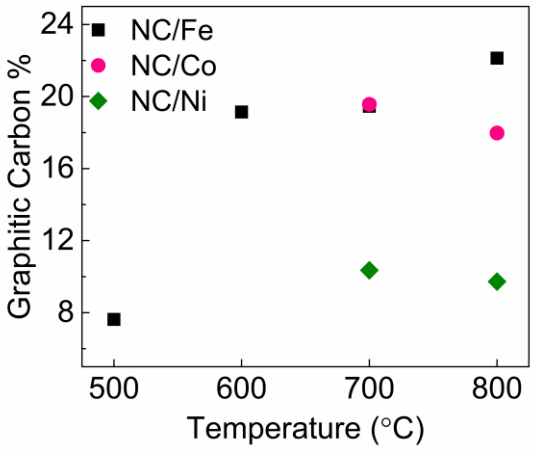

Figure (3.9). Graphitic carbon percentage of NC/Fe, NC/Co, and NC/Ni.

3.5.9 Resonant Raman Spectroscopy

Resonant Raman Spectroscopy is a well-known technique used to study vibrational properties of materials and it has been shown to be particularly powerful for studying carbon-based structures such as graphite,[38,39] carbon nanotubes,[40,41] graphene,[42,43] and amorphous carbon.[44,45] Carbon materials are an assembly of honeycomb-like layers in which these layers are connected to each other via van der Waals forces and the in-layer carbon atoms are sp^2 hybridized. The Raman spectra of disordered carbons show two distinct modes, the G peak occurring around 1580-1600 cm^{-1} (which is assigned to zone center phonons of E_{2g} symmetry) and the D peak around 1350 cm^{-1} (which corresponds to *K*- point phonons of A_{1g} symmetry).[45,46] The G peak is associated with in-plane out-of-phase vibrations of two neighboring carbon atoms (that happen to be the two carbon atoms in the unit cell of the carbon material) that are connected to each other and are sp^2 hybridized and the D peak is due to the breathing modes of the hexagons formed by the carbon atoms in the carbon materials structure.[44] The area ratio of the D and G peaks gives information about the crystallinity of the carbon structures and it is routinely used for the analysis of graphitization in disordered graphite[42,47] However, the intensity ratio of the D and G peaks are generally used for the analysis of largely disordered materials, thereby decoupling the information contained in the integrated area of the peaks into their intensity and FWHM.[45,46] As a representative case, the peak deconvolution of the G and D peaks observed for the NC sample pyrolyzed at the temperature 800 ^{o}C is given in Figure **3.10** and a third peak in addition to the D and G peaks corresponds to combination of sp^2 and sp^3 carbon that is not crystallized. The hydrogen and oxygen present in carbon can also contribute to this additional peak and so this peak gives little useful information.

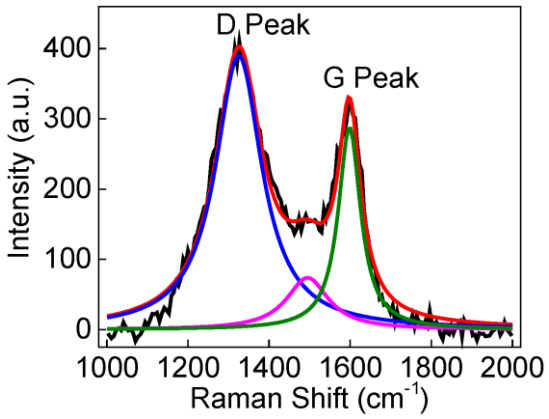

Figure (3.10). Peak deconvolution of Raman spectrum of NC 800.

The intensity ratio was found to increase with increasing temperature when the samples were excited at both 532 nm (Figure **3.11a**) and 633 nm (Figure **3.11b**) wavelengths. We observe this increase in the ratio for all the samples: NC, NC/Fe, NC/Co, and NC/Ni. The I_D/I_G ratio increases with increasing temperature because the thermal energy favors the clustering of the sp^2 phase to form the carbon hexagons in the honeycomb lattice.[45] I_D is directly proportional to the number of ordered rings and clustering of rings (the D-band is known to be a disorganization related Raman feature - a feature related to the crystallinity disorder of the crystal). Note that the I_D/I_G ratio increases with increasing disorder of graphite. When the number of defects increases, it means that the sp^2 domains decreases and the carbon hexagons, therefore, become fewer and more distorted. In fact, eventually the hexagons come to rupture creating a defect. The ratio I_D/I_G decreases if the material gets more crystalline, which in other words means more organized.[45,46] According to Lucchese *et al.*, the I_D/I_G ratio can be related to a parameter L_D which represents the distance between defective sites in the carbon material lattice.[48] In other words, L_D can be seen as a measure of the amount of disorder. The smaller the L_D, the higher the density of defective sites is and, therefore, the higher the disorder of the material is. The process of

formation of amorphous carbon from graphite usually proceeds in three stages: (1) the graphite converts to nanocrystalline graphite; (2) nanocrystalline graphite to amorphous carbon of low density sp^3 content; and (3) the low density sp^3 amorphous carbon to high density sp^3 amorphous carbon. The I_D/I_G is proportional to $1/ L_D$ in the first stage and in the second and third stages, I_D/I_G is proportional to L_D^2.[45,46] This means that when moving from stage three to stage two, the I_D/I_G ratio is expected to increase as the sample moves from essentially sp^3 carbon to a mixing of sp^2 and sp^3 carbons (note that there is no crystalline organization yet, although some parts of the material is no longer amorphous carbon). When moving from the stage two to the stage one the I_D/I_G ratio decreases and the material gets closer and closer to its crystalline sp^2 structure. In our research we aim to graphitize a sample essentially composed of amorphous carbon containing a mixture of sp^2 and sp^3 carbons. So, our experiments are making a transition from the stage three to the stage two, as described above, which is confirmed by the plot in Figure **3.11**. According to the increasing I_D/I_G ratio observed with increasing pyrolyzing temperature we believe that the amorphous carbon that is synthesized by pyrolyzing the NC samples with different catalysts at low temperature can be considered as amorphous carbon with a high density of sp^3 contents and as the temperature is increased, pyrolyzing the samples further, the density of sp^3 contents decreases and the new carbon material produced consists of amorphous carbon and nanocrystalline graphite. This is in fully agreement with the discussions and observations made in the previous sections and are fully supported by the XRD and TEM results discussed above. Indeed, when the temperature is increased, the amount of defects tends to decrease, which means that the density of crystalline carbon is increasing. As a consequence, L_D is expected to increase as well with increasing the temperature. Incorporating more catalyst metals and pyrolyzing at

higher temperatures are some of strategies that could produce carbon materials with a higher crystallinity to eventually produce few layers of carbon atoms or even graphite.

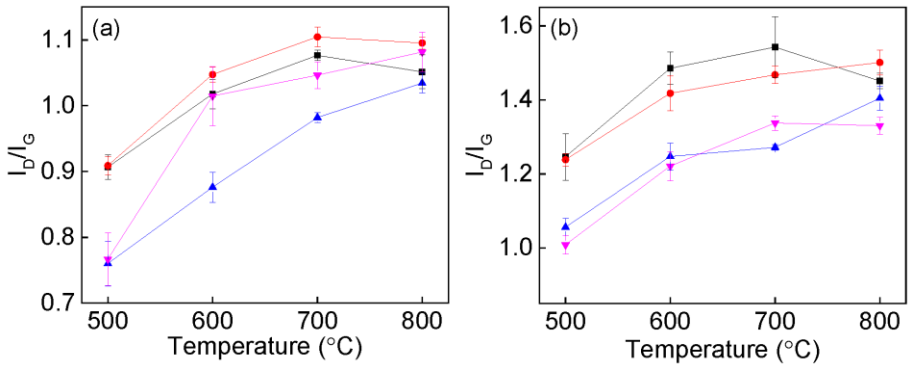

Figure (3.11). I_D/I_G ratio at (a) 532 nm and (b) 633 nm laser wavelengths of NC (black), NC/Fe (red),NC/Co (blue), and NC/Ni (purple) pyrolyzed at 500 °C, 600 °C, 700 °C, and 800 °C.

The FWHM is a measure of the structural disorder as well.[46] The FWHM (Γ) of the D and G peaks generally increase with increasing disorder.[42,46] Accordingly, the ratio between the FWHM for the D and G peaks (Γ_D/Γ_G) is analyzed, for each sample, as the temperature increases, as shown in Figure **3.12**. Figure **3.12** shows, for all the samples NC, NC/Fe, NC/Co, and NC/Ni, that the Γ_D/Γ_G tends to decrease with increasing temperature. Figure **3.12a** shows the results for the samples excited at 532 nm and Figure **3.12b** shows the results for the samples excited at 632 nm. Once again we have a confirmation that the NC samples with different metal catalysts become more ordered when temperature is increased.

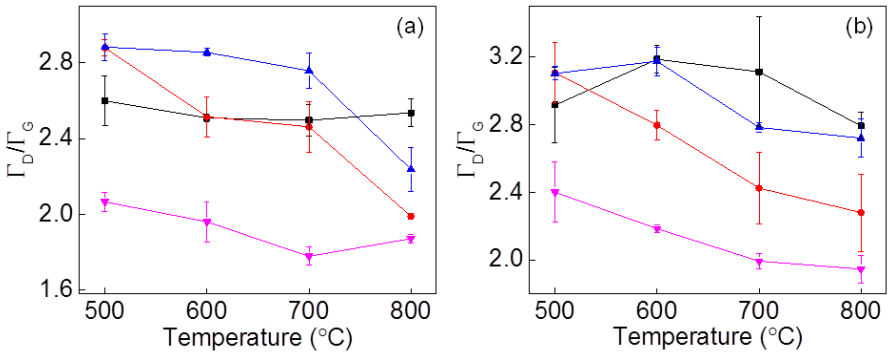

Figure (3.12). Γ_D/Γ_G ratio at (a) 532 nm and (b) 633 nm laser wavelengths of NC (black), NC/Fe (red), NC/Co (blue), and NC/Ni (purple) pyrolyzed at 500 °C, 600 °C, 700 °C, and 800 °C.

The position of the D band appeared in the region of 1340-1355 cm^{-1} when the samples are excited from laser of 532 nm wavelength and 1320 cm^{-1}-1330 cm^{-1} from 633 nm wavelength as shown in Figure **3.13a** and **b**, respectively. The D peak is expected to change its position with change in the wavelength of excitation.[44] The peak position of the G band was around 1600 cm^{-1} in NC, NC/Fe, NC/Co, and NC/Ni at both 532 nm (Figure **3.13c**) and 633 nm (Figure **3.13d**) laser wavelengths.

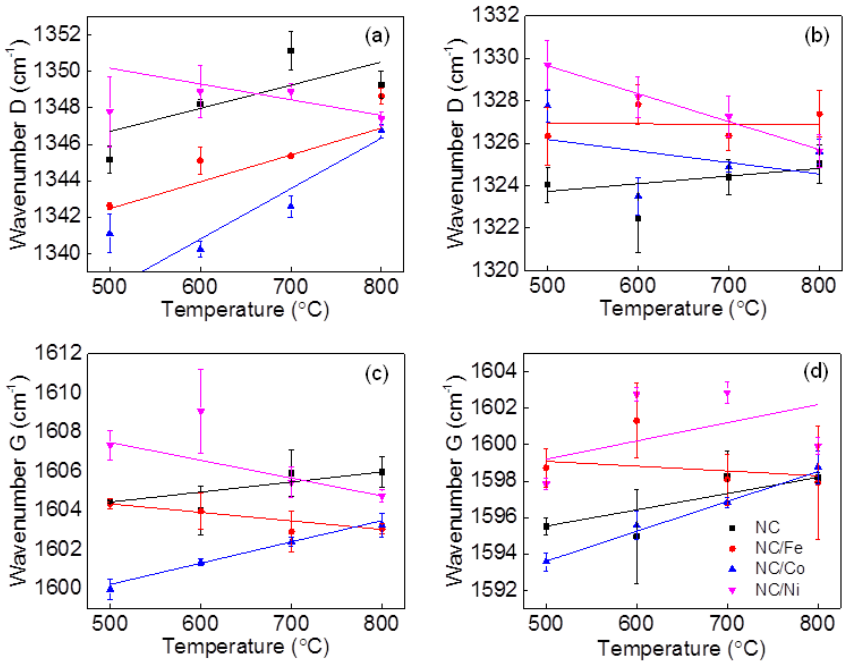

Figure (3.13). Peak position of D from (a) 532 nm (b) 633 nm laser irradiation and G band from (c) 532 nm and (d) 633 nm laser irradiation of NC (black), NC/Fe (red), NC/Co (blue), NC/Ni (purple) pyrolyzed at 500 °C, 600 °C, 700 °C, and 800 °C.

The G peak appears in graphite at 1581 cm^{-1}.[45] The G peak could be due to the presence of nanocrystalline graphite. When the carbon is converted from graphite to nanocrystalline graphite it has been found that the G peak shifted from 1580 cm^{-1} to about 1600 cm^{-1}.[45] This is due to the appearance of a D' peak around 1615 cm^{-1}, that merges with the G peak and shifts the G peak to higher Raman shift. The D' peak is believed to be due to the edges of graphitic

crystallites.[49] This peak becomes more dominant because of the high percentage of the edges which results from the decreased size of graphitic crystallites.[36] In NC, there is higher percentage of nanocrystalline graphitic crystallites as shown in the HRTEM image (Figure **3.2b**) that produces a higher amount of edges. In metal loaded NC the crystallite carbon is present and could be seen in the HRTEM images. The proportion of edges in crystallite turbostratic carbon is low when compared with the amorphous carbon (NC) decreasing the contribution from the D' peak and giving a more pronounced G peak.

The second order Raman spectra of NC, NC/Fe, NC/Co, and NC/Ni pyrolyzed at all temperatures are given in Figure **3.14a, b, c,** and **d,** respectively. The given spectra were acquired using 532 nm laser wavelength. Peak deconvolution of NC/Fe 800 is given in Figure **3.14e**. These four peaks are attributed to the overtones of vibrations.[50] The peak at about 2530 cm^{-1} could be the peak appearing around 2450 cm^{-1} in the literature which was attributed to the overtone mode of longitudinal optical phonon.[51] The peak appearing around 2700 cm^{-1} can be attributed to the G' peak which is believed to be the first overtone of the D band.[52] This band is a Raman allowed mode for sp^2 carbons.[53] The band around 2925 cm^{-1} can be assigned to the D+G overtone combination that is also induced by disorder.[54] The band appearing at around 3188 cm^{-1} could be assigned to the 2D' which is the second harmonic of the D' peak.[55] Figure **3.14a** shows a broad band from 2100 cm^{-1}-3500 cm^{-1}. In disordered carbon the second order Raman features appear as a broad band. In metal loaded carbon samples, it can be seen that the appearance of the G' becomes more prominent as indicated by decreasing FWHM with increasing temperature. For all samples the peaks are much broader when the pyrolyzing temperature is lower. The G' band becomes more prominent as a single peak with increasing temperature, indicating the formation of turbostratic carbon with increasing temperature. In graphitic carbon the G' band appears as a

double band.[56] In turbostratic carbon the G' appears as a single Lorentzian peak similar to monolayer graphene due to the absence of interlayer interactions between graphene layers.[31] This observation shows that with increasing temperature, amorphous carbon is converted to turbostratic carbon in the presence of metal NPs. This is consistent with the XRD patterns and TEM images which also show the presence of turbostratic carbon with increasing temperature.

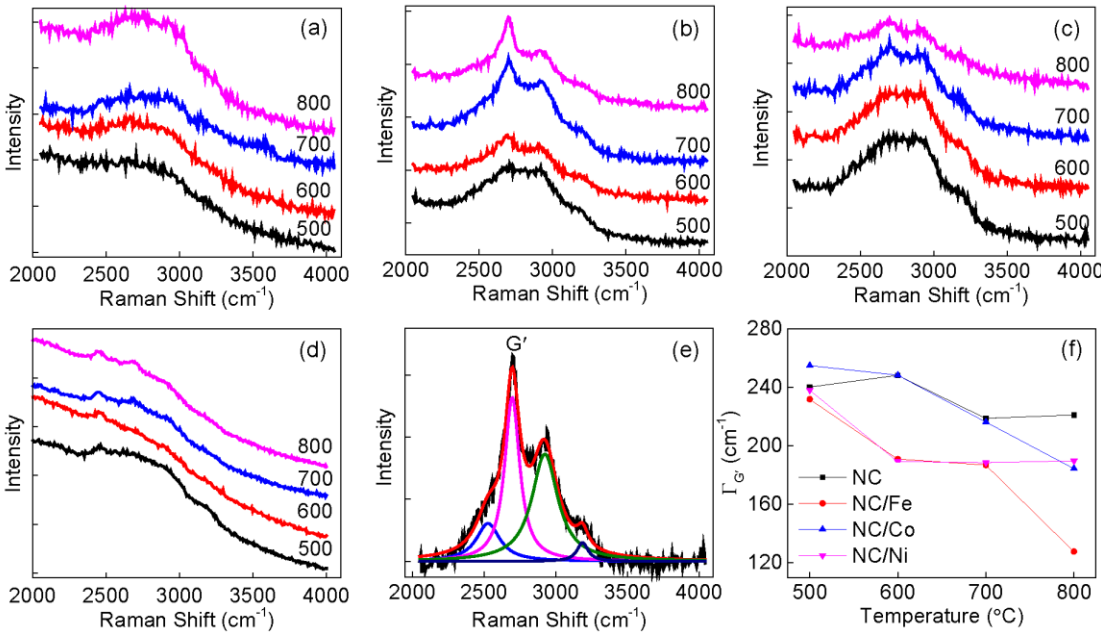

Figure (3.14). Second order Raman spectra of (a) NC, (b) NC/Fe, (c) NC/Co, and (d) NC/Ni pyrolyzed at 500 °C, 600 °C, 700 °C, and 800 °C (e) peak deconvolution of second order Raman spectrum of NC/Fe 800 (f) Γ variation of G' band with temperature of all samples.

3.5.10 XPS Analysis

The chemical bonds in carbon and oxygen, and the oxidation state of the metals synthesized were determined by XPS analysis. High resolution spectra of carbon, oxygen, and metals in the composites are given in Figure **3.15**. The spectrum of C 1s (Figure **3.15a**) shows the graphitic carbon feature at 284.60 eV,[57] carbon bound to oxygen with a single bond at 285.55 eV, and in ester at 288.32 eV.[58] The peak appearing at 290.71 eV could be attributed to a shake -

up peak of carbon. The high resolution spectrum of O 1s (Figure **3.15b**) consists of peaks from the oxygen bound to carbon by single bond (531.43 eV), and by a double bond (532.83 eV). The peak at 534.14 eV could be assigned to the hydroxyl groups present in carbon. The high resolution spectra of Fe (Figure **3.15c**), Co (Figure **3.15d**), and Ni (Figure **3.15e**) show spin orbital coupling of the 2p orbital as $2p_{3/2}$ and $2p_{1/2}$. In the high resolution spectra of NC/Fe the peak due to the $2p_{3/2}$ is observed at 711.63 eV, but is not due to elemental Fe which is expected to be at 706.6 eV.[59] This indicates the presence of oxidized iron which would appear to be Fe^{3+}, as Fe in the +3 oxidation state is reported to appear at 710.0 eV.[59] It might also be from Fe (III) in $Fe(OH)_3$. In Fe shake - up peaks were not observed. The high resolution spectra of both Co and Ni in NC/Co and NC/Ni respectively show four peaks corresponding to spin orbital coupling of the 2p orbital as $2p_{3/2}$ and $2p_{1/2}$ and their shake-up peaks. The peak at lower binding energy with high intensity is the $2p_{3/2}$ and the peak adjacent to it on the high binding energy side with low intensity is the shake-up peak. The peak at higher binding energy with lower intensity than $2p_{3/2}$ peak but higher intensity than other peaks is the $2p_{1/2}$ peak and the peak adjacent to it at high binding energy side with low intensity is the shake-up peak of $2p_{1/2}$. In Co zero oxidation state $2p_{3/2}$ should appear at 778.1 eV[59] but a peak is seen at around 781.50 eV. Furthermore, the other peaks are also shifted to higher binding energy indicating that oxidized cobalt has formed and that probably indicates the presence of $Co(OH)_2$. Similar multiple peaks were observed in Ni also where the presence of multiple peaks indicates that different oxidation states are present. The $2p_{3/2}$ of metallic Ni should appear around 852.6 eV,[59] suggesting that the peak seen at 856.28 eV is instead due to nickel in a positive oxidation state (+2) which could indicate the presence of $Ni(OH)_2$.[60] XRD patterns showed the crystal state as the metal in some of the patterns, but XPS revealed that the surface is oxidized. This could be that the surface of the NPs

is oxidized but the core may not be. Further, during etching an alkaline medium is used and that may have caused the formation of surface metal hydroxides and metal oxides.

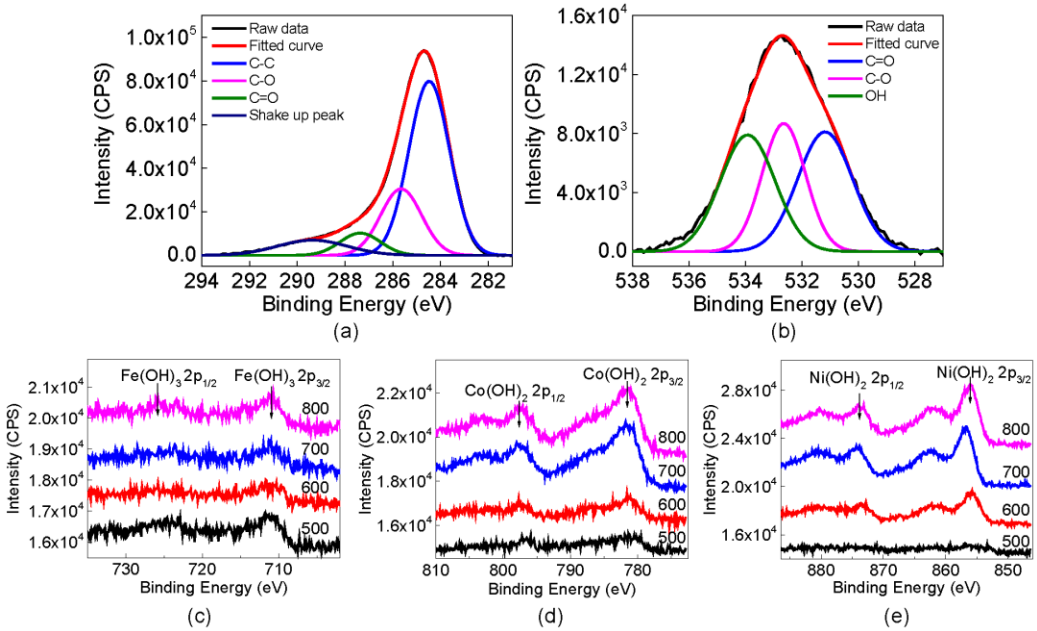

Figure (3.15). XPS high resolution spectra of (a) C 1s (b) O 1s in NC pyrolyzed at 800 °C (c) Fe 2p in NC/Fe, (d) Co 2p in NC/Co, and (e) Ni 2p in NC/Ni pyrolyzed at 500, 600, 700, and 800 °C.

3.5.11 N_2 Sorption

The textural parameters of the monolithic composites have been evaluated by N_2 sorption analysis. Figure **3.16a** shows the isotherms of SiO_2, and NC, NC/Fe, NC/Co and NC/Ni pyrolyzed at 800°C. One pyrolysis temperature was selected to show the behavior as samples pyrolyzed at other temperatures behave similarly. The isotherm of SiO_2 shows two N_2 uptakes. The first region appeared around $P/P_0 = 0.4$ is due to the filling of surfactant mesopores and the second region, that appeared around $P/P_0 = 0.9$ is due to the filling of textural mesopores.[25] The isotherms of NC, NC/Fe, NC/Co and NC/Ni pyrolyzed at 800 °C show an uptake around $P/P_0 = 0.4$ indicating the presence of surfactant mesopores, but the uptake around $P/P_0 = 0.9$ is very low because textural mesopores are relatively well filled with carbon. It can be clearly seen in the

isotherms of NC/Fe, NC/Co and NC/Ni pyrolyzed at 800 °C that the loop area corresponding to surfactant mesopores is much lower than that in NC 800. This results from the inversion of the SiO_2 mesopore structure: the SiO_2 template has mesopores which are all of diameter (which gives rise to a narrow pore size distribution), but the mesopores do not form ordered arrays, hence the SiO_2 mesopore walls are of varying thickness. On replication that gives mesopores of variable diameter. According to the BJH adsorption branch pore size distribution curves (Figure **3.16b**) the average pore size of NC is greater than that of SiO_2. The BJH pore size of SiO_2 is at 3.40 nm, and that of NC, NC/Fe, NC/Co and NC/Ni pyrolyzed at 800 °C are 4.32 nm, 3.11nm, 4.34 nm and 3.12 nm respectively. The data on N_2 sorption analysis of all the samples are given in Table **3.1**. The pore size distribution curves of SiO_2 show a narrow pore size distribution which is consistent with the C_{18}TAB used as the porogen to synthesize SiO_2. But the curves of the replica show broader pore size distributions. Mesopore walls of the disordered mesoporous SiO_2 have variable thickness due to the randomly spacing of the surfactant mesopores. Nanocasting gives a negative replica at the nanoscale producing broader pore size distribution.[61,62] Nanocast carbon produced from the ordered mesoporous SiO_2, has a narrower pore size distribution as the wall thickness of the parent SiO_2 is no longer random.[62]

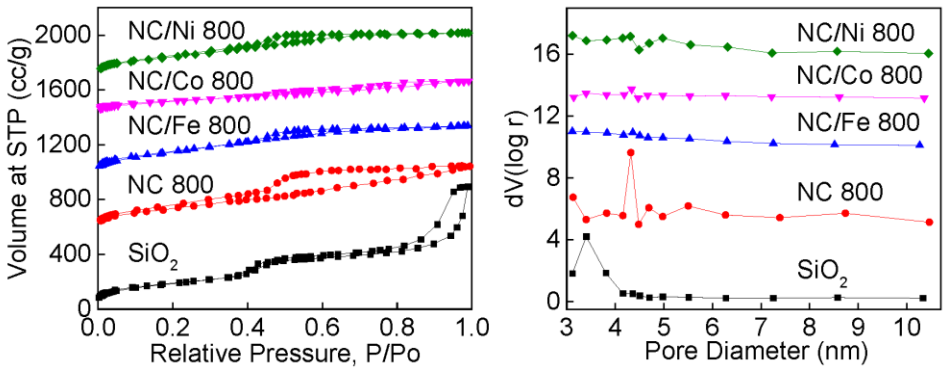

Figure (3.16). (a) N_2 Sorption isotherms (b) BJH adsorption pore size distribution curves of SiO_2 and NC, NC/Fe, NC/Co and NC/Ni pyrolyzed at 800 °C.

Table **3.1.** Textural parameters of the monoliths synthesized.

Sample	BET Surface Area (m^2/g)	Total Pore Volume (cc/g)	Mesopore Volume (cc/g)	Micropore Volume (cc/g)	BJH Method Adsorption Pore Diameter (nm)
SiO_2	671	0.58	0.58	0.00	3.40
NC 500	730	0.50	0.46	0.04	3.13
NC 600	621	0.45	0.448	0.002	3.40
NC 700	556	0.41	0.406	0.004	4.29
NC 800	823	0.56	0.52	0.04	4.32
NC/Fe 500	658	0.44	0.37	0.07	3.41
NC/Fe 600	683	0.49	0.44	0.05	3.38
NC/Fe 700	573	0.40	0.37	0.03	3.12
NC/Fe 800	885	0.59	0.55	0.04	3.11
NC/Co 500	714	0.49	0.45	0.04	3.11
NC/Co 600	777	0.53	0.47	0.06	4.37
NC/Co 700	640	0.44	0.41	0.03	4.35
NC/Co 800	415	0.28	0.25	0.03	4.34
NC/Ni 500	894	0.60	0.51	0.09	3.12
NC/Ni 600	797	0.57	0.48	0.09	3.11
NC/Ni 700	932	0.65	0.60	0.05	3.38
NC/Ni 800	836	0.57	0.51	0.06	3.12

The isotherms for samples before etching, NC/SiO_2/Fe, NC/SiO_2/Co, NC/SiO_2/Ni pyrolyzed at 800 °C are given in Figure **3.17a**. The uptake at relative pressure of 0.4 is relatively low indicating the filling of surfactant mesopores from carbon and the textural mesopores are mostly completely filled, consistent with the disappearance of the loop at around P/Po = 0.9 which shows the uptake from the textural mesopores. The greatly reduced mesopore volume in those samples further supports the mesopores being filled with carbon. Therefore the monoliths before etching have low surface area. The BJH adsorption branch pore size distribution curves of those samples (Figure **3.17b**) show that the maximum peak position has reduced indicating the filling of mesopores. The textural parameters of these samples are given in Table **3.2**. Upon etching the mesopore volume has increased and the uptake at relative pressures around 0.4 is

pronounced. But the loop corresponding to textural mesopores is not present indicating that FA polymerization has also occurred in textural mesopores. The surface area, total pore volume, mesopore volume and micropore volume could not be compared from sample to sample in NC/Fe, NC/Co, and NC/Ni as the metal NPs in the carbon monolith are washed out during etching and washing after etching. Metal NPs reduce the pore volumes as they fill the mesopores partially or completely reducing the mesopore volume. This would generate some micropores increasing the micropore volume and at the same time metal nanoparticles could also completely cover the micropores reducing the micropore volume. Since the metal NPs are only partially washed out, these parameters cannot be compared from sample to sample. All these parameters affect the surface area. But we can see that all the samples have high surface areas, considerable mesopore volumes and micropore volumes.

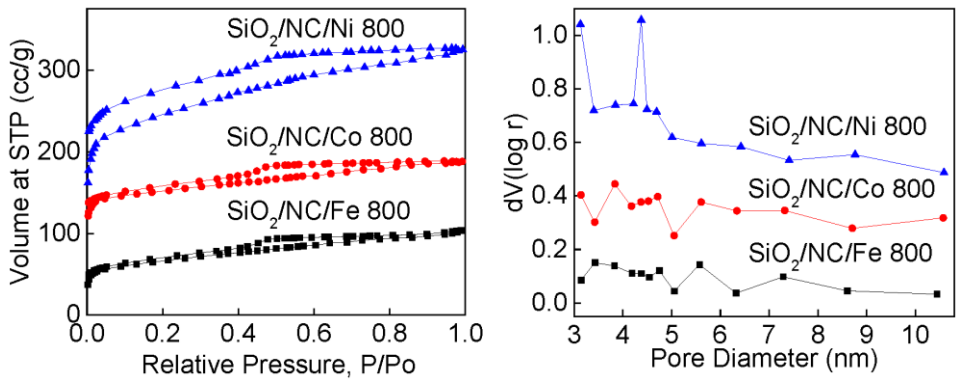

Figure (3.17). (a) N_2 sorption isotherms (b) BJH adsorption pore size distribution curves of SiO_2/NC/Fe, SiO_2/NC/Co and SiO_2/NC/Ni pyrolyzed at 800 °C.

Table **3.2.** Textural parameters of the replicated monoliths before etching.

Sample	BET Surface Area (m^2/g)	Total Pore Volume (cc/g)	Mesopore Volume (cc/g)	Micropore Volume (cc/g)	BJH Method Adsorption Pore Diameter (nm)
SiO_2/NC/Fe 500	338	0.20	0.15	0.05	3.42
SiO_2/NC/Fe 600	342	0.20	0.13	0.07	4.41
SiO_2/NC/Fe 700	368	0.21	0.13	0.08	4.20
SiO_2/NC/Fe 800	219	0.13	0.10	0.03	3.43
SiO_2/NC/Co 500	395	0.23	0.15	0.08	3.13
SiO_2/NC/Co 600	421	0.24	0.15	0.09	3.13
SiO_2/NC/Co 700	440	0.25	0.18	0.07	3.15
SiO_2/NC/Co 800	172	0.11	0.105	0.005	3.84
SiO_2/NC/Ni 500	421	0.23	0.12	0.11	3.13
SiO_2/NC/Ni 600	319	0.18	0.10	0.08	4.42
SiO_2/NC/Ni 700	244	0.15	0.11	0.04	4.38
SiO_2/NC/Ni 800	575	0.35	0.28	0.07	3.13

3.5.12 SEM Analysis

The SEM images (Figure **3.18**) show the macropore structure of the monoliths. It can be seen from the images that the macropore structure of SiO_2 (Figure **3.18a**) is retained in NC 800, NC/Fe 800, NC/Co 800, and NC/Ni 800 (Figure **3.18b, c, d,** and **e,** respectively) and they are a positive replica of SiO_2, as expected from previous work.[26,27]

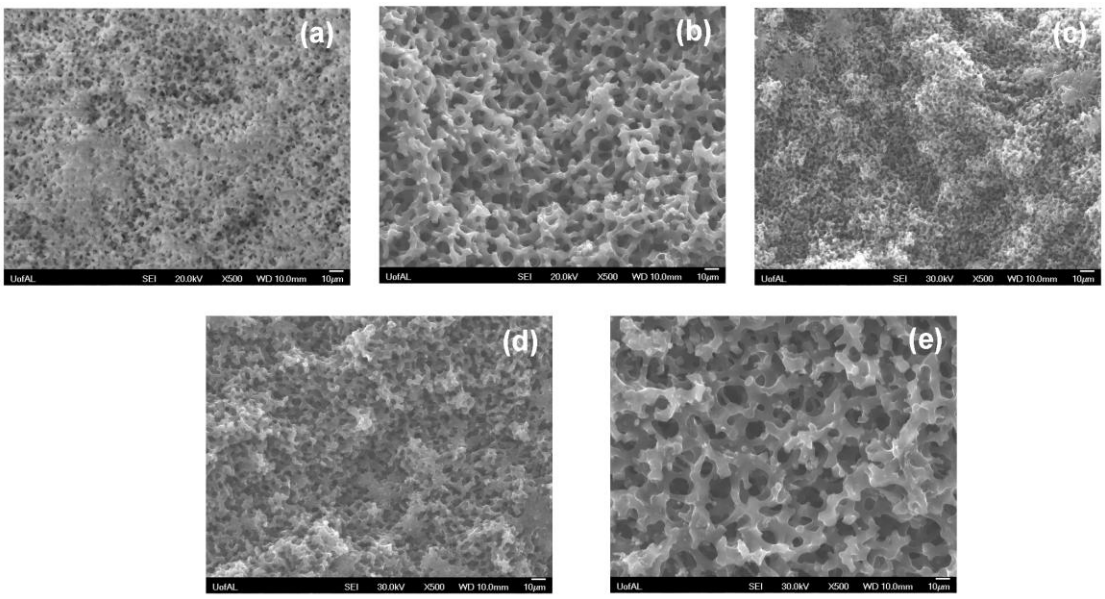

Figure (3.18). SEM images of (a) SiO_2 (b) NC 800 (C) NC/Fe 800 (d) NC/Co 800 and (e) NC/Ni 800.

The graphitic carbon is more thermodynamically stable as indicated by negative free energy change in converting disordered carbon to graphite.[9] The graphitization process involves breaking bonds in disordered carbon and formation of bonds to give ordered carbon. These processes require energy and the activation energy for the uncatalyzed graphitization is reported to be >1000 kJ mol^{-1}.[12] This value can be attributed to a rate determining step of mass-transport self-diffusion by a defect mechanism. In catalytic graphitization the activation energy has been found to be much lower than for uncatalyzed graphitization. The rate determining step could be the movement of NPs through the carbon framework or the carbon dissolution and precipitation in the nanoparticle.[12] These processes require energy and increasing temperature provides the energy required. This is certainly consistent with the higher amount of graphitization produced by higher pyrolyzing temperatures.

The d-orbitals of transition metals like Fe, Co, and Ni are filled with six, seven, and eight electrons respectively. The energy levels of configurations in these metals are hardly changed

when accepting electrons from carbon and it is understood that carbon form positive ions. Consequently, these metals can dissolve carbon and catalytically graphitized carbon by a dissolution-precipitation mechanism.[11] On the other hand metals in group IVb-VIIb like Ti, Cr, and Mn have from two to five electrons in the d-orbitals and therefore they form strong chemical bonds with carbon such as metal carbides. These metals catalytically graphitize carbon by carbide formation-decomposition mechanism.[11] This explanation is further supported by the compounds found if the carbons are quenched: metals such as Ti and Cr have formed metal carbides, while Fe, Co, and Ni produce metals containing carbon.[11] Furthermore the standard enthalpy of formation of carbides in Ti, Cr, and Mn are smaller than that in Fe and Ni indicating that the carbide formation is feasible in those metals.[63] So it can be concluded that catalytic graphitization in this work has occurred in dissolution-precipitation mechanism.

3.6 Conclusions

Metal (Fe, Co, Ni) incorporated carbon monoliths could be synthesized by nanocasting as a one pot synthesis, pyrolyzing at four temperatures in the range of 500 °C-800 °C. From the XRD patterns, the turbostratic crystallite carbon peak started appearing at 500 °C due to iron catalyzing the graphitization. For carbon incorporating Co and Ni this peak was first observed at 700 °C. The TEM and HRTEM images revealed the presence of turbostratic and amorphous carbon in metal loaded carbon indicating that metals have catalyzed the graphitization of some amorphous carbon but the treated temperature and the amount of metal loading is not sufficient to produce completely graphitic carbon. In the absence of metal NPs no graphitization is observed. From the percentage of graphitic carbon calculated from XRD data, the catalytic activity of iron is greater than of cobalt and nickel, and that of cobalt is greater than nickel. Raman analysis show an increase of intensity ratio and a decrease of FWHM ratio of the D and

G bands indicating the ordering of material with increasing temperature. Our analysis indicates that the catalytic graphitization has occurred by dissolution-precipitation mechanism.

3.7 References

(1) Li, Z. Q.; Lu, C. J.; Xia, Z. P.; Zhou, Y.; Luo, Z.: X-ray diffraction patterns of graphite and turbostratic carbon. *Carbon* **2007**, *45*, 1686-1695.

(2) Dresselhaus, M. S.; Jorio, A.; R.Saito: Characterizing Graphene, Graphite, and Carbon Nanotubes by Raman Spectroscopy. *Annual Review of Condensed Matter Physics* **2010**, *1*, 89-108.

(3) Sun, B.; Skyllas-Kazacos, M.: Chemical modification of graphite electrode materials for vanadium redox flow battery application—part II. Acid treatments. *Electrochimica Acta* **1992**, *37*, 2459-2465.

(4) Nika, D. L.; Ghosh, S.; Pokatilov, E. P.; Balandin, A. A.: Lattice thermal conductivity of graphene flakes: Comparison with bulk graphite. *Applied Physics Letters* **2009**, *94*, 203103.

(5) Hsiao, M.-C.; Liao, S.-H.; Yen, M.-Y.; Teng, C.-C.; Lee, S.-H.; Pu, N.-W.; Wang, C.-A.; Sung, Y.; Ger, M.-D.; Ma, C.-C. M.; Hsiao, M.-H.: Preparation and properties of a graphene reinforced nanocomposite conducting plate. *Journal of Materials Chemistry* **2010**, *20*, 8496-8505.

(6) Yudasaka, M.; Kikuchi, R.; Matsui, T.; Kamo, H.; Ohki, Y.; Yoshimura, S.; Ota, E.: Graphite thin film formation by chemical vapor deposition. *Applied Physics Letters* **1994**, *64*, 842-844.

(7) Kuang, Q.; Xie, S.-Y.; Jiang, Z.-Y.; Zhang, X.-H.; Xie, Z.-X.; Huang, R.-B.; Zheng, L.-S.: Low temperature solvothermal synthesis of crumpled carbon nanosheets. *Carbon* **2004**, *42*, 1737-1741.

(8) Charinpanitkul, T.; Tanthapanichakoon, W.; Sano, N.: Carbon nanostructures synthesized by arc discharge between carbon and iron electrodes in liquid nitrogen. *Current Applied Physics* **2009**, *9*, 629-632.

(9) Ōya, A.; Marsh, H.: Phenomena of catalytic graphitization. *Journal of Materials Science* **1982**, *17*, 309-322.

(10) Krivoruchko, O. P.; Maksimova, N. I.; Zaikovskii, V. I.; Salanov, A. N.: Study of multiwalled graphite nanotubes and filaments formation from carbonized products of polyvinyl alcohol via catalytic graphitization at 600–800 C in nitrogen atmosphere. *Carbon* **2000**, *38*, 1075-1082.

(11) Ōya, A.; Ōtani, S.: Catalytic graphitization of carbons by various metals. *Carbon* **1979**, *17*, 131-137.

(12) Marsh, H.; Crawford, D.; Taylor, D. W.: Catalytic graphitization by iron of isotropic carbon from polyfurfuryl alcohol, 725–1090 K. A high resolution electron microscope study. *Carbon* **1983**, *21*, 81-87.

(13) Maldonado-Hódar, F. J.; Moreno-Castilla, C.; Rivera-Utrilla, J.; Hanzawa, Y.; Yamada, Y.: Catalytic Graphitization of Carbon Aerogels by Transition Metals. *Langmuir* **2000**, *16*, 4367-4373.

(14) Ōya, A.; Ōtani, S.: Influences of particle size of metal on catalytic graphitization of non-graphitizing carbons. *Carbon* **1981**, *19*, 391-400.

(15) Mochida, I.; Ohtsubo, R.; Takeshita, K.; Marsh, H.: Catalytic graphitization of graphitizable carbon by chromium, manganese and molybdenum oxides. *Carbon* **1980**, *18*, 25-30.

(16) Sevilla, M.; Fuertes, A. B.: Catalytic graphitization of templated mesoporous carbons. *Carbon* **2006**, *44*, 468-474.

(17) Sevilla, M.; Fuertes, A. B.: Graphitic carbon nanostructures from cellulose. *Chemical Physics Letters* **2010**, *490*, 63-68.

(18) Sevilla, M.; Salinas Martinez-de Lecea, C.; Valdes-Solis, T.; Morallon, E.; Fuertes, A. B.: Solid-phase synthesis of graphitic carbon nanostructures from iron and cobalt gluconates and their utilization as electrocatalyst supports. *Physical Chemistry Chemical Physics* **2008**, *10*, 1433-1442.

(19) Lee, K. T.; Ji, X.; Rault, M.; Nazar, L. F.: Simple Synthesis of Graphitic Ordered Mesoporous Carbon Materials by a Solid-State Method Using Metal Phthalocyanines. *Angewandte Chemie International Edition* **2009**, *48*, 5661-5665.

(20) Frackowiak, E.: Carbon materials for supercapacitor application. *Physical Chemistry Chemical Physics* **2007**, *9*, 1774-1785.

(21) Gao, W.; Wan, Y.; Dou, Y.; Zhao, D.: Synthesis of Partially Graphitic Ordered Mesoporous Carbons with High Surface Areas. *Advanced Energy Materials* **2011**, *1*, 115-123.

(22) Kim, T.-W.; Park, I.-S.; Ryoo, R.: A Synthetic Route to Ordered Mesoporous Carbon Materials with Graphitic Pore Walls. *Angewandte Chemie* **2003**, *115*, 4511-4515.

(23) Kim, C. H.; Lee, D.-K.; Pinnavaia, T. J.: Graphitic Mesostructured Carbon Prepared from Aromatic Precursors. *Langmuir* **2004**, *20*, 5157-5159.

(24) Fuertes, A. B.; Alvarez, S.: Graphitic mesoporous carbons synthesised through mesostructured silica templates. *Carbon* **2004**, *42*, 3049-3055.

(25) Smått, J.-H.; Schunk, S.; Lindén, M.: Versatile Double-Templating Synthesis Route to Silica Monoliths Exhibiting a Multimodal Hierarchical Porosity. *Chemistry of Materials* **2003**, *15*, 2354-2361.

(26) Lu, A.-H.; Smått, J.-H.; Backlund, S.; Lindén, M.: Easy and flexible preparation of nanocasted carbon monoliths exhibiting a multimodal hierarchical porosity. *Microporous and Mesoporous Materials* **2004**, *72*, 59-65.

(27) Lu, A. H.; Smått, J. H.; Lindén, M.: Combined Surface and Volume Templating of Highly Porous Nanocast Carbon Monoliths. *Advanced Functional Materials* **2005**, *15*, 865-871.

(28) Brunauer, S.; Emmett, P. H.; Teller, E.: Adsorption of Gases in Multimolecular Layers. *Journal of the American Chemical Society* **1938**, *60*, 309-319.

(29) Barrett, E. P.; Joyner, L. G.; Halenda, P. P.: The Determination of Pore Volume and Area Distributions in Porous Substances. I. Computations from Nitrogen Isotherms. *Journal of the American Chemical Society* **1951**, *73*, 373-380.

(30) Vázquez-Santos, M. B.; Geissler, E.; László, K.; Rouzaud, J.-N.; Martínez-Alonso, A.; Tascón, J. M. D.: Comparative XRD, Raman, and TEM Study on Graphitization of PBO-Derived Carbon Fibers. *The Journal of Physical Chemistry C* **2012**, *116*, 257-268.

(31) Malard, L. M.; Pimenta, M. A.; Dresselhaus, G.; Dresselhaus, M. S.: Raman spectroscopy in graphene. *Physics Reports* **2009**, *473*, 51-87.

(32) Thambiliyagodage, C. J.; Hakat, Y.; Bakker, M. G.: One Pot Synthesis of Carbon/Ni Nanoparticle Monolithic Composites by Nanocasting and Their Catalytic Activity for 4-Nitrophenol Reduction. *Current Catalysis* **2016**, *5*, 135-146.

(33) Lau, S. S.; Mayer, J. W.; Tu, K. N.: Interactions in the Co/Si thin-film system. I. Kinetics. *Journal of Applied Physics* **1978**, *49*, 4005-4010.

(34) Cameán, I.; García, A. B.; Suelves, I.; Pinilla, J. L.; Lázaro, M. J.; Moliner, R.; Rouzaud, J.-N.: Influence of the inherent metal species on the graphitization of methane-based carbon nanofibers. *Carbon* **2012**, *50*, 5387-5394.

(35) Foggiato, J.; Yoo, W. S.; Ouaknine, M.; Murakami, T.; Fukada, T.: Optimizing the formation of nickel silicide. *Materials Science and Engineering: B* **2004**, *114–115*, 56-60.

(36) Hoekstra, J.; Beale, A. M.; Soulimani, F.; Versluijs-Helder, M.; Geus, J. W.; Jenneskens, L. W.: Base Metal Catalyzed Graphitization of Cellulose: A Combined Raman Spectroscopy, Temperature-Dependent X-ray Diffraction and High-Resolution Transmission Electron Microscopy Study. *The Journal of Physical Chemistry C* **2015**, *119*, 10653-10661.

(37) Ni, L.; Kuroda, K.; Zhou, L.-P.; Ohta, K.; Matsuishi, K.; Nakamura, J.: Decomposition of metal carbides as an elementary step of carbon nanotube synthesis. *Carbon* **2009**, *47*, 3054-3062.

(38) Tuinstra, F.; Koenig, J. L.: Raman Spectrum of Graphite. *The Journal of Chemical Physics* **1970**, *53*, 1126-1130.

(39) Nikiel, L.; Jagodzinski, P. W.: Raman spectroscopic characterization of graphites: A re-evaluation of spectra/ structure correlation. *Carbon* **1993**, *31*, 1313-1317.

(40) Dresselhaus, M. S.; Dresselhaus, G.; Saito, R.; Jorio, A.: Raman spectroscopy of carbon nanotubes. *Physics Reports* **2005**, *409*, 47-99.

(41) Hishiyama, Y.; Nakamura, M.: X-ray diffraction in oriented carbon films with turbostratic structure. *Carbon* **1995**, *33*, 1399-1403.

(42) Martins Ferreira, E. H.; Moutinho, M. V. O.; Stavale, F.; Lucchese, M. M.; Capaz, R. B.; Achete, C. A.; Jorio, A.: Evolution of the Raman spectra from single-, few-, and many-layer graphene with increasing disorder. *Physical Review B* **2010**, *82*, 125429.

(43) Casiraghi, C.; Hartschuh, A.; Qian, H.; Piscanec, S.; Georgi, C.; Fasoli, A.; Novoselov, K. S.; Basko, D. M.; Ferrari, A. C.: Raman Spectroscopy of Graphene Edges. *Nano Letters* **2009**, *9*, 1433-1441.

(44) Ferrari, A. C.; Robertson, J.: Resonant Raman spectroscopy of disordered, amorphous, and diamondlike carbon. *Physical Review B* **2001**, *64*, 075414.

(45) Ferrari, A. C.; Robertson, J.: Interpretation of Raman spectra of disordered and amorphous carbon. *Physical Review B* **2000**, *61*, 14095-14107.

(46) Cançado, L. G.; Jorio, A.; Ferreira, E. H. M.; Stavale, F.; Achete, C. A.; Capaz, R. B.; Moutinho, M. V. O.; Lombardo, A.; Kulmala, T. S.; Ferrari, A. C.: Quantifying Defects in Graphene via Raman Spectroscopy at Different Excitation Energies. *Nano Letters* **2011**, *11*, 3190-3196.

(47) Basko, D. M.; Piscanec, S.; Ferrari, A. C.: Electron-electron interactions and doping dependence of the two-phonon Raman intensity in graphene. *Physical Review B* **2009**, *80*, 165413.

(48) Lucchese, M. M.; Stavale, F.; Ferreira, E. H. M.; Vilani, C.; Moutinho, M. V. O.; Capaz, R. B.; Achete, C. A.; Jorio, A.: Quantifying ion-induced defects and Raman relaxation length in graphene. *Carbon* **2010**, *48*, 1592-1597.

(49) Cançado, L. G.; Pimenta, M. A.; Neves, B. R. A.; Dantas, M. S. S.; Jorio, A.: Influence of the Atomic Structure on the Raman Spectra of Graphite Edges. *Physical Review Letters* **2004**, *93*, 247401.

(50) Cuesta, A.; Dhamelincourt, P.; Laureyns, J.; Martínez-Alonso, A.; Tascón, J. M. D.: Raman microprobe studies on carbon materials. *Carbon* **1994**, *32*, 1523-1532.

(51) Shimada, T.; Sugai, T.; Fantini, C.; Souza, M.; Cançado, L. G.; Jorio, A.; Pimenta, M. A.; Saito, R.; Grüneis, A.; Dresselhaus, G.; Dresselhaus, M. S.; Ohno, Y.; Mizutani, T.; Shinohara, H.: Origin of the 2450 cm−1 Raman bands in HOPG, single-wall and double-wall carbon nanotubes. *Carbon* **2005**, *43*, 1049-1054.

(52) Vidano, R. P.; Fischbach, D. B.; Willis, L. J.; Loehr, T. M.: Observation of Raman band shifting with excitation wavelength for carbons and graphites. *Solid State Communications* **1981**, *39*, 341-344.

(53) Dresselhaus, M. S.; Jorio, A.; Hofmann, M.; Dresselhaus, G.; Saito, R.: Perspectives on Carbon Nanotubes and Graphene Raman Spectroscopy. *Nano Letters* **2010**, *10*, 751-758.

(54) Pimenta, M. A.; Dresselhaus, G.; Dresselhaus, M. S.; Cancado, L. G.; Jorio, A.; Saito, R.: Studying disorder in graphite-based systems by Raman spectroscopy. *Physical Chemistry Chemical Physics* **2007**, *9*, 1276-1290.

(55) Lee, Y.-J.: The second order Raman spectroscopy in carbon crystallinity. *Journal of Nuclear Materials* **2004**, *325*, 174-179.

(56) Lespade, P.; Marchand, A.; Couzi, M.; Cruege, F.: Caracterisation de materiaux carbones par microspectrometrie Raman. *Carbon* **1984**, *22*, 375-385.

(57) Witek, G.; Noeske, M.; Mestl, G.; Shaikhutdinov, S.; Behm, R. J.: Interaction of platinum colloids with single crystalline oxide and graphite substrates: a combined AFM, STM and XPS study. *Catalysis Letters*, *37*, 35-39.

(58) Briggs, D.; Beamson, G.: Primary and secondary oxygen-induced C1s binding energy shifts in x-ray photoelectron spectroscopy of polymers. *Analytical Chemistry* **1992**, *64*, 1729-1736.

(59) Biesinger, M. C.; Payne, B. P.; Grosvenor, A. P.; Lau, L. W. M.; Gerson, A. R.; Smart, R. S. C.: Resolving surface chemical states in XPS analysis of first row transition metals, oxides and hydroxides: Cr, Mn, Fe, Co and Ni. *Applied Surface Science* **2011**, *257*, 2717-2730.

(60) Payne, B. P.; Biesinger, M. C.; McIntyre, N. S.: The study of polycrystalline nickel metal oxidation by water vapour. *Journal of Electron Spectroscopy and Related Phenomena* **2009**, *175*, 55-65.

(61) Taguchi, A.; Smått, J. H.; Lindén, M.: Carbon Monoliths Possessing a Hierarchical, Fully Interconnected Porosity. *Advanced Materials* **2003**, *15*, 1209-1211.

(62) Grano, A. J.; Sayler, F. M.; Smått, J.-H.; Bakker, M. G.: Hierarchically porous monoliths of carbon and metal oxides with ordered mesopores. *Journal of Porous Materials* **2014**, *21*, 1113-1122.

(63) Marsh, H.; Warburton, A. P.: Catalysis of graphitisation. *Journal of Applied Chemistry* **1970**, *20*, 133-142.

CHAPTER 4

Heteroatom Rich Mesoporous Carbon as Supports for Gold Nanoparticles and Evaluation as Catalyst for Benzyl Alcohol Oxidation

4.1 Abstract

NC/O,N hierarchically porous carbon was synthesized by using furfuryl amine as the carbon precursors by nanocasting using hierarchically porous SiO_2 monoliths as the template. Performance was compared to nanocast material made using FA. After etching SiO_2, Au NPs supported on the carbon, were synthesized by incipient wetness followed by reduction of$HAuCl_4$. The resulting nanocomposites were characterized by TEM, SEM, XRD, XPS, Raman spectroscopy and N_2 sorption. It was found that both the mesoporous and macroporous structures were replicated in the carbon composites giving high surface area and mesopore volume. From analysis of TEM images average Au nanoparticle size of 39 nm was found for the NC/O support compared with 25 nm on NC/O,N. SEM images showed that the NPs were heterogeneously distributed on the macropores of carbon supports. Au NPs were found to be in zero oxidation state based on XRD and the surface of the NPs was not oxidized as indicated by XPS. Raman spectra indicated the presence of amorphous carbon and a new type of disorder could be seen in NC/O,N as revealed by the shift in D band frequency compared to NC/O. The Au NPs incorporated NC/O and NC/O,N were found to be efficient catalysts for benzyl alcohol oxidation.

4.2 Introduction

The oxidation of alcohols is an interesting organic transformation that has been extensively studied in the field of catalysis.[1-6] The selectivity of the desired product mainly depends on the properties of the catalyst. Production of the corresponding acid after complete oxidation[7,8] or the aldehyde by partial oxidation[9-12] or production of more than one product[6,13] has been found in many studies. NPs are attractive catalysts due to the high surface to volume ratio[14] but using NPs in homogeneous catalysis possess significant disadvantages. A homogeneous catalyst is hard to remove from the catalytic reaction limiting the potential use in industry.[15] Furthermore, product purification is more difficult: for cost effective removal, the NPs needs to be aggregated and precipitated.[16] This limits the reuse of NPs as catalyst, which is a significant limitation, especially the noble metal NPs which are expensive to synthesize.[17] NPs tend to aggregate to minimize the surface energy, and will do so easily when they are not covered by a ligand layer giving charge or steric repulsion. In order to prevent such aggregation they are protected from capping agents like polymers[18] and dendrimers[19] which result in the production of ultra small NPs. These NPs required to be aggregated after the reaction in order to analyze the products and hence cannot be reused. These drawbacks could be eliminated by stabilizing NPs on to a solid support as the solid catalysts could be easily removed from the reaction mixture.[15,17] But nanoparticle leaching is a common problem when they are stabilized on to a support.[15] Au NPs stabilized on solid supports have attracted interest as it could be used in many chemical reactions like hydrogenation,[20,21] oxidation[3,9] and coupling reactions.[22] Au NPs incorporated onto carbon supports like activated carbon, graphitic carbon and reduced graphene oxide have been investigated for the catalytic oxidation of benzyl alcohol.[23] It has been found that incorporation of two kinds of metal NPs like Au and Pd on activated carbon,[13,24] carbon

nanofibers,[25] and mesoporous carbon[26] increases the catalytic activity. Furthermore, bimetallic NPs like Au and Pd on mesoporous carbon have shown high selectivity to benzaldehyde.[26] In addition to carbon, other supports like SiO_2,[27] ceria,[28] and alumina[29] have also used as supports to immobilize Au NPs and bimetallic Au and Pd NPs. Carbon is often chosen as the support because carbon materials show high resistance to acids and bases, surface chemical structure can be modified, and porosity can be changed.[30] In this work mesoporous carbon rich with oxygen, and with oxygen and nitrogen have been synthesized by using FA and furfuryl amine as the carbon precursors respectively. $HAuCl_4$ was introduced onto the mesoporous carbon by an incipient wetness method followed by reduction to form Au NPs. The catalytic activity of the composite has been investigated for the oxidation of benzyl alcohol. The stability of the Au NPs on both oxygen, and oxygen and nitrogen rich carbon has been evaluated.

4.3 Experimental

4.3.1 Materials.

PEG 35,000, HNO_3 70%, KOH, benzyl alcohol, K_2CO_3, ethanol 95%, acetone and ethyl acetate were procured from VWR. NH_4OH 29% and H_2O_2 30% were purchased from Fisher Scientific. FA 98% and Furfuryl Amine were purchased from Acros Organics. TEOS 98% and anhydrous OA 98% were purchased from Alfa Aesar. C_{18}TAB was obtained from Genescript. $HAuCl_4 .3H_2O$ 49% was purchased from Sigma-Aldrich. All chemicals were used as received without further purification.

4.3.2 Catalyst synthesis

4.3.2.1 Synthesis of SiO_2 monoliths

Synthesis of SiO_2 monoliths was carried out according to a literature procedure.[31] Briefly, PEG 35000 (2.2 g) was added to 18 MΩ water and was stirred until it completely dissolved. Then 6.5 ml of 30% HNO_3 was added to the stirring mixture. Subsequently, 32 ml of TEOS was added and stirred until a homogeneous mixture was obtained. C_{18}TAB (5.5 g) was then added and the mixture was stirred until all surfactant was dissolved. The resulted sol was degassed for a few minutes. The sol was then poured into well plates, which were incubated at 40 °C for 72 h. The gels were removed from the well plates and were immersed in 1 M NH_4OH at 90 °C for 12 h. Then the monoliths were washed with 0.1 M HNO_3 and then washed with deionized water several times. After that the monoliths were washed with acetone and dried at 40 °C for 72 h. The monoliths were then calcined at 550 °C for 5 h at a heating rate of 1 °Cmin^{-1}.

4.3.2.2 Synthesis of NC/O

Preparation of NC/O was performed according to a modified version of a published procedure.[32,33] SiO_2 monoliths, the templates for NC, were degassed for several hours prior to use. FA was diluted with ethanol in a volume ratio of 5:1, and OA was dissolved in the mixture to give a molar ratio of FA:OA of 200:1. The SiO_2 monoliths were immersed in that mixture for 12 h. Then the monoliths were heated at 80 °C for 24 h to polymerize the FA. The infiltration and polymerization were repeated once. The monoliths were then heated to 800 °C in 4 h and were held at that temperature for 2 h in N_2 flow. After this pyrolysis the monoliths were etched in 3M KOH at 75 °C for 24 h in order to remove the SiO_2 template. They were then washed with deionized water several times and dried at room temperature.

4.3.2.3 Synthesis of NC/O,N

Synthesis of *NC/O,N* was carried out according to a modified version of an existing procedure.[34] The SiO_2 monoliths were degassed for several hours prior to use. They were infiltrated in furfuryl amine solution for 12 h. Then they were heated at 100 °C for 24 h and then at 160 °C for another 24 h in order to enhance the cross linking of furfuryl amine. The infiltration and heating were repeated for three times. Then pyrolysis, etching and drying were performed as described above for NC/O.

4.3.2.4 Synthesis of Au NPs supported NC

$HAuCl_4$ was introduced to mesoporous carbon by an incipient wetness method. Powdered NC was added to $HAuCl_4$ (1 mg/ml) aqueous solution in which the Au concentration was prepared to be 1 wt% relative to the carbon weight. The suspension was stirred for 24 h at room temperature and then heated at 80 °C while stirring until the solution evaporated. Then the powder was washed three times with deionized water until no Cl^- ions were detected in washings by UV-vis spectrophtometer. Then the powder was dried at 70 °C for 24 h. The dry powder was then heated to 250 °C in 4 h and held at that temperature for 2 h in 5% H_2/N_2 flow.

4.4 Characterization.

XRD patterns were collected by a Bruker D2 Phaser equipped with a Cu Kα emitting source (Wavelength, 1.54 Å) Lynx-Eye 1D strip detector, and an anti-scatter blade fixed at 3 mm. The interlayer spacing, d was calculated from the Bragg equation, $d= \lambda/2\sin\theta$, in which λ is the wavelength of the Cu Kα x-ray source, θ is the Bragg angle and d is the interlayer spacing. Crystallite size (L_C) was calculated by the Debye-Scherrer equation, $L_C = K\lambda/B\cos\theta$, in which

L_C is the crystallite size, K is the shape factor (0.9), and B is the FWHM in radians. The acquisition time for all samples was 1 h. TEM images were obtained on a FET Tecnai F20, equipped with a cold field emission gun and a super twin objective lens with an accelerating voltage of 200 kV. Samples were prepared on holey carbon supported by a Cu grid. The morphology was imaged using bright field image mode.

Raman spectra were acquired using a 10× objective lens with a laser, wavelength of 532nm, as the excitation source. The laser power at the sample was kept around 0.5 mW to avoid heating effects. The spectra were deconvoluted with Lorentizian curves by using the Peakfit software package. A base line subtraction was performed before fitting the data. The region with frequencies ranging from 1200 to 1800 cm^{-1} (so-called D- and G-bands) was fitted with three bands. XPS were acquired on a Kratos Axis 165 XPS system that is operated with a dual Mg/Al anode and a monochromatic x-ray source at 1486.6 eV, corresponding to the Al Kα line. Photoelectrons were collected with a takeoff angle of 90° relative to the sample surface. The survey and high resolution spectra were acquired in order to determine the chemical states of C, O, N and Au. The survey spectra were taken at a pass energy of 160 eV, with a step size of 0.1 eV, using a single scan. The dwell time was 500 ms for the survey spectra and 1000 ms for the high resolution spectra. The peak deconvolution of all the high resolution spectra was performed using Gaussian functions.

SEM images were collected using a JEOL 7000 FE-SEM operated at 30 kV, with diode based back scatter detector and an Oxford EDS detector for elemental analysis. N_2 adsorption measurements were taken on a Quantachrome Nova 2200e pore size analyzer at -197 °C with He mode to determine the surface area and void volumes of the monoliths. The interpretation of the isotherms was carried out with Quantachrome Nova Win software version 11.03, using a

multipoint BET method[35] to determine the surface areas and the BJH method[36] was applied to the adsorption branch to determine the pore size distribution. The volume of micropores was determined by the t-plot method. Product analysis was carried out on an HP 6890N GC connected to a Waters Micromass Quattro micro mass spectrometer equipped with a DB-1701 30 m × 320 µm × 1.0 µm, column.

4.5 Catalytic Tests.

The oxidation of benzyl alcohol was carried out by using a batch-type reaction vessel with a refluxing condenser. Typically, the powdered catalyst (20 mg) was added into an appropriate volume of deionized water in a 50 ml round bottom flask. Then 0.4 mmol of K_2CO_3 (0.053g) was added while stirring followed by 0.2 mmol of benzyl alcohol. The reaction mixture was heated to 95 °C while refluxing and then 1 mmol of H_2O_2 (30%) was quickly added and the reaction mixture was stirred for 24 h. The contents in the flask was cooled to room temperature and transferred into centrifuge tubes. The flask was washed with 1 ml of ethyl acetate and that was also transferred into a centrifuge tube. Then the reaction mixture was centrifuged at 10 000 rpm for 1 h. The supernatant was collected and was centrifuged again in the same conditions and then that supernatant was filtered through a 0.2 µm filter. The pH of the filtrate was adjusted to 2 and then the reactants and products were extracted with ethyl acetate using 1 ml of ethyl acetate three times. The extracts were collected and the trace of water was removed using $MgSO_4$ as drying agent. The internal standard method was used for the quantification where the internal standard, toluene was added to the extracted reactant and product mixture. Then reactants and products were analyzed by GC-MS.

Reusability study of the catalyst. The spent catalyst was centrifuge-washed at 10 000 rpm for 10 minutes with deionized water twice. It was then used for the catalytic reaction as described above.

4.6 Results and Discussion

4.6.1 Material Characterization

SiO_2 monoliths were cylindrical in shape and about 7 mm in length and 5 mm of diameter. The NC/O monoliths showed shrinkage compared to SiO_2 monoliths. The NC/O,N samples appeared to be initialing monoliths similar to the NC/O, but they broke during polymerization of the furfuryl amine and during etching of SiO_2. The effect of heating temperatures for the polymerization of furfuryl amine was explored; temperatures of 100 °C and 160 °C were tried, where the later temperature is above the boiling temperature of furfuryl amine (145 °C). So furfuryl amine tends to boil and evaporate rapidly at 160 °C before all the monomers linked as a continuous chain. The breaking of the monoliths during the etching could result from the furfuryl amine not being well cross-linked in the SiO_2 monolith templates so that the replication does not extend throughout the monolith. Removal of the SiO_2 template would then produce only fine powder or small pieces. The SEM image in Figure **4.1a** shows the macropore structure of the SiO_2 monoliths. SEM images in Figure **4.1b** and **c** show that the carbons produced by nanocasting (NC/O and NC/O,N respectively) show similar macropore structures to the SiO_2 monoliths. However, the macropore structure has broken during grinding as shown in Figure **4.1d** and **e** of NC/O/Au and NC/O,N/Au respectively. The N_2 sorption isotherm and TEM image which will discussed later, clearly show that in NC/O,N the mesopore structure is replicated. The confirmation of the presence of mesopore structure and the

macropore structure shows that furfuryl amine has polymerized in the SiO_2 monoliths, but as some of the NC/O,N monoliths were broken suggests that furfuryl amine has not completely cross-linked to give a continuous replica.

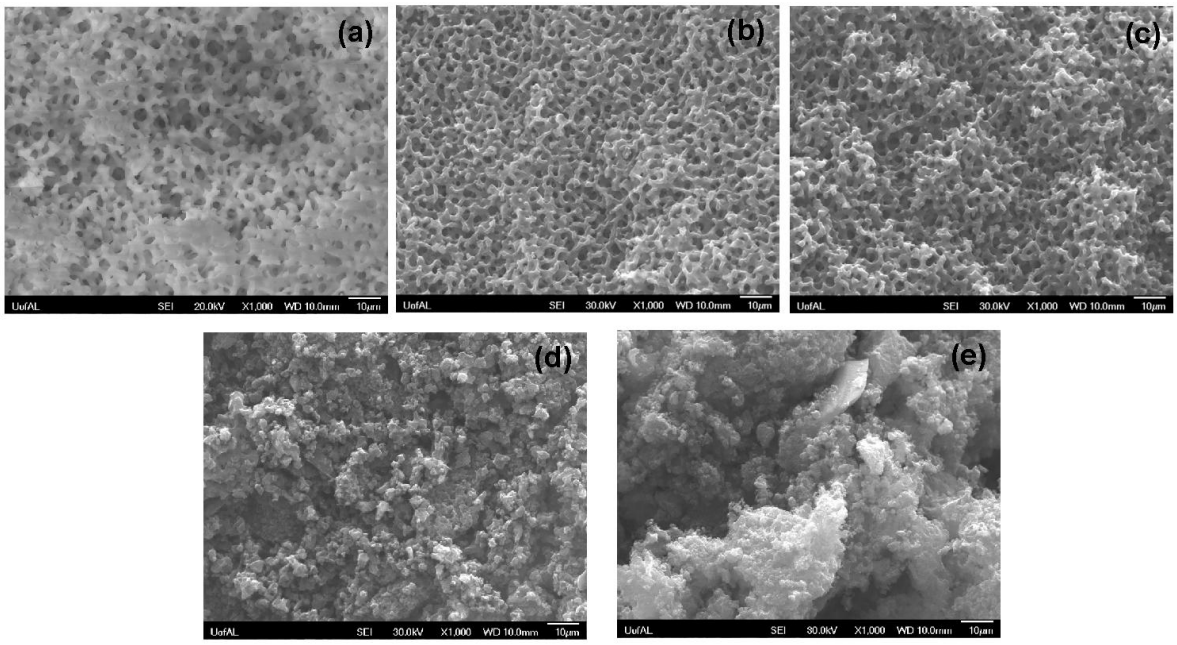

Figure (4.1). The SEM images of (a) SiO_2 (b) NC/O (c) NC/O,N (d) NC/O/Au (e) NC/O,N/Au.

The nitrogen isotherms and BJH pore size distribution plots of template and replicated materials are given in Figure **4.2a** and **4.2b,** respectively. The values of various textural parameters are given in Table **4.1**. The nitrogen sorption isotherm of SiO_2 shows two regions of N_2 uptake. The first N_2 uptake region around P/Po = 0.4 is due to the surfactant mesopores and the second uptake region round P/Po = 0.9 is due to the filling of textural mesopores.[32] In isotherms of both NC/O and NC/O,N the uptake around a relative pressure of 0.9 is almost absent indicating that textural mesopores are completely filled with carbon. But the uptake around a relative pressure of 0.4 indicates the presence of surfactant mesopores in both types of carbon. This clearly show that mesopore structure is replicated in NC/O and NC/O,N. The BJH pore size distribution shows a narrow peak at 3.4 nm in SiO_2, consistent with the C_{18}TAB used

as a porogen to make the SiO_2. The maxima in the pore size distributions for NC/O and NC/O,N are 3.2 nm and 4.4 nm, respectively, but the pore size distributions are much broader than that of the template SiO_2. This is consistent with earlier work.[37,38] Since the SiO_2 template has disordered surfactant mesopores, the mesopore walls show variable thickness. When the negative replica is former, the mesopores produced correspond to the silica walls, and so have a broader pore size distribution. The isotherms and pore size distributions of NC/O/Au and NC/O,N/Au show similar behavior to NC/O and NC/O,N, as would be expected. The BJH pore size distribution of NC/O/Au shows a narrow peak at 4.2 nm which corresponds to the NC/O peak at 3.2 nm. But NC/O,N/Au show a narrow peak at 4.4 nm being similar to NC/O,N. The replication by using furfuryl amine has taken place in similar fashion to the replication with FA at the mesopore level as indicated by the N_2 isotherms. The replication is the same at the macropore level as indicated by SEM images (Figure **4.2**).

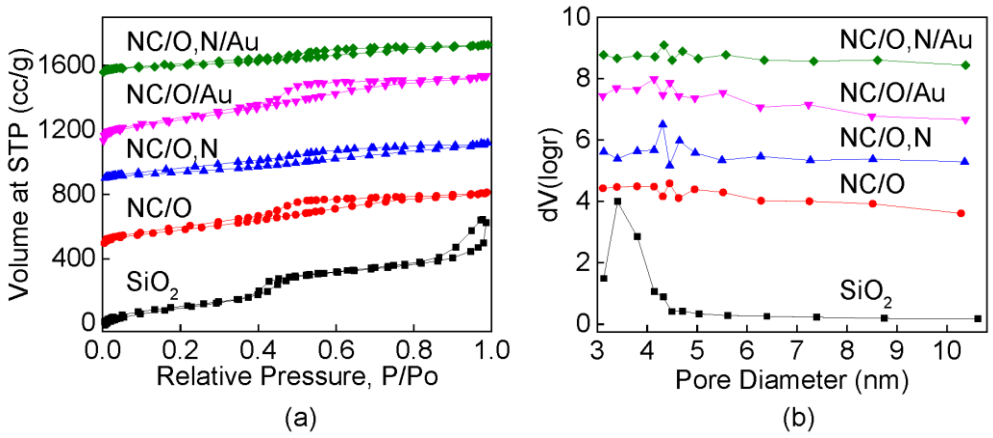

Figure (4.2). (a) N_2 sorption isotherms and (b) BJH pore size distributions of template and replicated materials.

Table **4.1**. Textural parameters of template and replicated materials.

Sample	BET Surface Area (m^2/g)	Total Pore Volume (cc/g)	Mesopore Volume (cc/g)	Micropore Volume (cc/g)	BJH Method Adsorption Pore Diameter (nm)
SiO_2	673	0.620	0.620	0.000	3.4
NC/O	650	0.480	0.477	0.003	3.2
NC/O,N	222	0.190	0.190	0.000	4.4
NC/O/Au	781	0.580	0.580	0.000	4.2
NC/O,N/Au	203	0.180	0.180	0.000	4.4

TEM images of NC/O/Au and NC/O,N/Au are given in Figure **4.3a** and **b,** respectively. Particle size distributions determined from these images are given in Figure **4.3c** and **d,** respectively. The Au NPs are distributed on the carbon matrix in a wide range as shown by TEM images and particle distribution histograms. The average particle sizes are 39 nm and 25 nm respectively, in NC/O/Au and NC/O,N/Au. In both composites nanoparticle aggregates were observed. Some of the NPs were partially aggregated. Larger NPs or aggregates could be produced during the reduction process because when NPs move through across the internal surfaces of the carbon they tend to encounter other Au NPs and grow by agglomeration.

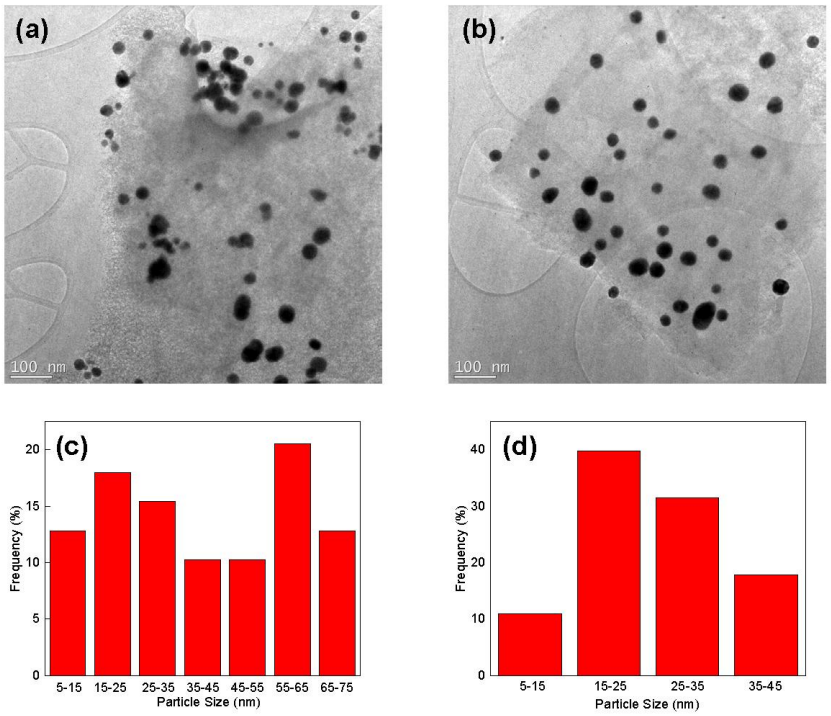

Figure (4.3). TEM images of (a) NC/O/Au (b) NC/O,N/Au Particle size distributions of (c) NC/O/Au (d) NC/O,N/Au.

The SEM images of NC/O/Au and NC/O,N/Au taken from the backscatter detector (COMPO) are given in Figure **4.4a** and **b,** respectively. Those images show that the NPs are distributed on the macropores and moreover they also show that in addition to the dispersed NPs, aggregated NPs are also present. These images also show that NPs are heterogeneously distributed on the surfaces of the macropores. The metal loading is 1 wt%, which is low relative to carbon. So the amount of NPs produced from such low metal loading will be less potentially giving a heterogeneous nanoparticle distribution on the carbon support. The method used to introduce the metal precursor is incipient wetness where precursor solution is stirred while heating with the carbon powder till all the solution evaporates. In this method, $HAuCl_4$ will precipitate when the solution locally reaches the solubility limit. At which point in the evaporation process this occurs depends upon the initial concentration of the solution, the total

pore volume, the total volume of solution added and the drying rate. It can also be impacted by the surface functionality, which can potentially act to nucleate crystal growth once the solubility limit is reached. If the solubility limit is much higher than the concentration of the added salt, then substantial evaporation will occur before the salt starts to precipitate giving a very inhomogeneous distribution of the salt, and so a heterogeneous distribution of (larger) gold nanoparticles. Moreover, if oxygen and/or nitrogen act as the binding sites for the gold precursor these sites may also not be homogeneously distributed on the carbon support. The percentage of oxygen and nitrogen present relative to carbon is relatively low as will be described in the XPS section, and so is more likely to be prone to being heterogeneous distributed within the carbon. When the binding sites are heterogeneously distributed, the precursor that adsorbs to those binding sites will produce heterogeneously distributed NPs after reduction.

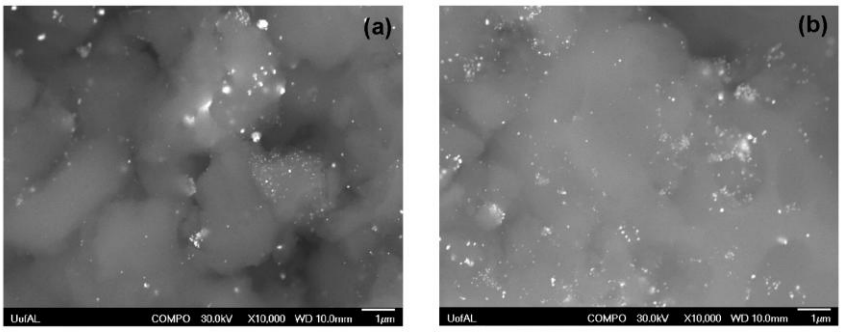

Figure (4.4). SEM images of (a) NC/O/Au (b) NC/O,N/Au taken from the back scatter detector.

The wide angle XRD patterns are given in Figure **5**. The XRD patterns of NC/O and NC/O,N show a broad peak around 2θ, 23.5° indicating the presence of amorphous carbon. In addition to that there is another small broad peak around 43.7° which is due to scattering from carbon (10) and (100) planes. The XRD patterns of NC/O/Au and NC/O,N/Au show peaks at 38.4°, 44.6°, 64.8°, 77.6° and 81.8° which could be assigned to diffractions of (111), (200),

(220), (311), and (222) of fcc metallic Au. Debye-Scherrer analysis was performed on (111) diffraction peak of NC/O/Au and NC/O,N/Au to determine the crystallite size of the Au crystals. The crystallite size calculated for NC/O/Au is 23.7 nm and for NC/O,N/Au it is 20.1 nm. These are in consistent with the average Au NP sizes determined by TEM. The d spacing was also calculated by using the (111) diffraction peak and they are 0.2345 nm and 0.2341 nm in NC/O/Au and NC/O,N/Au respectively.

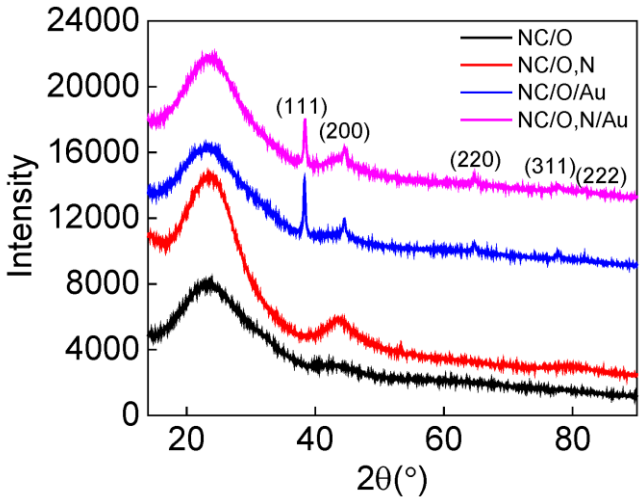

Figure (4.5). The wide angle XRD patterns.

Carbon materials were characterized by Raman spectroscopy to determine the vibrational modes of the material. The Raman spectra of NC/O, NC/O,N, NC/O/Au, and NC/O,N/Au are shown in Figure **4.6a, b, c,** and **d,** respectively. The G band, that appeared around 1600 cm^{-1}, corresponds to the zone center phonons of E_{2g} symmetry and the D band that appeared around 1350 cm^{-1} corresponds to the *K*- point phonons of A_{1g} symmetry.[39,40] The G band is due to the bond stretching of sp^2 atoms in both rings and chains and the D band is due to the breathing modes of sp^2 atoms in rings.[41] The third peak in between the D and G band is added to get a better fit. The D band appeared at about 1347 cm^{-1} in NC/O and in NC/O/Au but in NC/O,N and

NC/O,N/Au it appeared at about 1359 cm^{-1}. The shift of the D band in nitrogen functionalized carbon indicates a new type of disorder compared to the oxygen functionalized carbon.[42] The G band has not shifted. The intensity ratio of D and G bands is same in all samples indicating that there is no change in the crystallinity of the carbon due to the incorporation of nitrogen.

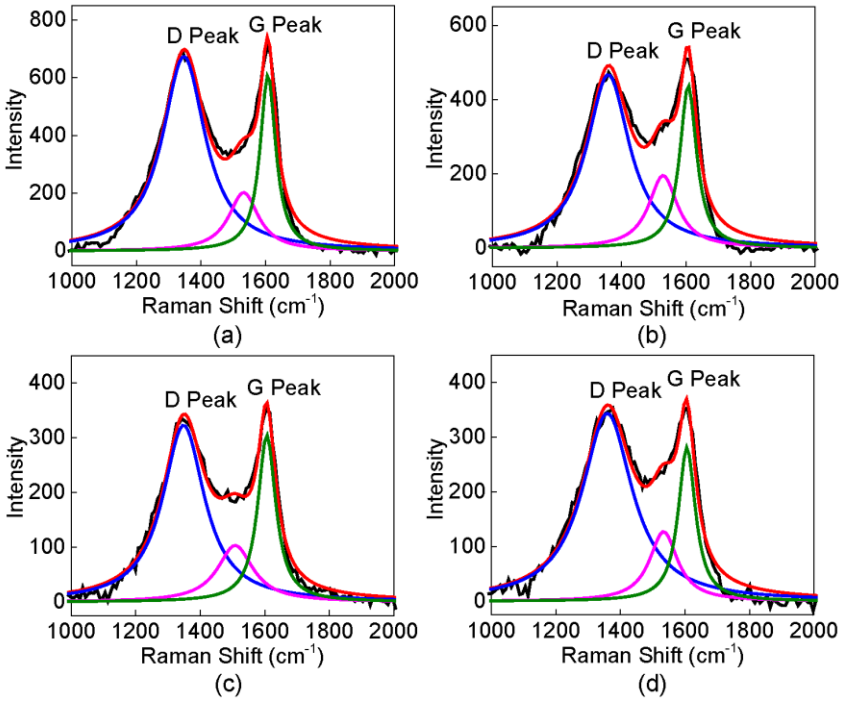

Figure (4.6). Raman spectra of (a) NC/O (b) NC/O,N (c) NC/O/Au (d) NC/O,N/Au.

High resolution XPS spectra (Figure **4.7**) were acquired in order to determine the chemical states of the elements of the catalysts. The high resolution spectrum of C 1s of NC/O/Au (Figure **4.7a**) shows sp^2 hybridized C-C at 284.4 eV, the same peak in NC/O,N/Au (Figure **4.7b**) appeared at 286.3 eV. The C-O feature appears at 285.7 eV in the high resolution spectrum of C 1s of NC/O/Au. But the various forms of C-N are also appearing in the region of 285-287 eV.[43] So in the high resolution spectrum of C 1s of NC/O,N/Au the peak at 285.6 eV is considered to arise from both C-O and C-N features. The peak at 287.5 eV in C 1s of NC/O/Au

and NC/O,N/Au corresponds to the C=O bond.[44] The highest binding energy peak of both NC/O/Au and NC/O,N/Au can be assigned to a shake-up peak. The high resolution spectra of O 1s of NC/O/Au and NC/O,N/Au are given in Figure **4.7c** and **d,** respectively. The peak appear around 531 eV corresponds to oxygen in C=O, the peak around 532 eV is assigned to oxygen singly bound to C[44] and the peak around 533.8 eV can be assigned to O bound to H.[43] The high resolution spectrum of N 1s in NC/O,N/Au is shown in Figure **4.7e**. The peak at 399.9 eV is assigned to pyrrolic N[45] where N is bound to two C atoms and the peak at 403.6 eV corresponds to oxidized N. It can be considered that furfuryl amine forms pyrrolic N where N is present in a five member ring bound to two C atoms during pyrolysis and it does not form any graphitic N which should appear at around 401 eV.[46] The oxidized N could be due to the KOH used for etching. The high resolution spectra of Au 4f of NC/O/Au and NC/O,N/Au are given in Figure **4.7f** and **g,** respectively. The Au $4f_{7/2}$ of NC/O/Au appeared at 84.4 eV and that of NC/O,N/Au at 83.9 eV indicating that the oxidation state of the surface of Au NPs is zero in both cases. The binding energy of Au $4f_{7/2}$ of NC/O/Au is slightly higher because the sample was slightly charging. The surface remains unoxidized due to the inertness of Au. The elemental composition as atomic percentage relative to carbon is given in Table **4.2**. It can be clearly seen that the atomic percentage of oxygen in NC/O/Au (3.53%) is higher than in NC/O,N/Au (3.35%). This is could be simply due to the presence of two oxygen atoms in furfuryl alcohol and one oxygen atom in furfuryl amine. However, the C:O ratio is 2:1 in furfuryl alcohol, so it is clear that during the pyrolysis/carbonization more oxygen is lost than is carbon. It is also unclear if and how the KOH etch to remove the SiO_2 impacts the presence of oxygen. It is entirely possible that the hydroxide could react with the carbon atoms at the surface of the carbon. Further, it is possible that the high surface area carbon could also pick up atmospheric oxygen and water after etching.

The atomic nitrogen percentage relative to carbon, 5% indicates good nitrogen incorporation has been achieved by using furfuryl amine as the nitrogen precursor. Although this level of incorporation does indicate that nitrogen is preferentially lost rather than carbon during the pyrolysis/carbonization, as the initial percentage would be closer to 20%. The atomic percentages of Au are 0.09 and 0.14 in NC/O/Au and NC/O,N/Au respectively. They can be considered as approximately the same within the error range as the step size used for analysis is 0.1 eV.

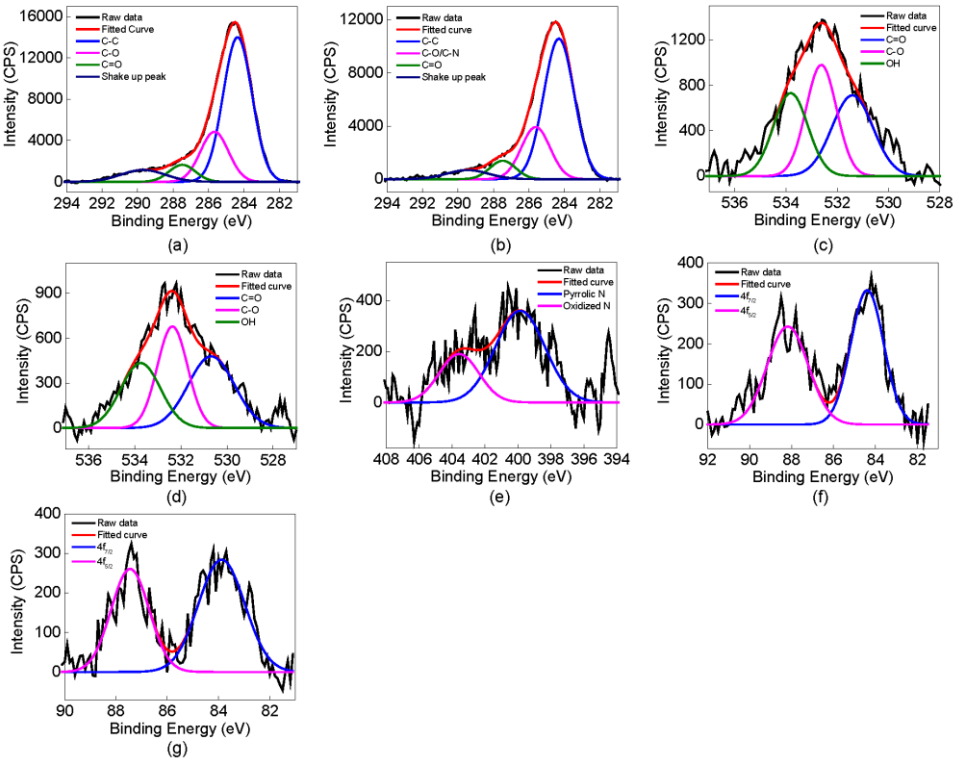

Figure (4.7). High resolution XPS spectra of, C 1s of (a) NC/O/Au (b) NC/O,N/Au, O 1s of (c) NC/O/Au (d) NC/O,N/Au, N 1s of (e) NC/O,N/Au, Au 4f of (f) NC/O/Au (g) NC/O,N/Au.

Table **4.2**. Atomic percentages relative to C based on XPS quantification.

Catalyst	Atomic Percentage Relative to C		
	O	N	Au
NC/O/Au	3.53	-	0.094
NC/O,N/Au	3.34	5.07	0.14

4.6.2 Catalytic activity

NC/O/Au has converted 81.5% of benzyl alcohol while 91.5% has been converted by NC/O,N/Au when used as catalysts. NC/O/Au has higher selectivity to benzoic acid (96.7%) and lower selectivity to benzaldehyde (3.3%). NC/O,N/Au also show higher selectivity to benzoic acid (61.4%) than the selectivity for benzaldehyde (38.6%). The TON and TOF of NC/O/Au are 0.815 mol/g and 0.034 mol/g.h, and 0.915 mol/g and 0.038 mol/g.h in NC/O,N/Au. If the NPs are considered as spheres the total surface area of NC/O/Au is higher than of NC/O,N/Au as the average particle sizes are 39 nm and 25 nm, respectively. If the Au loading is assumed to be approximately the same, the number of NPs produced at larger particle size on NC/O/Au should be lower than that of NC/O,N/Au. This suggests that the total surface area of NC/O/Au should be lower than that of NC/O,N/Au and that could be the reason for the higher conversion resulted in NC/O,N/Au than NC/O/Au.

The NC/O consists of different oxygen containing functional groups such as C-O, C=O and OH as indicated by the XPS data. These groups might render adjacent carbon atoms positively charged because of the electron withdrawing oxygen atoms in the graphene π system.[47] These oxygen containing groups could be the active sites. NC/O,N contains nitrogen in addition to oxygen. So in addition to the above discussed functional groups, nitrogen containing

functional groups present could also be active sites. Nitrogen rich carbons show high catalytic activity because their edges and defective sites can interact with N atoms to form C-N bonds, which make adjacent carbon atoms positively charged. These carbon atoms can interact with benzyl alcohol an ion and promote the electron transfer between catalyst and reactants.[47] Alternatively, the presence of nitrogen on the surface could give rise to hydrogen bonding with the benzyl alcohol, although not with the benzaldehyde. The dual active sites present in NC/O,N/Au may have resulted in high catalytic activity than in NC/O/Au.

The reusability study of NC/O/Au and NC/O,N/Au (Figure **4.8a** and **b**) showed that the conversion on subsequent cycles is lower than the first run. When the NC/O/Au is used the conversion drops to 48 % by the second run and that gradually decreases to 14% by the fifth cycle. The selectivity to benzoic acid gradually decreases from 96.7 % for the first cycle to 59.4% for the fifth run while the selectivity to benzaldehyde increases from 3.3% to 40.6% in the fifth run. This decrease in activity, and the increasing benzaldehyde yield are consistent with a two-step reaction mechanism in which there is a decrease in overall activity of the catalyst with reuse. Possible explanations for the decrease in activity are (1) aggregation of the nanoparticles leading to a decrease in the total metal surface area; (2) Nanoparticle leaching in which the total number of NPs and total metal surface area decreases.

If the formation of benzoic acid and benzaldehyde occurs in a two-step mechanism for which the second step is the slower step, then decreasing surface area could significantly impact the product yield; Decreasing metal surface area would change the surface area to substrate ratio: as benzyl alcohol molecules get partially oxidized partially to benzaldehyde at the catalyst surface less surface area is available for the (faster) benzyl alcohol oxidation. So the conversion of benzyl alcohol decreases when the catalyst is used on subsequent cycles.

The conversion of benzyl alcohol does not show a trend in the reusability work of NC/O,N/Au. The selectivity to benzoic acid increases from 61.4 % to 90.1% till the fourth cycle but decreases to 73.5 % at the fifth run. The selectivity to benzaldehyde decreases gradually from 38.6% at the first run to 9.9% at the fourth run but increases to 26.4% at the fifth cycle.

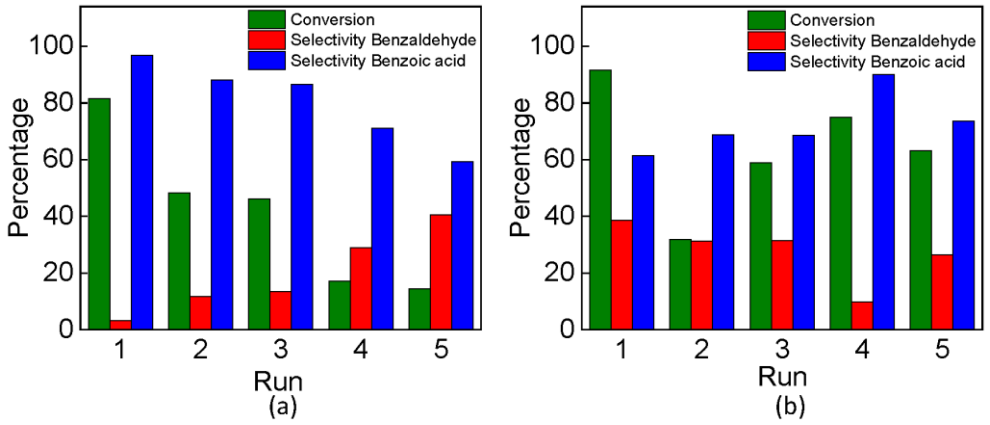

Figure (4.8). Reusability study of (a) NC/O/Au (b) NC/O,N/Au.

The SEM images taken from the COMPO of NC/O/Au and NC/O,N/Au after five cycles of catalysis are shown in Figure **4.9a** and **b,** respectively. From the SEM images it is hard to decide whether there is a decrease in the number of NPs in both catalysts as the SEM images are taken from two different places before and after catalysis. But in general in both catalysts after five cycles there is are a considerable number of NPs remaining. Similarly it is not clear if there was a significant change in the extent of aggregation/agglomeration observed, as again, the location matters on deciding the nanoparticle size distribution. However in both catalysts the conversion of benzyl alcohol was lower on the subsequent cycles than the first cycle. So it could be that the nanoparticle leaching and aggregation have occurred. It cannot be concluded which catalyst the change was most pronounced as there was considerable variability in the conversion

and the selectivity when NC/O,N/Au was used as the catalyst. Therefore it cannot be concluded that that one heteroatom, oxygen or nitrogen stabilizes the Au NPs more than the other.

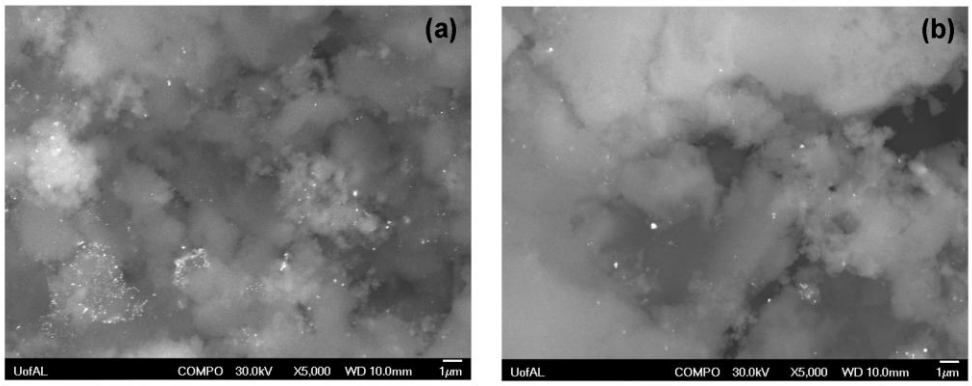

Figure (4.9). SEM images of the used catalysts after five cycles of (a) NC/O/Au (b) NC/O,N/Au taken from the back scatter detector.

4.7 Conclusions

Oxygen and nitrogen rich hierarchically porous carbons were synthesized by nanocasting. $HAuCl_4$ was introduced by an incipient wetness method followed by reduction in 5% H_2/N_2 to produce Au NPs. These catalysts were efficient for benzyl alcohol oxidation by H_2O_2. The nitrogen rich catalyst was more active than the oxygen only catalysts. The conversion of benzyl alcohol in subsequent cycles is lower than the first cycle for both catalysts suggesting that nanoparticle leaching and/or aggregation occurred regardless of the heteroatom content.

4.8 References

(1) He, Y.; Yang, P.; Fan, J.; Liu, Y.; Du, Y.; Feng, J.; Fan, F.; Li, D.: Facile and surfactant-free synthesis of supported Pd nanoparticles on hydrotalcite for oxidation of benzyl alcohol. *RSC Advances* **2015**, *5*, 74907-74915.

(2) Hou, W.; Dehm, N. A.; Scott, R. W. J.: Alcohol oxidations in aqueous solutions using Au, Pd, and bimetallic AuPd nanoparticle catalysts. *Journal of Catalysis* **2008**, *253*, 22-27.

(3) Kumar, A.; Kumar, V. P.; Srikanth, A.; Vishwanathan, V.; Chary, K. V. R.: Vapor Phase Oxidation of Benzyl Alcohol over Nano Au/SBA-15 Catalysts: Effect of Preparation Methods. *Catalysis Letters* **2016**, *146*, 35-46.

(4) Ma, C. Y.; Dou, B. J.; Li, J. J.; Cheng, J.; Hu, Q.; Hao, Z. P.; Qiao, S. Z.: Catalytic oxidation of benzyl alcohol on Au or Au-Pd nanoparticles confined in mesoporous silica. *Applied Catalysis B: Environmental* **2009**, *92*, 202-208.

(5) Mallat, T.; Baiker, A.: Oxidation of alcohols with molecular oxygen on platinum metal catalysts in aqueous solutions. *Catalysis Today* **1994**, *19*, 247-283.

(6) Villa, A.; Janjic, N.; Spontoni, P.; Wang, D.; Su, D. S.; Prati, L.: Au–Pd/AC as catalysts for alcohol oxidation: Effect of reaction parameters on catalytic activity and selectivity. *Applied Catalysis A: General* **2009**, *364*, 221-228.

(7) Anderson, R.; Griffin, K.; Johnston, P.; Alsters, P. L.: Selective Oxidation of Alcohols to Carbonyl Compounds and Carboxylic Acids with Platinum Group Metal Catalysts. *Advanced Synthesis & Catalysis* **2003**, *345*, 517-523.

(8) Ji, H.; Mizugaki, T.; Ebitani, K.; Kaneda, K.: Highly efficient oxidation of alcohols to carbonyl compounds in the presence of molecular oxygen using a novel heterogeneous ruthenium catalyst. *Tetrahedron Letters* **2002**, *43*, 7179-7183.

(9) Long, N. Q.; Quan, N. A.: Highly selective oxidation of benzyl alcohol to benzaldehyde catalyzed by nano Au/γ-Al_2O_3 under environment-friendly conditions. *Reaction Kinetics, Mechanisms and Catalysis* **2015**, *114*, 147-155.

(10) Zhan, B.-Z.; White, M. A.; Sham, T.-K.; Pincock, J. A.; Doucet, R. J.; Rao, K. V. R.; Robertson, K. N.; Cameron, T. S.: Zeolite-Confined Nano-RuO_2: A Green, Selective, and Efficient Catalyst for Aerobic Alcohol Oxidation. *Journal of the American Chemical Society* **2003**, *125*, 2195-2199.

(11) Ji, H.-B.; Ebitani, K.; Mizugaki, T.; Kaneda, K.: Environmentally friendly alcohol oxidation using heterogeneous catalyst in the presence of air at room temperature. *Catalysis Communications* **2002**, *3*, 511-517.

(12) Mahyari, M.; Shaabani, A.; Behbahani, M.; Bagheri, A.: Thiol-functionalized fructose-derived nanoporous carbon as a support for gold nanoparticles and its application for aerobic oxidation of alcohols in water. *Applied Organometallic Chemistry* **2014**, *28*, 576-583.

(13) Pritchard, J.; Kesavan, L.; Piccinini, M.; He, Q.; Tiruvalam, R.; Dimitratos, N.; Lopez-Sanchez, J. A.; Carley, A. F.; Edwards, J. K.; Kiely, C. J.; Hutchings, G. J.: Direct Synthesis of Hydrogen Peroxide and Benzyl Alcohol Oxidation Using Au−Pd Catalysts Prepared by Sol Immobilization. *Langmuir* **2010**, *26*, 16568-16577.

(14) Chaturvedi, S.; Dave, P. N.; Shah, N. K.: Applications of nano-catalyst in new era. *Journal of Saudi Chemical Society* **2012**, *16*, 307-325.

(15) Gruber-Woelfler, H.; Radaschitz, P. F.; Feenstra, P. W.; Haas, W.; Khinast, J. G.: Synthesis, catalytic activity, and leaching studies of a heterogeneous Pd-catalyst including an immobilized bis(oxazoline) ligand. *Journal of Catalysis* **2012**, *286*, 30-40.

(16) Yuan, Y.; Yan, N.; Dyson, P. J.: pH-Sensitive Gold Nanoparticle Catalysts for the Aerobic Oxidation of Alcohols. *Inorganic Chemistry* **2011**, *50*, 11069-11074.

(17) Cole-Hamilton, D. J.: Homogeneous Catalysis-New Approaches to Catalyst Separation, Recovery, and Recycling. *Science* **2003**, *299*, 1702-1706.

(18) Tsunoyama, H.; Sakurai, H.; Ichikuni, N.; Negishi, Y.; Tsukuda, T.: Colloidal Gold Nanoparticles as Catalyst for Carbon-Carbon Bond Formation: Application to Aerobic Homocoupling of Phenylboronic Acid in Water. *Langmuir* **2004**, *20*, 11293-11296.

(19) Garcia-Martinez, J. C.; Lezutekong, R.; Crooks, R. M.: Dendrimer-Encapsulated Pd Nanoparticles as Aqueous, Room-Temperature Catalysts for the Stille Reaction. *Journal of the American Chemical Society* **2005**, *127*, 5097-5103.

(20) Gu, H.; Xu, X.; Chen, A.-a.; Ao, P.; Yan, X.: Separate deposition of gold and palladium nanoparticles on ordered mesoporous carbon and evaluation of their catalytic activity for cinnamaldehyde hydrogenation under atmospheric condition. *Catalysis Communications* **2013**, *41*, 65-69.

(21) Gu, H.; Xu, X.; Li, Y.; Chen, A.-a.; Ao, P.; Yan, X.: Homogeneously dispersed gold nanoparticles stabilized on the walls of ordered mesoporous carbon via a simple and repeatable method with enhanced hydrogenation properties for nitro-group. *Microporous and Mesoporous Materials* **2013**, *173*, 189-196.

(22) Datta, K. K. R.; Reddy, B. V. S.; Ariga, K.; Vinu, A.: Gold Nanoparticles Embedded in a Mesoporous Carbon Nitride Stabilizer for Highly Efficient Three-Component Coupling Reaction. *Angewandte Chemie International Edition* **2010**, *49*, 5961-5965.

(23) Yu, X.; Huo, Y.; Yang, J.; Chang, S.; Ma, Y.; Huang, W.: Reduced graphene oxide supported Au nanoparticles as an efficient catalyst for aerobic oxidation of benzyl alcohol. *Applied Surface Science* **2013**, *280*, 450-455.

(24) Wang, D.; Villa, A.; Spontoni, P.; Su, D.; Prati, L.: In Situ Formation of Au–Pd Bimetallic Active Sites Promoting the Physically Mixed Monometallic Catalysts in the Liquid-Phase Oxidation of Alcohols. *Chemistry - A European Journal* **2010**, *16*, 10007-10013.

(25) Villa, A.; Wang, D.; Spontoni, P.; Arrigo, R.; Su, D.; Prati, L.: Nitrogen functionalized carbon nanostructures supported Pd and Au-Pd NPs as catalyst for alcohols oxidation. *Catalysis Today* **2010**, *157*, 89-93.

(26) Hao, Y.; Hao, G.-P.; Guo, D.-C.; Guo, C.-Z.; Li, W.-C.; Li, M.-R.; Lu, A.-H.: Bimetallic Au–Pd Nanoparticles Confined in Tubular Mesoporous Carbon as Highly Selective and Reusable Benzyl Alcohol Oxidation Catalysts. *ChemCatChem* **2012**, *4*, 1595-1602.

(27) Wang, L.; Meng, X.; Wang, B.; Chi, W.; Xiao, F.-S.: Pyrrolidone-modified SBA-15 supported Au nanoparticles with superior catalytic properties in aerobic oxidation of alcohols. *Chemical Communications* **2010**, *46*, 5003-5005.

(28) Zhang, H.; Xie, Y.; Sun, Z.; Tao, R.; Huang, C.; Zhao, Y.; Liu, Z.: In-Situ Loading Ultrafine AuPd Particles on Ceria: Highly Active Catalyst for Solvent-Free Selective Oxidation of Benzyl Alcohol. *Langmuir* **2011**, *27*, 1152-1157.

(29) Pawelec, B.; Venezia, A. M.; La Parola, V.; Cano-Serrano, E.; Campos-Martin, J. M.; Fierro, J. L. G.: AuPd alloy formation in Au-Pd/Al_2O_3 catalysts and its role on aromatics hydrogenation. *Applied Surface Science* **2005**, *242*, 380-391.

(30) Rodríguez-Reinoso, F.: The role of carbon materials in heterogeneous catalysis. *Carbon* **1998**, *36*, 159-175.

(31) Smått, J.-H.; Schunk, S.; Lindén, M.: Versatile Double-Templating Synthesis Route to Silica Monoliths Exhibiting a Multimodal Hierarchical Porosity. *Chemistry of Materials* **2003**, *15*, 2354-2361.

(32) Lu, A.-H.; Smått, J.-H.; Backlund, S.; Lindén, M.: Easy and flexible preparation of nanocasted carbon monoliths exhibiting a multimodal hierarchical porosity. *Microporous and Mesoporous Materials* **2004**, *72*, 59-65.

(33) Lu, A. H.; Smått, J. H.; Lindén, M.: Combined Surface and Volume Templating of Highly Porous Nanocast Carbon Monoliths. *Advanced Functional Materials* **2005**, *15*, 865-871.

(34) Dombrovskis, J. K.; Jeong, H. Y.; Fossum, K.; Terasaki, O.; Palmqvist, A. E. C.: Transition Metal Ion-Chelating Ordered Mesoporous Carbons as Noble Metal-Free Fuel Cell Catalysts. *Chemistry of Materials* **2013**, *25*, 856-861.

(35) Brunauer, S.; Emmett, P. H.; Teller, E.: Adsorption of Gases in Multimolecular Layers. *Journal of the American Chemical Society* **1938**, *60*, 309-319.

(36) Barrett, E. P.; Joyner, L. G.; Halenda, P. P.: The Determination of Pore Volume and Area Distributions in Porous Substances. I. Computations from Nitrogen Isotherms. *Journal of the American Chemical Society* **1951**, *73*, 373-380.

(37) Taguchi, A.; Smått, J. H.; Lindén, M.: Carbon Monoliths Possessing a Hierarchical, Fully Interconnected Porosity. *Advanced Materials* **2003**, *15*, 1209-1211.

(38) Grano, A. J.; Sayler, F. M.; Smått, J.-H.; Bakker, M. G.: Hierarchically porous monoliths of carbon and metal oxides with ordered mesopores. *Journal of Porous Materials* **2014**, *21*, 1113-1122.

(39) Ferrari, A. C.; Robertson, J.: Interpretation of Raman spectra of disordered and amorphous carbon. *Physical Review B* **2000**, *61*, 14095-14107.

(40) Cançado, L. G.; Jorio, A.; Ferreira, E. H. M.; Stavale, F.; Achete, C. A.; Capaz, R. B.; Moutinho, M. V. O.; Lombardo, A.; Kulmala, T. S.; Ferrari, A. C.: Quantifying Defects in Graphene via Raman Spectroscopy at Different Excitation Energies. *Nano Letters* **2011**, *11*, 3190-3196.

(41) Ferrari, A. C.; Robertson, J.: Resonant Raman spectroscopy of disordered, amorphous, and diamondlike carbon. *Physical Review B* **2001**, *64*, 075414.

(42) Bulusheva, L. G.; Okotrub, A. V.; Kinloch, I. A.; Asanov, I. P.; Kurenya, A. G.; Kudashov, A. G.; Chen, X.; Song, H.: Effect of nitrogen doping on Raman spectra of multi-walled carbon nanotubes. *Physica Status Solidi B* **2008**, *245*, 1971-1974.

(43) Hellgren, N.; Haasch, R. T.; Schmidt, S.; Hultman, L.; Petrov, I.: Interpretation of X-ray photoelectron spectra of carbon-nitride thin films: New insights from in situ XPS. *Carbon* **2016**, *108*, 242-252.

(44) Wu, M.; Feng, Q.; Sun, X.; Wang, H.; Gielen, G.; Wu, W.: Rice (Oryza sativa L) plantation affects the stability of biochar in paddy soil. *Scientific Reports* **2015**, *5*, 10001.

(45) Bertóti, I.; Mohai, M.; László, K.: Surface modification of graphene and graphite by nitrogen plasma: Determination of chemical state alterations and assignments by quantitative X-ray photoelectron spectroscopy. *Carbon* **2015**, *84*, 185-196.

(46) Ibrahim, E. M. M.; Khavrus, V. O.; Leonhardt, A.; Hampel, S.; Oswald, S.; Rümmeli, M. H.; Büchner, B.: Synthesis, characterization, and electrical properties of nitrogen-doped single-walled carbon nanotubes with different nitrogen content. *Diamond and Related Materials* **2010**, *19*, 1199-1206.

(47) Chen, S.; Duan, J.; Jaroniec, M.; Qiao, S.-Z.: Nitrogen and Oxygen Dual-Doped Carbon Hydrogel Film as a Substrate-Free Electrode for Highly Efficient Oxygen Evolution Reaction. *Advanced Materials* **2014**, *26*, 2925-2930.

CHAPTER 5

Conclusions and Future Work

Porous carbon composites incorporating metal NPs with high surface area was synthesized by nanocasting using hierarchically porous SiO_2 monoliths as the template. The synthesis of hierarchically porous carbon monoliths with metal NPs, in which metal NPs are produced during the carbonization of carbon precursors, is introduced in chapter 1. The incorporation of metal NPs reduced the surface area and mesopore volume for the composite compared with the carbon monoliths without NPs but such metal NP/porous carbon composites still possessing high values of those textural parameters. The carbon composites with nickel NPs were found to have high catalytic activity for the reduction of *p*-nitrophenol by $NaBH_4$. One intermediate product observed was *p*-quinoimine which was sufficiently stable that is was observed by GC/MS. In these composites Ni NPs were observed to also catalyze the graphitization of amorphous carbon. This observation led to the work discussed in chapter 2 where the catalytic graphitization of amorphous carbon monoliths by NPs of iron, cobalt and nickel was studied.

Amorphous carbon was observed to convert primarily to turbostratic carbon in the presence of iron, cobalt and nickel NPs. The catalytic activity of iron was greater than cobalt and nickel, cobalt being higher in activity than nickel. The extent of catalytic graphitization was increased at higher pyrolysis temperature. Though the metal NPs resulted in crystallizing some of amorphous carbon, as found in TEM images, XRD patterns and Raman data show that large amounts of amorphous carbon were still present in all the samples. Further, turbostractic carbon

is still less ordered than truly graphitic carbon, and so it is not clear if the increase in crystallinity would be sufficient to improve the stability of electrical conductivity of the composites over those of the basic carbon monolith. The structure of the carbon, particularly as observed in the TEM is consistent with the dissolution-precipitation mechanism.

Hierarchically porous carbon monoliths incorporating oxygen and nitrogen were synthesized by nanocasting. The monoliths formed by nanocasting generally contain significant amounts of oxygen, which could come from either the FA precursor used, or by incorporation during the hydroxide etch used to remove the silica template. Monoliths with a high nitrogen content were prepared using furfuryl amine as the precursor. It was found that multiple infiltration cycles were needed to produce complete monoliths. It was suggested that this multiple infiltration was necessary because the furfuryl amine did not completely polymerize in the SiO_2 monoliths and so was evaporated rather than carbonized during the pyrolysis step. $HAuCl_4$ was used as the gold precursor and it was introduced to mesoporous carbon by the incipient wetness method, followed by reduction in 5% H_2/N_2 to form Au NPs. These catalysts were found to be relatively catalytically active for oxidation of benzyl alcohol to benzyl aldehyde and to benzoic acid. The catalytic activity decreased after the first cycle in those catalysts regardless of the heteroatom which they are rich with. It cannot be concluded the exact reason for the loss of activity, either nanoparticle leaching or agglomeration because a quantitative determination was not performed. However as NPs could be seen in SEM images after catalysis with few aggregates it can be both reasons have caused the loss of activity. So nanoparticle leaching and aggregation have occurred in the catalysts and hence NPs were not completely stabilized by incorporating these heteroatoms.

Preparation and applications of porous carbon supporting metal NPs by nanocasting have been discussed above. The methods developed for the synthesis are believed to have value to the scientific community but still need to be further optimized.

Among approaches that could improve the properties of the materials: synthesis of a range of different percentages of nickel supported on NC monoliths and the evaluation of the impact of this on the catalytic activity for *p*-nitrophenol reduction. This would allow the nickel loading that gave the maximum catalytic activity can be determined. It would be interesting to carry out a kinetic study of the catalytic activity using the monolithic form of the prepared catalysts rather than the powdered form. This could be done in one of two ways (1) if the monoliths can be made mechanically more robust then they could be used in a batch process. This would allow the whole monolith to be removed after the reaction making both analysis of the extent of reaction easier (since the solution does not have to be filtered to remove particles) and it will make recycling studies easier, as the total mass of catalyst should not change. (2) The prepared catalysts in monolithic form can be used to make a flow reactor. The monolithic form is expected to have lower pressure drop for fluids passing through the monolith than for the equivalent packed bed of particles. The extent of conversion depends upon the activity and the residence time, i.e. the time a given plug of the fluid spends inside the monolith. For a more catalytically active monolith a given residence time will give higher conversion. The length of the monolith also impacts the residence time, a longer monolith will increase the residence time, increasing the extent of conversion. Similarly lower flow rate increases residence time. Such flow systems also address loss of catalytic activity by leaching of NPs compared with agglomeration. The use of sodium borohydride overcomes one concern with hydrogenation in a flow reactor, which is that mixing of hydrogen gas with a liquid reactant (*p*-nitrophenol) is

problematic since at ambient pressure the mixing is very limited. However, decomposition of borohydride can lead to gas bubble formation, which can be a major issue in a monolithic reactor, impacting the fluid flow through the reactor.

The impact of the amount of catalyst on the catalytic graphitization can be determined by using different Co and Ni loadings. It will be more difficult to vary the amount of Fe as the rate of FA polymerization is significantly accelerated by the $Fe(NO_3)_2$. $9H_2O$ required for 1 wt% Fe. Incorporation of higher percentages would likely not be effective for infiltration of FA in to the template because the solution would solidify rapidly due to the faster polymerization.

The amount of metal incorporated into the monolith also impacts the nanoparticle size which increases with increasing metal incorporation: this will allow the effect of nanoparticle size on graphitization to be studied. The electrical conductivity of the prepared metal incorporated carbon monoliths can be measured. This is known to be strongly impacted by the amount of graphitic carbon in a monolith. The graphitic character of carbon is also known to impact the chemical stability. This could be assessed by either thermogravimetric analysis (TGA) in the presence of air/oxygen, since graphitic carbon reacts more slowly with oxygen than does amorphous carbon, or by reaction with peroxide which similarly reacts much more quickly with amorphous carbon than graphitic carbon.

The effect of heteroatoms on stabilizing metal NPs could be quantitatively measured by performing a leaching study of NPs and measuring the concentration of metal in the solution by inductively coupled plasma mass spectrometry, or by AAS, if the solution concentration is raised by evaporation of the solvent.

Increased loading of the metal NPs on the support is likely to impact the catalytic activity in a number of ways: A larger number of nanoparticles are expected to significantly increase the

rate of a given catalyzed reaction. However, addition of more metal is also likely to lead to larger nanoparticles. Both number and larger size could well impact the rates of the two oxidation reactions different resulting in a reaction which could be more or less selective for benzaldehyde or benzoic acid. The variation of the conversion and the selectivity during the reaction could also be studied by conducting the reaction for different time periods.

REFERENCES

(1) Parlett, C. M. A.; Wilson, K.; Lee, A. F.: Hierarchical porous materials: catalytic applications. *Chemical Society Reviews* **2013**, *42*, 3876-3893.

(2) Smått, J.-H.; Schunk, S.; Lindén, M.: Versatile Double-Templating Synthesis Route to Silica Monoliths Exhibiting a Multimodal Hierarchical Porosity. *Chemistry of Materials* **2003**, *15*, 2354-2361.

(3) Lu, A. H.; Smått, J. H.; Lindén, M.: Combined Surface and Volume Templating of Highly Porous Nanocast Carbon Monoliths. *Advanced Functional Materials* **2005**, *15*, 865-871.

(4) Smått, J.-H.; Sayler, F. M.; Grano, A. J.; Bakker, M. G.: Formation of Hierarchically Porous Metal Oxide and Metal Monoliths by Nanocasting into Silica Monoliths. *Advanced Engineering Materials* **2012**, *14*, 1059-1073.

(5) Freire, R. M.; de Morais Batista, A. H.; de Souza Filho, A. G.; Filho, J. M.; Saraiva, G. D.; Oliveira, A. C.: High Catalytic Activity of Nitrogen-Containing Carbon from Molecular Sieves in Fine Chemistry. *Catalysis Letters* **2009**, *131*, 135-145.

(6) Ryoo, R.; Joo, S. H.; Jun, S.: Synthesis of Highly Ordered Carbon Molecular Sieves via Template-Mediated Structural Transformation. *The Journal of Physical Chemistry B* **1999**, *103*, 7743-7746.

(7) Ryoo, R.; Joo, S. H.; Jun, S.; Tsubakiyama, T.; Terasaki, O.: 07-O-01 - Ordered mesoporous carbon molecular, sieves by templated synthesis: the structural varieties. In *Studies in Surface Science and Catalysis*; A. Galarneau, F. F. F. D. R., Vedrine, J., Eds.; Elsevier, 2001; Vol. Volume 135; pp 150.

(8) Xia, Y.; Yang, Z.; Mokaya, R.: Simultaneous Control of Morphology and Porosity in Nanoporous Carbon: Graphitic Mesoporous Carbon Nanorods and Nanotubules with Tunable Pore Size. *Chemistry of Materials* **2006**, *18*, 140-148.

(9) Kleitz, F.; Hei Choi, S.; Ryoo, R.: Cubic Ia3d large mesoporous silica: synthesis and replication to platinum nanowires, carbon nanorods and carbon nanotubes. *Chemical Communications* **2003**, 2136-2137.

(10) Taguchi, A.; Smått, J. H.; Lindén, M.: Carbon Monoliths Possessing a Hierarchical, Fully Interconnected Porosity. *Advanced Materials* **2003**, *15*, 1209-1211.

(11) Lu, A.-H.; Smått, J.-H.; Backlund, S.; Lindén, M.: Easy and flexible preparation of nanocasted carbon monoliths exhibiting a multimodal hierarchical porosity. *Microporous and Mesoporous Materials* **2004**, *72*, 59-65.

(12) Goel, C.; Bhunia, H.; Bajpai, P. K.: Resorcinol-formaldehyde based nanostructured carbons for CO2 adsorption: kinetics, isotherm and thermodynamic studies. *RSC Advances* **2015**, *5*, 93563-93578.

(13) Lin, Y.-P.; Lin, H.-P.; Chen, D.-W.; Liu, H.-Y.; Teng, H.; Tang, C.-Y.: Using phenol-formaldehyde resin as carbon source to synthesize mesoporous carbons of different pore structures. *Materials Chemistry and Physics* **2005**, *90*, 339-343.

(14) Hao, G.-P.; Li, W.-C.; Wang, S.; Wang, G.-H.; Qi, L.; Lu, A.-H.: Lysine-assisted rapid synthesis of crack-free hierarchical carbon monoliths with a hexagonal array of mesopores. *Carbon* **2011**, *49*, 3762-3772.

(15) Hao, G.-P.; Li, W.-C.; Qian, D.; Wang, G.-H.; Zhang, W.-P.; Zhang, T.; Wang, A.-Q.; Schüth, F.; Bongard, H.-J.; Lu, A.-H.: Structurally Designed Synthesis of Mechanically Stable Poly(benzoxazine-co-resol)-Based Porous Carbon Monoliths and Their Application as High-Performance CO2 Capture Sorbents. *Journal of the American Chemical Society* **2011**, *133*, 11378-11388.

(16) Sevilla, M.; Fuertes, A. B.: Fabrication of porous carbon monoliths with a graphitic framework. *Carbon* **2013**, *56*, 155-166.

(17) Li, Z.; Liu, J.; Huang, Z.; Yang, Y.; Xia, C.; Li, F.: One-Pot Synthesis of Pd Nanoparticle Catalysts Supported on N-Doped Carbon and Application in the Domino Carbonylation. *ACS Catalysis* **2013**, *3*, 839-845.

(18) Cheon, J. Y.; Kim, T.; Choi, Y.; Jeong, H. Y.; Kim, M. G.; Sa, Y. J.; Kim, J.; Lee, Z.; Yang, T.-H.; Kwon, K.; Terasaki, O.; Park, G.-G.; Adzic, R. R.; Joo, S. H.: Ordered mesoporous porphyrinic carbons with very high electrocatalytic activity for the oxygen reduction reaction. *Scientific Reports* **2013**, *3*, 2715.

(19) Kong, A.; Kong, Y.; Zhu, X.; Han, Z.; Shan, Y.: Ordered mesoporous Fe (or Co)-N-graphitic carbons as excellent non-precious-metal electrocatalysts for oxygen reduction. *Carbon* **2014**, *78*, 49-59.

(20) Yang, Y.; Ren, Y.; Sun, C.; Hao, S.: Facile route fabrication of nickel based mesoporous carbons with high catalytic performance towards 4-nitrophenol reduction. *Green Chemistry* **2014**, *16*, 2273-2280.

(21) Bhowmik, T.; Kundu, M. K.; Barman, S.: Ultra small gold nanoparticles-graphitic carbon nitride composite: an efficient catalyst for ultrafast reduction of 4-nitrophenol and removal of organic dyes from water. *RSC Advances* **2015**, *5*, 38760-38773.

(22) Kotbagi, T. V.; Hakat, Y.; Bakker, M. G.: Facile one-pot synthesis and characterization of nickel supported on hierarchically porous carbon. *Materials Research Bulletin* **2016**, *73*, 204-210.

(23) Liu, Y.; Li, D.; Lin, B.; Sun, Y.; Zhang, X.; Yang, H.: Hydrothermal synthesis of Ni-doped hierarchically porous carbon monoliths for hydrogen storage. *Journal of Porous Materials* **2015**, *22*, 1417-1422.

(24) Kotbagi, T. V.; Hakat, Y.; Bakker, M. G.: Novel one-pot synthesis of hierarchically porous Pd/C monoliths by a co-gelation method. *MRS Communications* **2015**, *5*, 51-56.

(25) Ōya, A.; Marsh, H.: Phenomena of catalytic graphitization. *Journal of Materials Science* **1982**, *17*, 309-322.

(26) Ōya, A.; Ōtani, S.: Catalytic graphitization of carbons by various metals. *Carbon* **1979**, *17*, 131-137.

(27) Sevilla, M.; Salinas Martinez-de Lecea, C.; Valdes-Solis, T.; Morallon, E.; Fuertes, A. B.: Solid-phase synthesis of graphitic carbon nanostructures from iron and cobalt gluconates and their utilization as electrocatalyst supports. *Physical Chemistry Chemical Physics* **2008**, *10*, 1433-1442.

(28) Hoekstra, J.; Beale, A. M.; Soulimani, F.; Versluijs-Helder, M.; Geus, J. W.; Jenneskens, L. W.: Base Metal Catalyzed Graphitization of Cellulose: A Combined Raman Spectroscopy, Temperature-Dependent X-ray Diffraction and High-Resolution Transmission Electron Microscopy Study. *The Journal of Physical Chemistry C* **2015**, *119*, 10653-10661.

(29) Mochida, I.; Ohtsubo, R.; Takeshita, K.; Marsh, H.: Catalytic graphitization of graphitizable carbon by chromium, manganese and molybdenum oxides. *Carbon* **1980**, *18*, 25-30.

(30) Mochida, I.; Ohtsubo, R.; Takeshita, K.; Marsh, H.: Catalytic graphitization of non-graphitizable carbon by chromium and manganese oxides. *Carbon* **1980**, *18*, 117-123.

(31) Li, Z. Q.; Lu, C. J.; Xia, Z. P.; Zhou, Y.; Luo, Z.: X-ray diffraction patterns of graphite and turbostratic carbon. *Carbon* **2007**, *45*, 1686-1695.

(32) Ferrari, A. C.; Robertson, J.: Interpretation of Raman spectra of disordered and amorphous carbon. *Physical Review B* **2000**, *61*, 14095-14107.

(33) Cançado, L. G.; Jorio, A.; Ferreira, E. H. M.; Stavale, F.; Achete, C. A.; Capaz, R. B.; Moutinho, M. V. O.; Lombardo, A.; Kulmala, T. S.; Ferrari, A. C.: Quantifying Defects in Graphene via Raman Spectroscopy at Different Excitation Energies. *Nano Letters* **2011**, *11*, 3190-3196.

(34) Ferrari, A. C.; Robertson, J.: Resonant Raman spectroscopy of disordered, amorphous, and diamondlike carbon. *Physical Review B* **2001**, *64*, 075414.

(35) Martins Ferreira, E. H.; Moutinho, M. V. O.; Stavale, F.; Lucchese, M. M.; Capaz, R. B.; Achete, C. A.; Jorio, A.: Evolution of the Raman spectra from single-, few-, and many-layer graphene with increasing disorder. *Physical Review B* **2010**, *82*, 125429.

(36) Basko, D. M.; Piscanec, S.; Ferrari, A. C.: Electron-electron interactions and doping dependence of the two-phonon Raman intensity in graphene. *Physical Review B* **2009**, *80*, 165413.

(37) Vidano, R. P.; Fischbach, D. B.; Willis, L. J.; Loehr, T. M.: Observation of Raman band shifting with excitation wavelength for carbons and graphites. *Solid State Communications* **1981**, *39*, 341-344.

(38) Malard, L. M.; Pimenta, M. A.; Dresselhaus, G.; Dresselhaus, M. S.: Raman spectroscopy in graphene. *Physics Reports* **2009**, *473*, 51-87.

(39) Vázquez-Santos, M. B.; Geissler, E.; László, K.; Rouzaud, J.-N.; Martínez-Alonso, A.; Tascón, J. M. D.: Comparative XRD, Raman, and TEM Study on Graphitization of PBO-Derived Carbon Fibers. *The Journal of Physical Chemistry C* **2012**, *116*, 257-268.

(40) Chen, S.; Duan, J.; Jaroniec, M.; Qiao, S.-Z.: Nitrogen and Oxygen Dual-Doped Carbon Hydrogel Film as a Substrate-Free Electrode for Highly Efficient Oxygen Evolution Reaction. *Advanced Materials* **2014**, *26*, 2925-2930.